

DESIGN, FABRICATION AND TESTING OF A NOVEL DUAL-AXIS AUTOMATIC SOLAR
TRACKER SYSTEM USING A FRESNEL-LENS SOLAR CONCENTRATOR

Laura Mabel Almara

Thesis Prepared for the Degree of

MASTER OF SCIENCE

UNIVERSITY OF NORTH TEXAS

August 2021

APPROVED:

Weihuam Zhao, Major Professor
Qandil Hassan, Committee Member
Prasad Vishwanath, Committee Member
Kuruvilla John, Chair of Department of
Mechanical Engineering
Hanchen Huang, Dean of the College of
Engineering
Victor Prybutok, Dean of the Toulouse
Graduate School

Almara, Laura Mabel. *Design, Fabrication and Testing of a Novel Dual-Axis Automatic Solar Tracker System Using a Fresnel-Lens Solar Concentrator*. Master of Science (Mechanical and Energy Engineering), August 2021, 113 pp., 14 tables, 69 figures, 5 appendices, 39 numbered references.

This thesis project investigates, analyzes, designs, simulates, constructs and tests a dual-axis solar tracker system to track the sun and concentrates the heat of the sunlight, using a Fresnel lens, into a small area, which is above of an evaporator, to increase the temperature of the seawater to convert it into freshwater. The dual-axis solar tracker was designed with the main objectives that the structure was portable, dismountable, lightweight, low cost, corrosion resistant, wires inside pipes, accurate, small size, follow the sun automatically, off-grid (electrical), use green energy (solar powered), and has an empty area right below of the lens.

First, a 500 mm diameter flat Fresnel lens was selected and simulated based on an algorithmic method achieved by a previous PhD student at UNT using MATLAB®, to give the optimization lens dimensions. The lens profile was drawn with AutoCAD®, then output profile lens was simulated in COMSOL Multiphysics®. The objective was to provide the high efficiency, optimum and high precision of the focal rays and heat to the receiver of the evaporator. A novel dual-axis solar tracker system was then designed that is portable, dismountable, lightweight and corrosion resistant. The solar tracker tracks the sun in two axis of rotation automatically during the day time, maximizing the angles of inclination on each axis. After testing computer simulations, the dual-axis solar tracker system was constructed and tested. Last, a detailed cost analysis was performed of the entire project. The outcome of this work can be applied for desalination seawater purposes or other any Fresnel lens application that require a focal high temperature directed by dual-axis solar tracker system.

Copyright 2021

By

Laura Mabel Almara

ACKNOWLEDGMENTS

During this journey it was possible to transform ideas and designs into a tangible outcome. The hard effort required was rewarded with the obtained results, looking a concrete solution for a real problem.

The present master thesis project would have not been possible without the endless and incredible support and love of my family. Dad, a clever person, thanks for the deep engineering guideline and motivation along my life. Your teachings forged the professional that I'm today. Mom, my endless emotional support and motivator, thanks for everything. Brother, for your insightful comments and support during the construction of this project.

A deep and candid appreciation goes to my advisor, Dr. Weihuan Zhao, for her incessant supervision, advice, support and guidance during the entire process of my project. I thank Dr. Vishwanath Prasad and Dr. Hassan Qandil, who have accepted to form part of the committee research group. My special appreciation goes to Dr. Vishwanath Prasad, who forged to emerge the deep analysis and analytical thinking in me. A great appreciation also goes to Dr. Hassan Qandil for his endless advice, guidance and encouragement.

I would like to express my appreciation to the University of North Texas for providing the opportunity to be part of it and growth in my academic life.

TABLE OF CONTENTS

	Page
ACKNOWLEDGMENTS.....	iii
LIST OF TABLES.....	vii
LIST OF FIGURES.....	viii
CHAPTER 1. INTRODUCTION AND OVERVIEW.....	1
1.1 Introduction.....	1
1.2 Overview	2
1.3 Importance and Scope.....	3
CHAPTER 2. FRESNEL-LENS SOLAR CONCENTRATOR.....	6
2.1 Design Parameters	6
2.2 Simulations.....	7
2.2.1 Heat Transfer and Ray Heating	9
2.2.2 Ray Heating: Fresnel Lens for Other Applications.....	20
2.2.3 Wind Speed Velocity and Pressure	21
2.2.4 Analysis of Fresnel Lens Only.....	21
CHAPTER 3. DUAL-AXIS SOLAR TRACKING SYSTEM	24
3.1 Introduction.....	24
3.2 Literature Review	24
3.3 Overall View of the Project.....	32
3.3.1 CAD Model.....	32
3.3.2 Fabrication Model.....	34
3.4 Design.....	36
3.4.1 Static Equilibrium Momentum Analysis.....	36
3.4.2 Worm Gear	38
3.4.3 LDR Sensors Analysis.....	40
3.4.4 Novel Sensor Holder	44
3.4.5 Stopper Motion Pad.....	45

3.5	Simulations.....	46
3.5.1	Worm-Gear Assembly.....	46
3.5.2	Wind Speed Velocity and Pressure Simulation of the Dual-Axis Solar Tracker System	49
3.5.3	Visualization and Results for 40° to 140° Inclination Angle Representation	55
CHAPTER 4. FABRICATION.....		60
4.1	Fabrication.....	60
4.2	Hardware.....	60
4.2.1	LDR (Photoresistor).....	60
4.2.2	Sensor Holder Assembly	61
4.2.3	Stepper Motor	62
4.2.4	Security Limit Switches	63
4.2.5	Manual Controls	64
4.2.6	Controller Box.....	65
4.2.7	3D Printed Parts.....	65
4.3	Software	71
4.3.1	Controller Logic.....	71
4.3.2	Electronic and Electric Circuit	73
4.3.3	Flowchart of the Algorithm Logic of the Automatic Dual Solar Tracking System	74
4.3.4	Day/Night Mode	78
4.3.5	Automatic Relocation of the Fresnel lens for the Next Day	79
CHAPTER 5. PROTOTYPE TESTING		80
5.1	Worm-Gear Assembly	80
5.2	Novel Sensor Holder	80
5.3	Manual Positioning Switches and Stopper Motion Pads	82
5.4	Solar Tracker System	83
CHAPTER 6. PROJECT COST AND ANALYSIS		85
6.1	Project Cost	85
6.2	Comparison with Other Projects	91

6.3	Conclusions.....	92
CHAPTER 7. CONCLUSIONS AND FUTURE WORK		93
7.1	Conclusions.....	93
7.2	Future Work	94
APPENDIX A. SOLAR TRACKER TESTING PROCEDURES		95
APPENDIX B. SOLAR TRACKER TROUBLESHOOTING PROCEDURES.....		97
APPENDIX C. MICROCONTROLLER CODE.....		99
APPENDIX D. POSSIBLE IMPROVEMENTS		105
APPENDIX E. CHRONOLOGICAL CONSTRUCTION PHOTO GALLERY		107
REFERENCES.....		110

LIST OF TABLES

	Page
Table 2.1: Design parameters of the Fresnel lens.	7
Table 2.2: Thermal and mechanical properties of materials.	8
Table 2.3: Heat transfer parameters.	11
Table 2.4: Geometrical optics parameters.	11
Table 2.5: Total energy at the receiver, efficiencies and transmittance lens for three different receiver diameters.	16
Table 2.6: Maximum temperatures results combining three different receiver diameters, receiver thickness, and rod thickness, applying heat transfer.	17
Table 2.7: Maximum temperature and receiver surface heat flux results combining three different receiver diameters, receiver thickness, and rod thickness applying ray heating.....	17
Table 2.8: Maximum values of pressure for different wind speed values.	21
Table 3.1: Summary of solar tracker literature review.....	25
Table 3.2: Design parameters of the worm gear.....	38
Table 3.3: Maximum temperature and heat flux on the receiver surface due to ray heating, from 40° to 140° inclination angle respect ground of the dual-axis solar tracker.....	57
Table 4.1: Name Part Description and Quantity of 3D Printed Parts.....	66
Table 6.1: Detailed bill of materials and costs of the dual-axis solar tracker system.	86
Table 6.2: Summarize of project cost by categories.....	90

LIST OF FIGURES

	Page
Figure 1.1: Different types of solar radiation beams.....	4
Figure 1.2: Earth’s photovoltaic power potential [3].....	5
Figure 2.1: Parameters of flat Fresnel lens design.....	6
Figure 2.2: Transparent figure of the components.....	8
Figure 2.3: Heat transfer simulation results for 4 hours: (a) 3D chamber temperature distribution using heat transfer by applying Gaussian function, (b) schematization of the Gaussian function on the receiver surface, (c) temperature distribution along the receiver surface (top view), and (d) 1D maximum, minimum and average temperate of the plate receiver as functions of time.....	10
Figure 2.4: 3D Temperature distribution and ray trajectory using ray heating.	12
Figure 2.5: Ray heating temperature results for 4 hours: (a) 2D receiver surface temperature distribution (top view), (b) curve of temperature distribution along the receiver surface, (c) 1D receiver depth temperate, and (d) 1D maximum, minimum and average temperate of the plate receiver as functions of time.....	12
Figure 2.6: Ray heating heat flux results for 4 hours: (a) 2D receiver surface heat flux distribution (top view), and (b) 1D receiver surface inward heat flux distribution along the receiver diameter as function of the variation time.....	13
Figure 2.7: Three examples of receiver diameter and thickness, and rod thickness: (a) 1.5 in receiver diameter with 0.5 in receiver thickness and 0.06252 in rod thickness, (b) 1.75 in receiver diameter with 1 in receiver thickness and 0.25 in rod thickness, and (c) 3 in receiver diameter with 1.5 in receiver thickness and 0.366 in rod thickness.....	14
Figure 2.8: Diameter receiver: 1.5 in, 500 mm diameter Fresnel lens with 500 mm focal length: (a) MATLAB® plot of the Gauss function of second order, and (b) 3D receiver surface inward heat flux distribution using Gaussian function of (a).....	15
Figure 2.9: Diameter receiver: 1.75 in, 500 mm diameter Fresnel lens with 500 mm focal length: (a) MATLAB® plot of the Gauss function of second order, and (b) 3D receiver surface inward heat flux distribution using Gaussian function of (a).....	15
Figure 2.10: Diameter receiver: 3 in, 500 mm diameter Fresnel lens with 500 mm focal length: (a) MATLAB® plot of the Gauss function of second order, and (b) 3D receiver surface inward heat flux distribution using Gaussian function of (a).....	16

Figure 2.11: Maximum temperature results combining three different receiver diameters, receiver thickness, and rod thickness, applying heat transfer. 18

Figure 2.12: (a) Maximum temperature results combining three different receiver diameters, receiver thickness, and rod thickness, and (b) receiver surface heat flux for three different receiver diameters, receiver thickness, and rod thickness. both applying ray heating. 19

Figure 2.13: Ray heating applied to a 1.5 inches receiver diameter and thickness. 20

Figure 2.14: Second order polynomial fitting maximum pressure versus wind speed. 22

Figure 2.15: Wind simulation on the Fresnel lens surface applying a wind speed of 44 mph: (a)-(d) Different views of the lens showing the pressure distribution and maximum and minimum pressure locations, (e) and (f) Sliced view of wind speed velocity and pressure distribution around the lens, and (g) and (h) Wind streamline flow showing the maximum and minimum pressure values. 23

Figure 3.1: Number of publications based on tracking application. 25

Figure 3.2: (a) Overall CAD model view of the dual-axis solar tracker system showing the interior of the controller box, (b) a different perspective of (a), (c) and (d) most unfavorable position regarding to inclination angle, being closer in a corner of the solar tracker. 33

Figure 3.3: 3D Overall view of the dual-axis solar tracker system showing the rays trajectories focusing and concentrating on the receiver surface. 33

Figure 3.4: Solar tracker system project..... 34

Figure 3.5: (a) – (c) Different perspectives of the solar tracker project..... 35

Figure 3.6: Diagram of dimensions and forces for the DAST. 37

Figure 3.7: Schematic diagram of the worm-gear pair force. 39

Figure 3.8: Variation of efficiency of LDR with solar radiation. 40

Figure 3.9: Resistance [kOhms] vs. Light [Lux]. 41

Figure 3.10: Measurement of LDR resistance as a function of illumination: (a) Full direct sunlight without tapping the LDR, (b) Indirect sunlight without tapping the LDR. 42

Figure 3.11: Sensor without taping used in the test..... 43

Figure 3.12: (a) LDR sensor taped. (b) Full direct sun experimental set up of the circuit with taped sensors..... 44

Figure 3.13: Shadow concept..... 45

Figure 3.14: Sensor holder components.	45
Figure 3.15: Stopper motion pad.	46
Figure 3.16: Worm gear simulation: (a) geometry of the model, and (b) mesh of the geometry model.	47
Figure 3.17: Worm gear simulation: (a) frictionless contact type between the worm and gear, and (b) worm gear teeth contact body view.	47
Figure 3.18: Worm gear simulation: (a) frictionless contact type between the bolt and the gear shaft hole, (b) bolt contact body view, and (c) gear shaft hole contact body view.	48
Figure 3.19: Worm gear simulation: (a) frictionless contact type between the shaft support and the worm shaft, (b) worm shaft contact body view, and (c) shaft support contact body view. ...	48
Figure 3.20: Worm gear simulation: (a) types of loads and supports applied on the model, (b) total deformation result, (c) equivalent elastic strain result, and (d) equivalent stress result. ...	49
Figure 3.21: Wind velocity distribution on the solar tracker system surface at 20 mph wind speed.	50
Figure 3.22: Wind simulation applying 44 mph wind speed on the solar tracker system surface: (a) and (b) distribution, location, and maximum/minimum values of wind velocity, and (c) and (d) distribution, location, and maximum/minimum values of pressure.	52
Figure 3.23: Wind simulation applying 65 mph wind speed on the solar tracker system surface: (a) and (b) distribution, location, and maximum/minimum values of wind velocity, and (c) and (d) distribution, location, and maximum/minimum values of pressure.	54
Figure 3.24: Representation of different inclination angles that takes the solar tracker system during the day, following the sun light.	56
Figure 3.25: Values of maximum temperature and heat flux on the receiver surface due to ray heating, from 40° to 140° inclination angle respect ground of the dual-axis solar tracker.	57
Figure 3.26: Visual inclination angle variation, from 40° to 140°, of the dual-axis solar tracker with values of maximum temperature and heat flux on the receiver surface due to ray heating.	59
Figure 4.1: LDR sensor.	61
Figure 4.2: Sensor holder assembly and components.	61
Figure 4.3: (a) Stepper motor, (b) Different point of view of (a).	62
Figure 4.4: Technical characteristics of the selected stepper motor.	62

Figure 4.5: Security limits switches: (a)-(b) they located in two different frames, one for each axis rotation.	63
Figure 4.6: Controller box: outside.....	64
Figure 4.7: (a)-(f) Before and after of using heat shrink tubes in the connection wires.	65
Figure 4.8: 3D printed gears: (a) gear type 1-front side, (b) gear type 1-rear side, (c) gear type 2-front side, and (d) gear type 2-rear side.....	67
Figure 4.9: 3D Printed worm: (a) front view, and (b) perspective view showing the key of the worm shaft on the right side.	68
Figure 4.10: 3D printed worm shaft support: (a) and (b) are two different views of the part.....	68
Figure 4.11: 3D printed sensor holder: (a) side view, (b) other view of (a), and (c) front view-before drilled, left side obstructed hole.....	69
Figure 4.12: 3D printed brackets: (a) front view of the bracket showing tree holes, and (b) other view of (a).	69
Figure 4.13: 3D printed stepper motor support: (a) front view of the cap, (b) rear view of the cap, (c) different rear view of the cap, (d) front side of the box support, (e) side view of the box support, are (f) two different views of the part.	70
Figure 4.14: 3D stopper motion pad: (a) front view of the left stopper motion pad, (b) front view of the right stopper motion pad, and (c) other view and size comparison of (b).	70
Figure 4.15: 3D printed solar brackets: (a) front view of the solar bracket left, (b) front view of the solar bracket right, and (c) downside view of (a).	71
Figure 4.16: Electronic and electric circuit of the dual-axis solar tracking system.	74
Figure 4.17: Flowchart of algorithm for light sensing of the automatic dual solar tracking system.	76
Figure 4.18: Flowchart of algorithm for manual positioning of the automatic dual solar tracking system.....	77
Figure 5.1: Worm gear assembly testing.....	80
Figure 5.2: Testing of the sensor holder with full direct sunlight: 35% cloud cover.	81
Figure 5.3: Testing of the sensor holder with full direct sunlight: 1% cloud cover.	82
Figure 5.4: Testing of (a) manual positioning switches, and (b) switches of stopping motion and the right side stopper motion pad.	83

Figure 5.5: Test of the dual-axis solar tracker system.	84
Figure 6.1: Summary of the project cost by categories.	90
Figure 6.2: Prototype cost by percentage contribution of each part category.....	91
Figure 6.3: 3D printing costs.	91

CHAPTER 1

INTRODUCTION AND OVERVIEW

1.1 Introduction

One of the most precious resources in the world, nowadays and specially in the future, is fresh water. This resource is not equally distributed around the world; there are places where water is even scarce. However, there is a large amount of seawater on the earth. Seawater can be converted into fresh water, using a desalination method. Several technologies of desalination process have been created applying physics concepts; some of them are more suitable, convenient, economic and non-contaminant for the purpose requirements than others.

Seawater can be converted into fresh water using solar energy, which has become an easy, suitable and green solution method to obtain heat for seawater desalination. Fresnel lenses have wide applications; one of them is to concentrate energy. It is possible to concentrate the heat flux from the sunlight into a small focal area by using a Fresnel lens. When the focal area is correctly located to an evaporation chamber, the obtained heat from the sun can significantly elevate the temperature of the chamber, and therefore, evaporate the water while setting the salt aside. This water steam can be condensed to produce fresh water for human consumption, helping to solve a tangible scarcity of fresh water issue with a concrete solution.

Seawater has an average salinity of 35 parts per thousand (35 g/l), and its boiling point is at 373.15 K (100 °C). The melting point of copper is at 1,358.15 K (1,085 °C) [1].

Depending on the requirements of fresh water output as a function of time, it is

necessary to design or select the lens to obtain the expected heat at the receiver surface, and to dimension the evaporator in order to have an energy distribution on the entire evaporating chamber.

This project aims to develop a novel dual axis automatic solar tracking system to significantly/efficiently enhance the solar energy harvesting, and therefore, achieve efficient portable water production for desalination. This project combines the mechanical, energy, electronic and electric parts of the Mechanical and Energy Master Program. Also, during the research were used different type of software packages such as MATLAB®, Inventor®, AutoCAD®, SOLIDWORKS®, ANSYS® and COMSOL Multiphysics®.

1.2 Overview

This project is about developing an efficient solar desalination portable technology to obtain drinking water. A Fresnel lens is used to heat a receiver (connected to a water heater) with the purpose to significantly increase the evaporation rate of seawater. Depending on the size (diameter) and the focal length (distance from the lens to the focal area) of the Fresnel lens, the obtained heat varies significantly. The heater system has a principal hollow copper core to act as a heat supplier for the evaporation chamber. The design and size of the core is related to the amount of heat that it can transport and distribute to the chamber, where a uniform distribution of the heat is an important aspect.

The process of the project includes the research, design and simulation, fabrication, testing and tuning the seawater desalination system.

Both topics, fresh water, priority for human rights, and renewable energy are extremely vital and have high global priority for live being considering the current and future global situation.

The research consists of solar energy utilization for water desalination. It uses a concentrator lens to increase the temperature of a chamber to evaporate salty water.

This novel ultra-light and low-cost solar tracking system and solar concentrator also include a novel sensor holder, and stopper motion pad designs. The rotation movement of the system is due to LDS sensors.

The outcome of this project will be a tangible real-solver consumption water global issue, and will bring validated knowledge to the research community and accompany the green mission of UNT.

Results of temperature and heat flux values on the receiver surface obtained in this study can be used as a reference to investigate and apply in other Fresnel lens applications. For several Fresnel lens applications

1.3 Importance and Scope

When the well is dry, we learn the worth of water.
Ben Franklin

From the sun there different form of radiations as illustrated in Figure 1.1. The direct radiation is the most usable type for solar energy applications, such Fresnel lens, solar cooking, PV solar panels, among others.

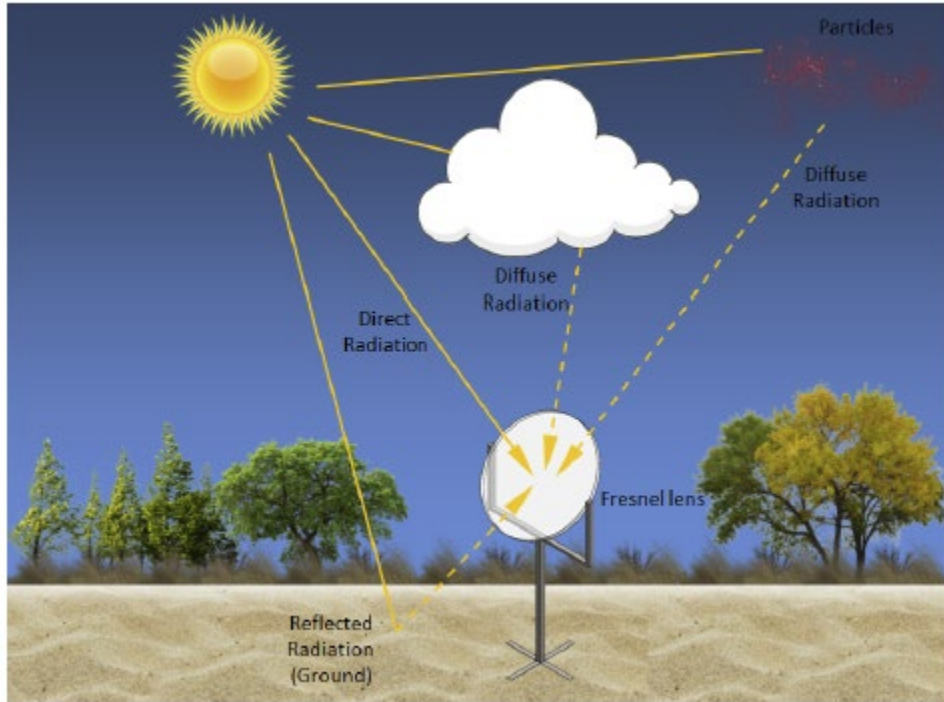


Figure 1.1: Different types of solar radiation beams.

There is an enormous potential for solar energy. Every day the Earth receive, in form of solar energy, about 200,000 times the world's total daily electric-generating capacity [3]. This solar energy is focused approximate between 60° above and below the Equator, Northern Hemisphere and Southern Hemisphere, respectively. The further you move from the Equator and the closer you get to the poles, the less solar radiation you obtain.

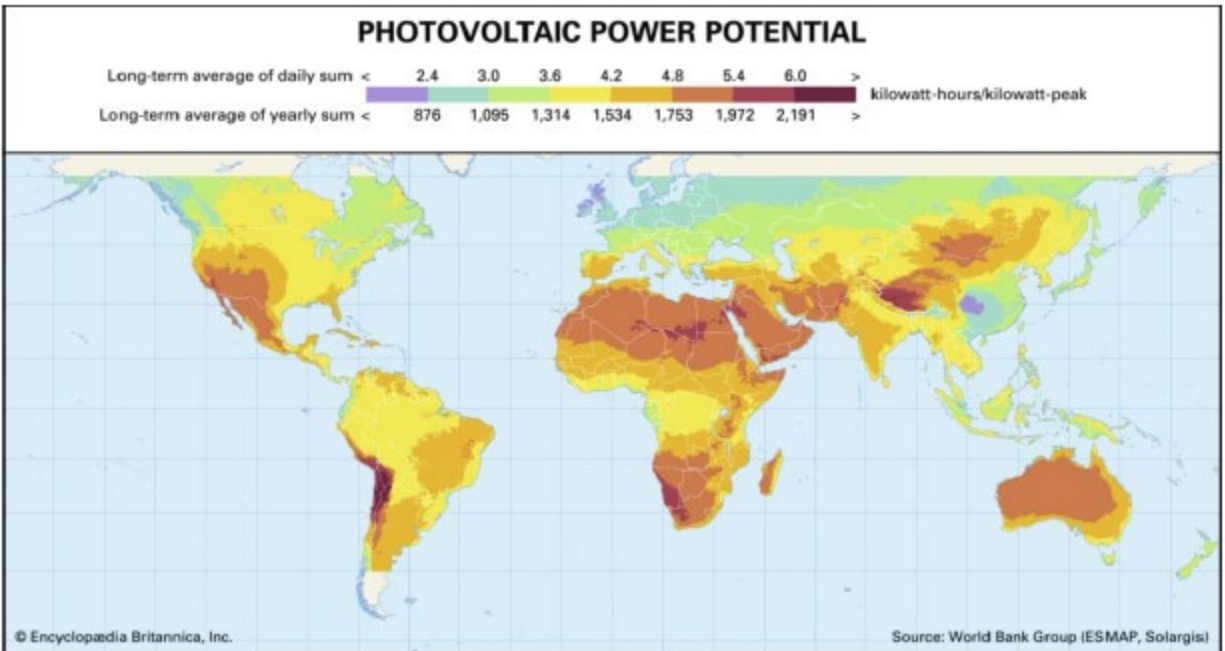


Figure 1.2: Earth’s photovoltaic power potential [3].

In the world there are places where the fresh water is scarce for different reasons, such as geographical areas, big cities with heavy contamination, and poverty areas, that, having abundant water, they cannot afford or make structures that carry the water to a specific place to supply it to the people. This is the main motivation of this project: develop a device that can provide potable water to people that needs it, beyond the reason it is. The project uses sustainable and green source energy: solar energy.

This project can be also oriented to other applications rather than distill seawater. It could be used in applications that need concentration of heat, on and/or outside Earth. Some examples are: solar cooking (also known as solar cooker or solar oven), solar welding, solar Photovoltaic (PV) Pane, solar thermal parabolic trough, solar thermal dish/engine, solar forges, in assemblies using Fresnel lens and solar cells, and solar collectors to heat water for domestic use. It can also be used to generate steam or to power a Stirling engine.

CHAPTER 2

FRESNEL-LENS SOLAR CONCENTRATOR

2.1 Design Parameters

Figure 2.1 shows the diagram with the main flat Fresnel lens parameters considered, and Table 2.1 lists its values. Groove width is equal for all prism grooves, in contrast, prism thickness and incident angle is different for each groove. Focal length is the vertical distance between the lens to the receiver surface, and has the value of $F = 2 \cdot R$, where R is the radius of the flat lens.

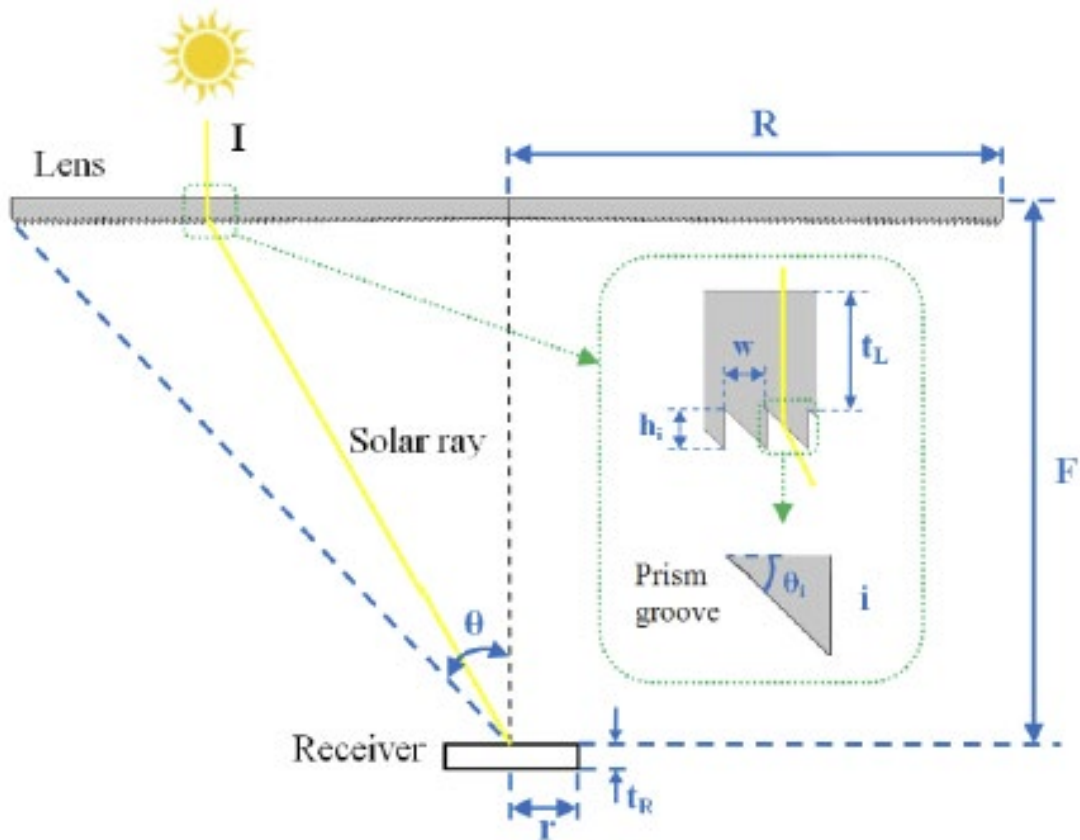


Figure 2.1: Parameters of flat Fresnel lens design.

Table 2.1: Design parameters of the Fresnel lens.

Lens Radius	R	250	mm
Lens thickness	t_L	3	mm
Receiver radius	r	0.75	in
Receiver thickness	t_R	0.5	in
Focal length	F	500	mm
Number of prim grooves in a half-lens	i	50	
Groove width	w	5	mm
Prism thickness	h_i		mm
Incident angle	θ_i		Deg
Incident ray intensity	I	1000	W/m^2

It was selected a hollow steel rod with height of 8.5 inches and 0.026252 inches of thickness. Also, a copper receiver of 0.5 inches thickness and 1.5 inches diameter.

2.2 Simulations

A Flat Fresnel lens and a receiver, with a chamber below it, are used to simulate the seawater desalination system. The flat Fresnel lens was designed based on an algorithmic method using MATLAB®, which provides the high optimization lens measurements, giving the optimum number of grooves and dimensions of each groove, where each groove has different dimensions along the lens. Then it was drawn with CAD software. The algorithm is a result of a PhD Dissertation of Dr. Qandil Hassan [4] [5].

Figure 2.2 illustrates the components of the system that will be used to simulate in the following sections. A close-up view of the flat Fresnel lens shows concentric circles on the underside surface.

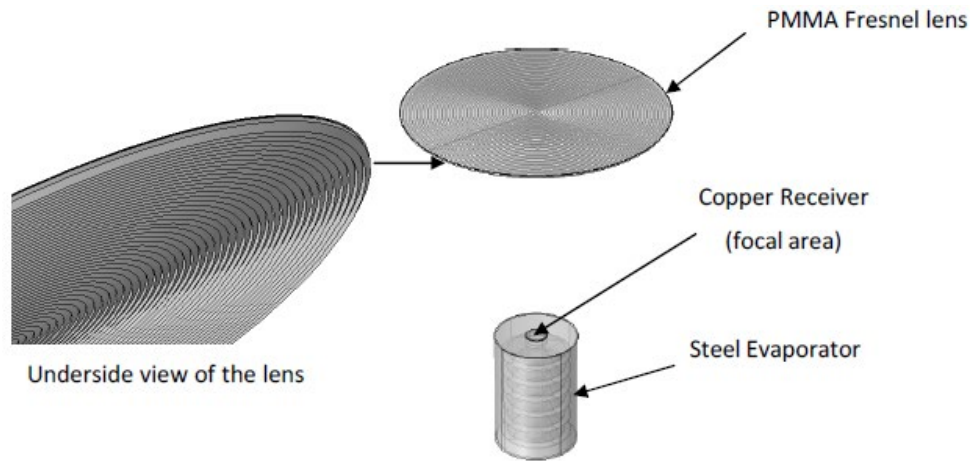


Figure 2.2: Transparent figure of the components.

Thermal and mechanical properties of the material used in this project are described in Table 2.2. The values were taken as defaults provided by the Material Library of COMSOL Multiphysics®. The foam insulation material selected was “Foam solid, 101 kPa”. A foam ring of small thickness was used in Ray Heating COMSOL Multiphysics® simulations where was included the evaporator tank. This ring provides insulation between the short rod of the receiver and the wall of the evaporator tank, avoiding to loss heat to the walls and top the tank.

Table 2.2: Thermal and mechanical properties of materials.

	Heat Capacity at Constant Pressure	Density	Thermal Conductivity	Young's Modulus	Refractive index, real part	Refractive index, imaginary part
	C_p [J/(kg*K)]	ρ [kg/m ³]	k [W/(m*K)]	E [Pa]	n	k
Copper	385	8960	400	110E9	0.25459	3.7096
PMMA	1420	1190	0.19	3E9	1.4878	3E-8
Stainless Steel	475	7850	44.5	200E9	2.75681	3.792016
Foam	Foam solid, 101 kPa - Material Library					
PVC	900	1760	0.1	2.9E9	1.5395	0.0000014400

Refractive index (n) and extinction coefficient (k) values for the copper, PMMA and PVC materials are from refractive index database [6], considering 660 nm vacuum wavelength. These values for the stainless steel are from Filmetrics company [7].

2.2.1 Heat Transfer and Ray Heating

2.2.1.1 Fresnel Lens for Desalination Seawater Application

COMSOL Multiphysics® was used to perform the simulations, applying Heat Transfer in Solids and Ray Heating (Ray Optics) modules.

Temperature and heat flux values can be obtained using a Fresnel lens, concentrating and focusing the rays on a focal area, the receiver.

2.2.1.1.1 Heat Transfer

Heat Transfer in Solids simulates only the temperature propagation and distribution in the heating chamber using a Gaussian pulse to simulate the sunrays energy (heat flux) applied to the receiver. The Gaussian function parameters were calculated running an algorithmic method using MATLAB® [4] [5]. This provides an idealized result.

Next Figure 2.3 shows the results obtained applying heat transfer simulation. Part (a) illustrates the temperature distribution in the receiver and chamber, with a maximum of 903.74 K. As visualization, on (b) a 3D plot of the Gaussian function is located directly above on the receiver. The temperature distribution along the receiver surface follows the behavior of the Gaussian function, concentric with a peak in the center, see part (c). In less than 30 minutes, the chamber achieves the maximum temperature and remains constant for the 4 hours simulation, see part (d).

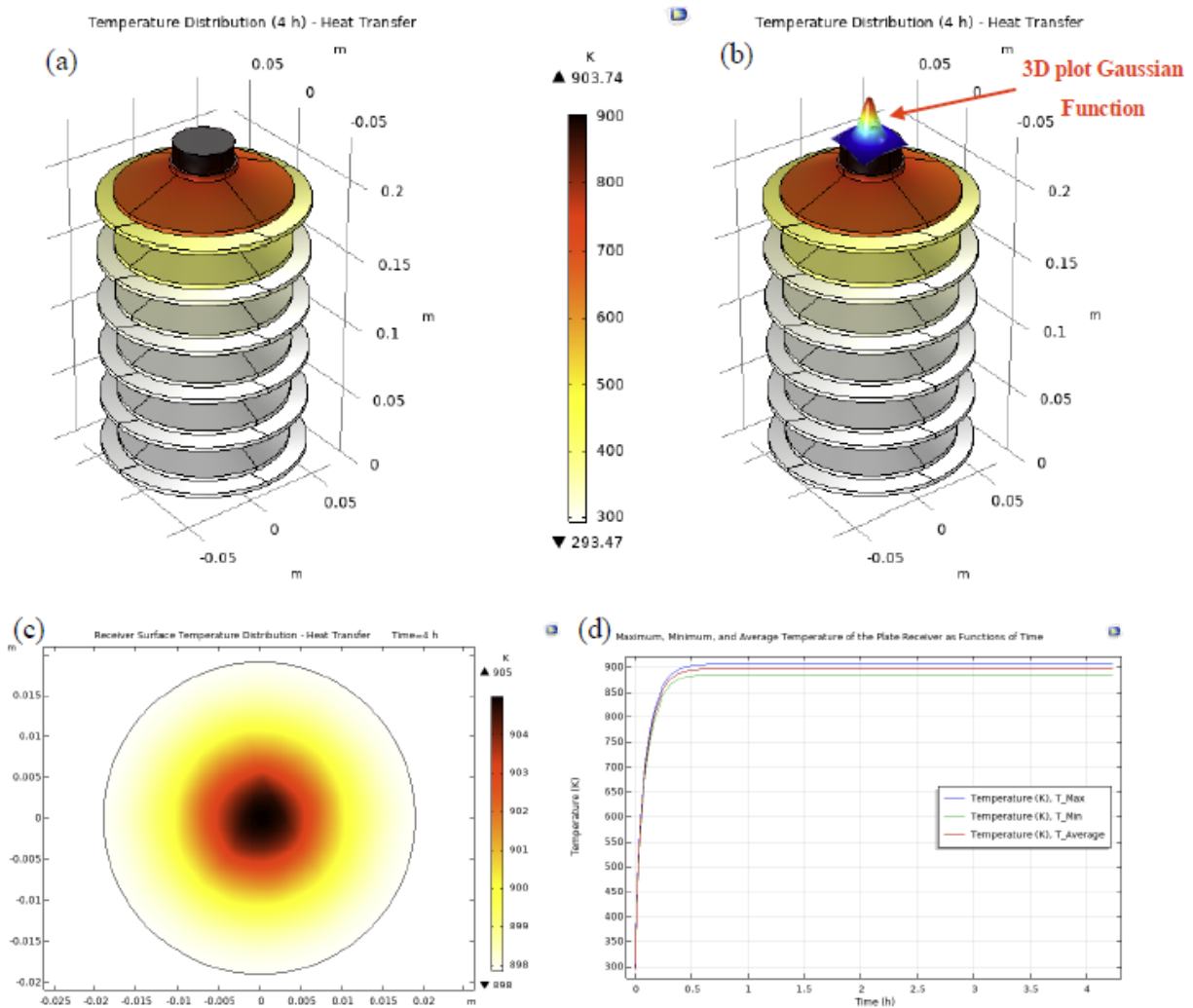


Figure 2.3: Heat transfer simulation results for 4 hours: (a) 3D chamber temperature distribution using heat transfer by applying Gaussian function, (b) schematization of the Gaussian function on the receiver surface, (c) temperature distribution along the receiver surface (top view), and (d) 1D maximum, minimum and average temperature of the plate receiver as functions of time.

Notice that this project does not consider the design of the chamber and evaporator tank; they only appear as a reference to visualize a part which is located below the receiver, being the main component concern of study in this project. However, this helps to have an idea of the evaporator temperatures. The evaporator design concerns to a UNT Master student, Bridger Planz.

Table 2.3 lists the parameters used in heat transfer simulations.

Table 2.3: Heat transfer parameters.

Initial temperature	T	293.15	K
Reference temperature	T _{ref}	293.15	K
External temperature	T _{ext}	293.15	K
Heat transfer coefficient	h	Defined for each component	W/(m ² *K)
Absolute pressure	P _A	1	atm
Thermal conductivity	k	from each material	W/(m*K)
Density	ρ	from each material	kg/m ³
Heat transfer at constant pressure	Cp	from each material	J/(kg*K)

2.2.1.1.2 Ray Heating

Ray Heating simulates the chamber and lens heat propagation and distribution due to sunrays, real sunrays energy (heat flux) applied on the receiver and ray trajectories. This simulation provides results that resemble real behavior.

Table 2.4 lists the parameters used in ray heating simulations.

Table 2.4: Geometrical optics parameters.

Incident ray intensity	I	1000	W/m ²
Total source power	P _{src}	1000	W
Vacuum wavelength	λ ₀	660	nm
Refractive index, real part	n	from each material	
Refractive index, imaginary part	k	from each material	

Figure 2.4 illustrates the temperature distribution and the ray trajectories. There is a concentric focus on the receiver surface of ray trajectories. For 4 hours simulation, the maximum was 810 K.

The temperature distribution along the receiver surface is concentric with a peak of 813.12 K, and follows the shape of the Gaussian function. See Figure 2.5 (a). On (b) the curve shows the shape of the temperature distribution along the receiver diameter surface following also the shape of a Gaussian function.

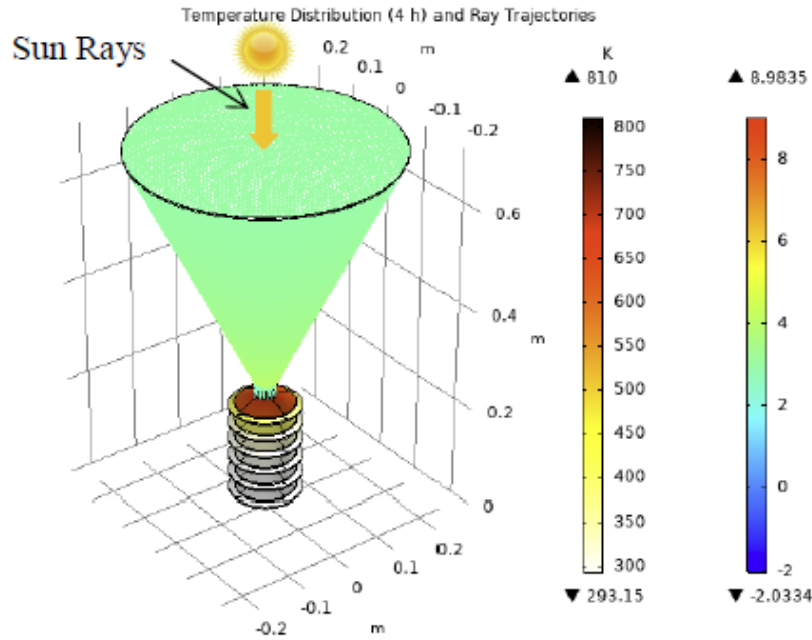


Figure 2.4: 3D Temperature distribution and ray trajectory using ray heating.

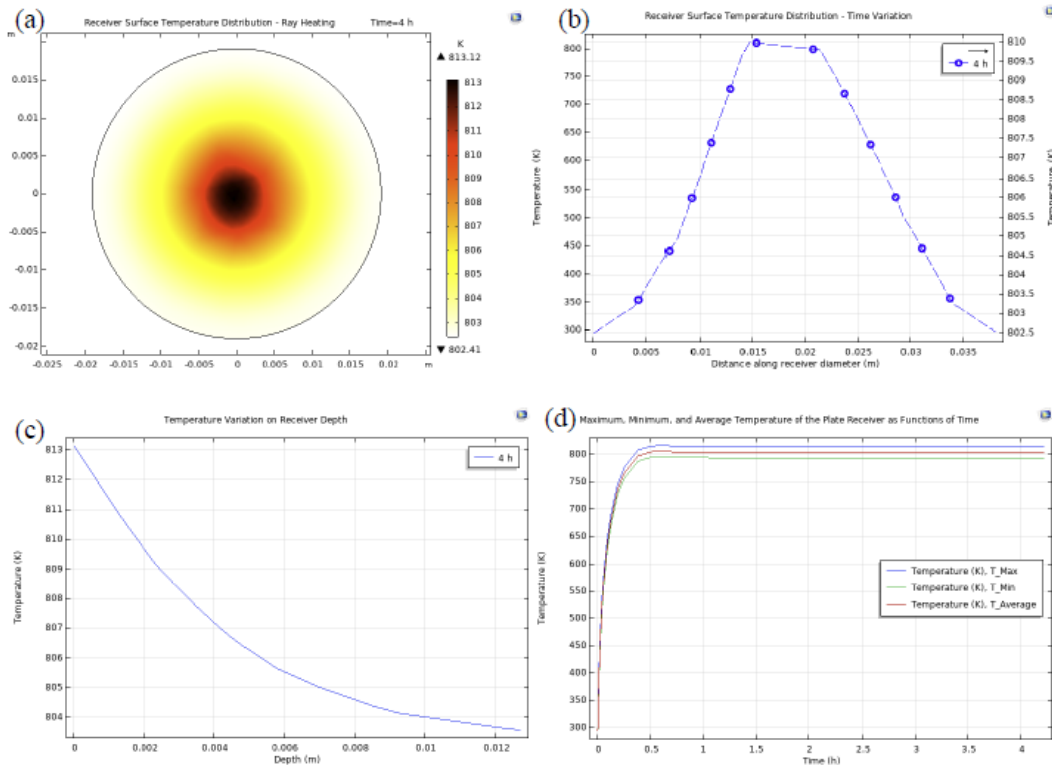


Figure 2.5: Ray heating temperature results for 4 hours: (a) 2D receiver surface temperature distribution (top view), (b) curve of temperature distribution along the receiver surface, (c) 1D receiver depth temperature, and (d) 1D maximum, minimum and average temperature of the plate receiver as functions of time.

The decreasing temperature on the receiver as function of its depth is illustrated on Figure 2.5 (c), from the top of the receiver surface to the plane that starts the rod surface, is losing approximate 10 K. (d) shows that the maximum temperature is reached before of 30 minutes of 4 hours simulation.

The inward heat flux distribution along the receiver diameter illustrated in Figure 2.6 (a), matches the peak of heat flux in (b). This peak of $1.28 \times 10^6 \text{ W/m}^2$ is reached much before 0.1 hour, following also a Gaussian function's shape, remaining the maximum value until the 4 hour simulation.

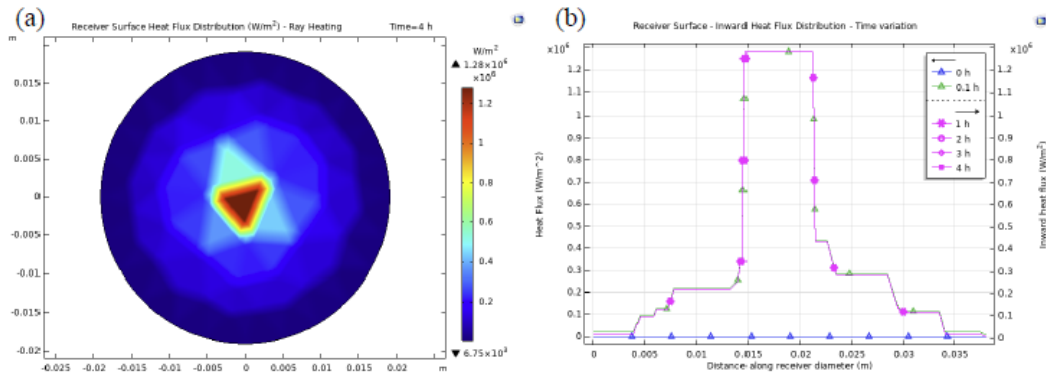


Figure 2.6: Ray heating heat flux results for 4 hours: (a) 2D receiver surface heat flux distribution (top view), and (b) 1D receiver surface inward heat flux distribution along the receiver diameter as function of the variation time.

As conclusion, temperature values applying heat transfer are higher than using ray heating simulations.

2.2.1.2 The Importance of the Receiver Diameter and Thickness, Rod Design and Thickness, and the Structure Design below the Receiver

The diameter and thickness of the receiver, as well as the rod thickness and design take importance at the moment of the design of the evaporator or the component on which the solar heat will be focusing. The temperature and homogenous temperature obtained will

depend on these factors.

Regarding to the design of the rod, in the case of the evaporator design, a hollow design demonstrates better performance compared to a solid one. In addition, if parts are added inside or outside of the rod, the temperature will decrease. This has the advantage of the use of less material, therefore cheaper final project costs. In a previous research presented on ASME-IMECE 2020 [1], were compared the combination of using a 70 cm and 120 cm diameter, for each case using flat and curved Fresnel lenses, and hollow and solid rods. For both diameters and lens shapes, hollow rod obtained higher maximum temperatures than solid design.

Regarding to receiver diameter and thickness and rod thickness, the following studies compares, analyzes and simulates the combination of three different receiver diameters with three different receiver thickness and with three different rod thickness. There are in total 27 combinations.

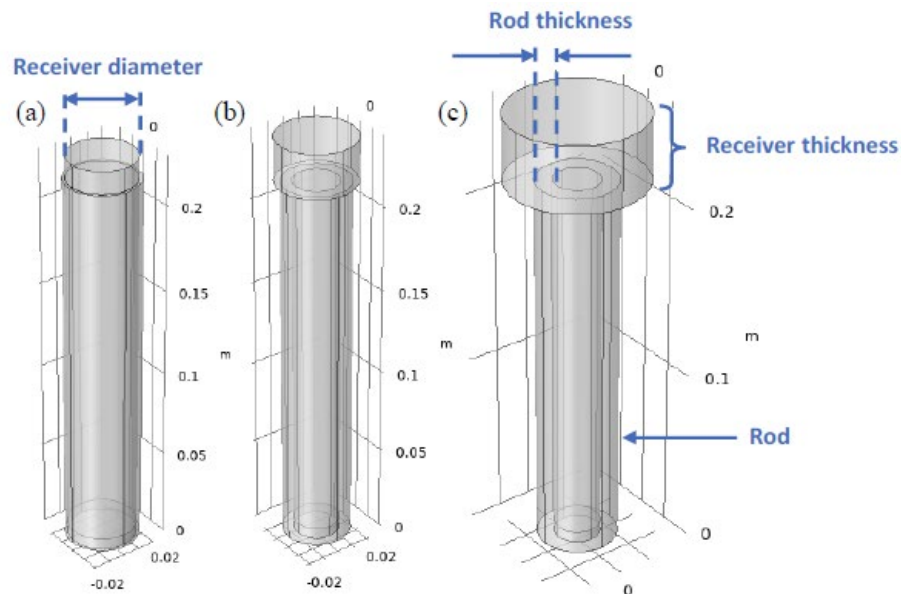


Figure 2.7: Three examples of receiver diameter and thickness, and rod thickness: (a) 1.5 in receiver diameter with 0.5 in receiver thickness and 0.06252 in rod thickness, (b) 1.75 in receiver diameter with 1 in receiver thickness and 0.25 in rod thickness, and (c) 3 in receiver diameter with 1.5 in receiver thickness and 0.366 in rod thickness.

Figure 2.7 illustrates one example of 1.5 inches receiver diameter with 0.5 inches receiver thickness and 0.06252 inches rod thickness, one example of 1.75 inches receiver diameter with 1 inches receiver thickness and 0.25 inches rod thickness, and lastly, one example of 3 inches receiver diameter with 1.5 inches receiver thickness and 0.366 inches rod thickness.

Using the MATLAB® code [4] [5], for each 1.5, 1.75 and 3 inches diameter receivers, was obtained the Gaussian functions and the design parameters to then, drawn using AutoCAD® each flat Fresnel lens that is used to simulate this section study.

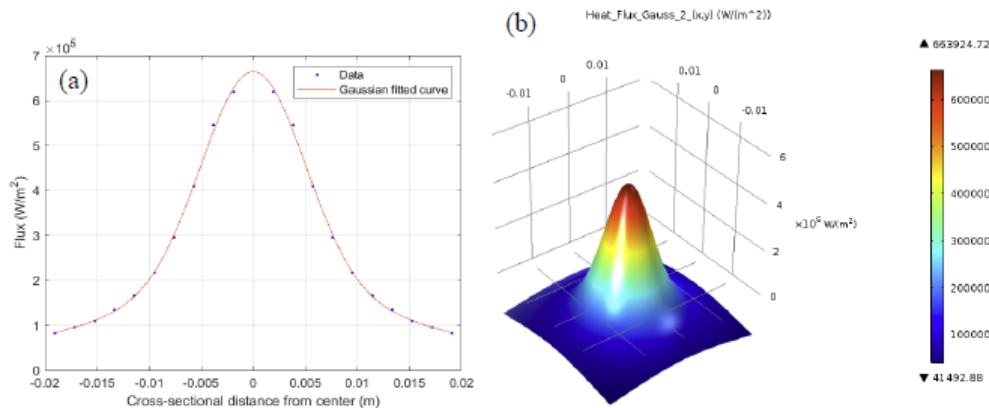


Figure 2.8: Diameter receiver: 1.5 in, 500 mm diameter Fresnel lens with 500 mm focal length: (a) MATLAB® plot of the Gauss function of second order, and (b) 3D receiver surface inward heat flux distribution using Gaussian function of (a).

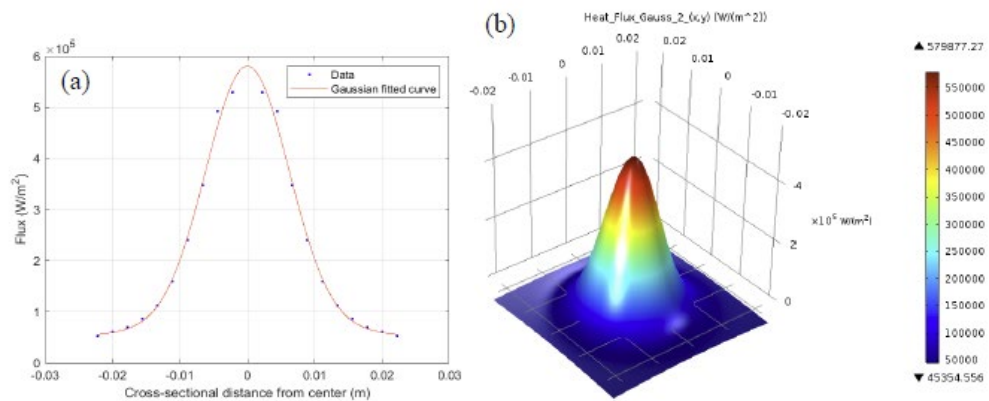


Figure 2.9: Diameter receiver: 1.75 in, 500 mm diameter Fresnel lens with 500 mm focal length: (a) MATLAB® plot of the Gauss function of second order, and (b) 3D receiver surface inward heat flux distribution using Gaussian function of (a).

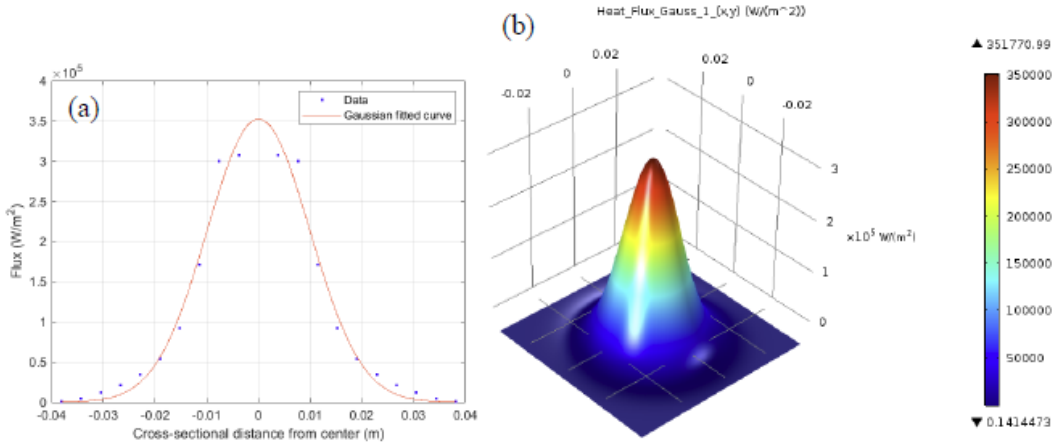


Figure 2.10: Diameter receiver: 3 in, 500 mm diameter Fresnel lens with 500 mm focal length: (a) MATLAB® plot of the Gauss function of second order, and (b) 3D receiver surface inward heat flux distribution using Gaussian function of (a).

From Figures 2.8-2.10 (a), when the receiver diameter increased, decreased the heat flux, from around 6.5×10^5 [W/m²] considering a diameter of 1.5 inches to 3.5×10^5 [W/m²] in a 3 inches diameter. This pattern also is reflected on Figures 2.8-1.10 (b). In addition, from 1.5 to 3 inches receiver diameter, see parts (a) of Figures 2.8-2.10, the Gaussian fitting curve goes from good to fair good fitting. Similarly, Table 2.5 shows that also, in all cases, increasing the receiver diameter, decrease the total energy received at the receiver, lens efficiency, overall lens efficiency and transmittance values. MATLAB® code provides these parameters.

Table 2.5: Total energy at the receiver, efficiencies and transmittance lens for three different receiver diameters.

		Receiver Diameter [in]		
		1.5	1.75	3
Total energy received at the receiver	W	191.08	190.48	186.76
Lens efficiency	%	97.32	97.01	95.11
Overall lens efficiency	%	91.06	90.65	88.19
Overall lens transmittance	%	93.57	93.44	92.72

In total, 54 simulations were performed to construct the Tables 2.6 and 2.7 and Figures 2.11 and 2.12, 27 heat transfer and 27 ray heating simulations, respectively. In all cases was

considered a steel hollow rod height of 8.5 inches. Copper material was used for the receiver. In this study, the evaporator was not included in the simulations.

Table 2.6: Maximum temperatures results combining three different receiver diameters, receiver thickness, and rod thickness, applying heat transfer.

Receiver Diameter inches	Receiver Thickness inches	Rod Thickness inches	Max. Temperature K	Rod Thickness inches	Max. Temperature K	Rod Thickness inches	Max. Temperature K
1.5	1.5	0.06252	872.86	0.25	655.44	0.366	592.33
	1		885.44		656.35		591.00
	0.5		903.74		658.05		590.04
1.75	1.5	0.06252	836.63	0.25	648.84	0.366	585.51
	1		852.11		651.88		585.97
	0.5		872.12		656.49		588.29
3	1.5	0.06252	758.63	0.25	610.23	0.366	558.45
	1		783.70		620.02		564.28
	0.5		810.28		630.28		571.23

Table 2.7: Maximum temperature and receiver surface heat flux results combining three different receiver diameters, receiver thickness, and rod thickness applying ray heating.

Receiver Diameter [inches]	Receiver Thickness [inches]	Rod Thickness [inches]	Max. Temperature [K]	Receiver Heat Flux [W/m ²]	Rod Thickness [inches]	Max. Temperature [K]	Receiver Heat Flux [W/m ²]	Rod Thickness [inches]	Max. Temperature [K]	Receiver Heat Flux [W/m ²]
1.5	1.5	0.06252	785.74	1.28E+06	0.25	602.85	1.28E+06	0.366	548.60	1.28E+06
	1		794.80	1.28E+06		604.28	1.28E+06		546.93	1.28E+06
	0.5		810.00	1.28E+06		606.51	1.28E+06		546.76	1.28E+06
1.75	1.5	0.06252	751.94	1.14E+06	0.25	594.51	1.16E+06	0.366	539.23	1.14E+06
	1		764.95	1.12E+06		597.93	1.19E+06		539.83	1.12E+06
	0.5		782.39	1.35E+06		603.63	1.34E+06		542.98	9.72E+05
3	1.5	0.06252	681.07	1.74E+05	0.25	558.37	1.74E+05	0.366	511.88	1.74E+05
	1		700.94	1.82E+05		566.51	1.81E+05		516.57	1.82E+05
	0.5		724.82	1.85E+05		575.33	1.59E+05		521.89	1.77E+05

Regarding to heat transfer simulation, results from the combination of comparing the temperatures achieved using 1.5, 1.75 and 3 inches receiver diameter, 0.5, 1 and 1.5 inches receiver thickness, and 0.06252, 0.25, and 0.366 inches rod thickness, show that a 1.5 inches receiver diameter in all the three dimensions rod thickness and receiver thickness, obtain the highest temperatures. On the other hand, 3 inches diameter receiver presents the lowest temperatures in all combinations of receiver and rod thickness. Moreover, considering a rod thickness of 0.06252 inches, using a 1.5 inches receiver thickness, the loss of heat between 1.5 and 3 inches receiver diameter is 114.23 K, being higher than using a 0.5 inches receiver thickness, 93.45 K. Figure 2.11 illustrates clearly this analysis. Each Gaussian Pulse function,

obtained previously for 1.5, 1.75 and 3 inches receiver diameter, was used to simulate the sunrays energy on the receiver.

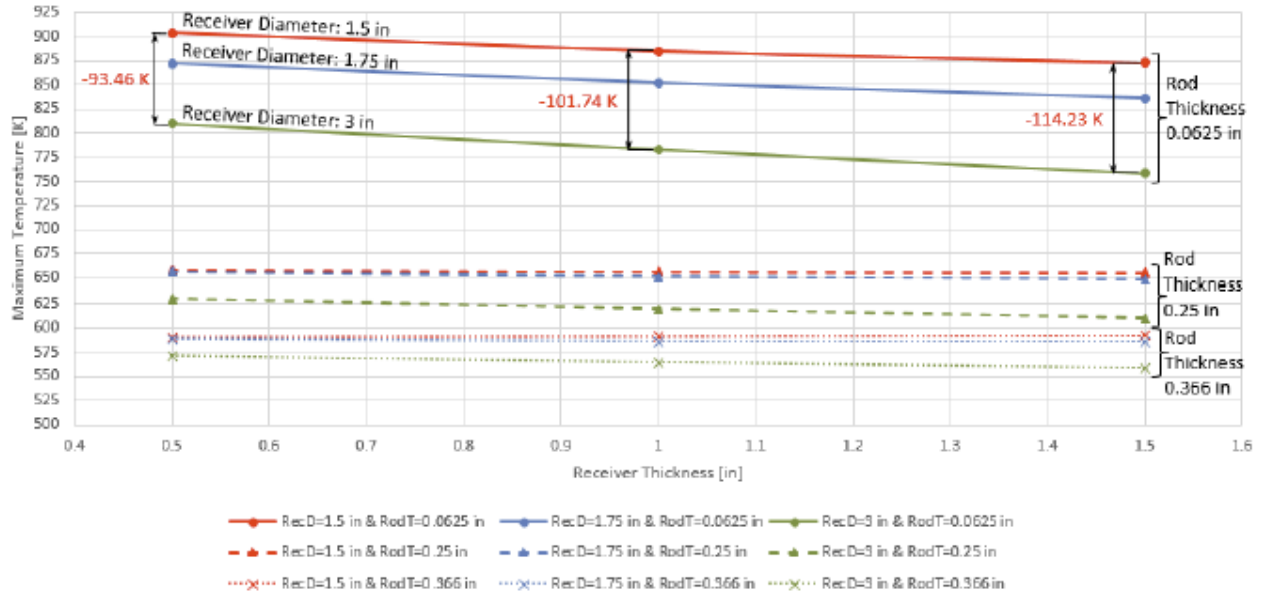


Figure 2.11: Maximum temperature results combining three different receiver diameters, receiver thickness, and rod thickness, applying heat transfer.

Regarding to ray heating simulation, performing the same analysis with the same dimensions previously mentioned, results show very similar behavior to heat transfer simulation results with Gaussian function. Figure 2.11 and Figure 2.12 (a) have the same values on x- and y-axis, to easily visually the difference between the highest temperature value applying heat transfer and ray heating is 93.74 K, considering 1.5 inches receiver diameter, 0.5 inches receiver thickness and a rod thickness of 0.06252 inches. In general, temperature values applying Gaussian function are higher than ray heating, but the difference between the two methods is within the same order of magnitude. For 1.5 and 3 inches receiver diameter, heat flux values remain constants for all receiver and rod thickness. 1.75 inches receiver diameter presents a little variation among the three receiver diameters. See Figure 2.12 (b). In a previous

research presented on COMSOL Conference 2020 [8], was compared a 120 cm diameter flat and curved Fresnel lenses. The flat lens, as in this study, presented values of temperature and heat flux also were higher applying heat transfer than ray heating. In addition, these results match the conclusion of the previous section.

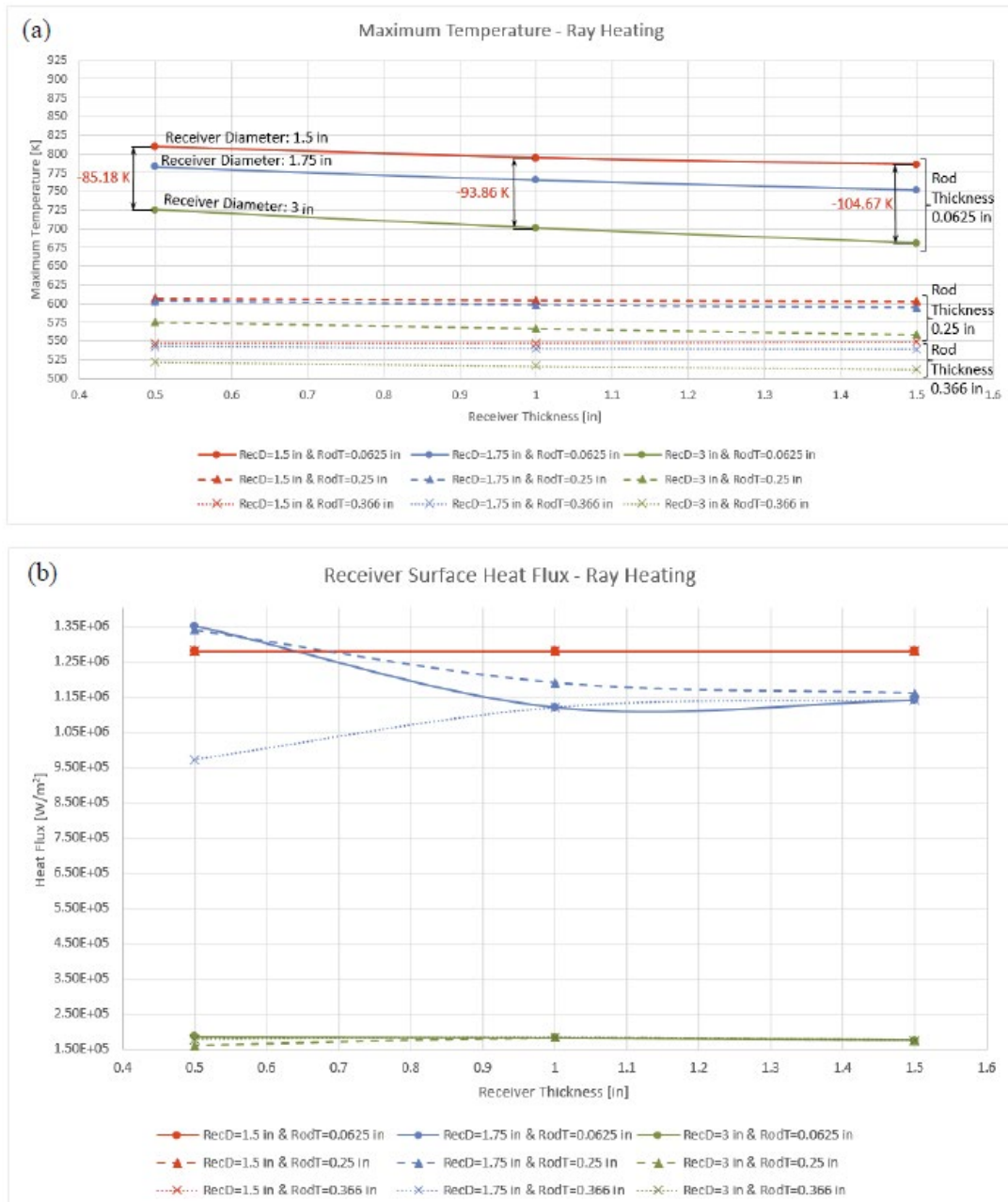


Figure 2.12: (a) Maximum temperature results combining three different receiver diameters, receiver thickness, and rod thickness, and (b) receiver surface heat flux for three different receiver diameters, receiver thickness, and rod thickness. both applying ray heating.

Based on the above analysis, from here in this project, it considers a 1.5 inches receiver diameter, 0.5 inches receiver thickness, and 0.06252 inches hollow rod thickness in further COMSOL Multiphysics® and SOLIDWORKS® simulations. Results show that these dimensions provide better values on both heat transfer and ray heating simulations.

2.2.2 Ray Heating: Fresnel Lens for Other Applications

This section provides an idea of the temperature values that can be obtained applying ray heating simulation using a flat Fresnel lens with previous features applied to other type of applications. It could be used in a range of applications, such as solar welding ray-heating, solar cooking, on Earth and outside it (Mars, Moon), for instance, build base camps and structures using solar welding, among others, such as mentioned in section 1.3. Next figure provides an idea of the amount of heat that can be obtained. Moreover, using a 1.5 inches receiver diameter and thickness, the temperature reached is 2,333.98 K, being near or higher for most melting points of metal materials.

The present project, the dual-axis solar tracker system, can be used for different applications aside from seawater evaporation to obtain fresh water.

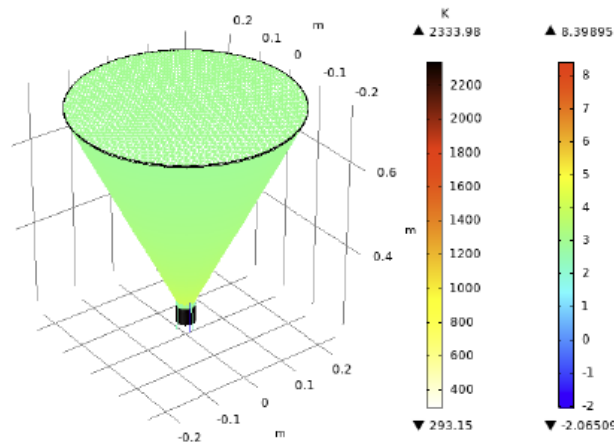


Figure 2.13: Ray heating applied to a 1.5 inches receiver diameter and thickness.

2.2.3 Wind Speed Velocity and Pressure

In this project, the Fresnel lens could be the part/component of the solar tracker that could create dynamic forces due to wind forces on it and on its supporting structure, because it is located at the highest part of the solar tracker system, making angle rotations in azimuth and elevation directions. Simulations considering the wind can provide values of maximum velocities and pressures that are actuating on the component, and also their locations on the part to have considerations at design time.

According to the Enhanced Fujita Scale (EF Scale) [9], winds of 65-85 mph are considered tornados of level EF-0 with light damage.

2.2.4 Analysis of Fresnel Lens Only

A studying of velocities and pressures due to wind was done considering only the Fresnel lens and an adverse inclination angle of it (40° respects to the ground plane). Table 2.8 shows the maximum values of pressure obtained for different wind speed values. The simulations considered turbulent flow. These nine wind simulation results are plotted on Figure 2.14, which can be fitted by a second order polynomial with $R^2 = 1$. Clearly, when the wind speed increases, the pressure values also increase in a smooth behavior.

Table 2.8: Maximum values of pressure for different wind speed values.

[mph]	Wind Speed		Max. Pressure [Pa]
	[km/h]	[m/s]	
5	8.05	2.24	6.23
10	16.09	4.47	24.79
18	28.97	8.05	80.46
30	48.28	13.41	223.77
40	64.37	17.88	398.89

[mph]	Wind Speed		Max. Pressure [Pa]
	[km/h]	[m/s]	
44	70.81	19.67	483.40
50	80.47	22.35	625.49
60	96.56	26.82	904.64
72	115.87	32.19	1,311.47

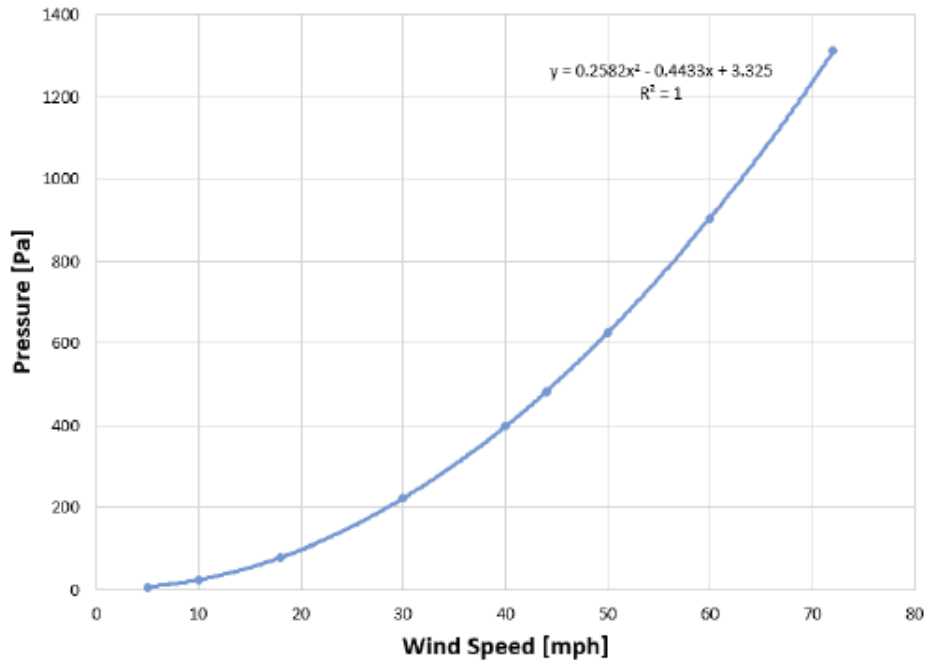


Figure 2.14: Second order polynomial fitting maximum pressure versus wind speed.

Figure 2.15 illustrates an example of wind simulation on the lens surface applying a wind speed of 44 miles per hour (mph)

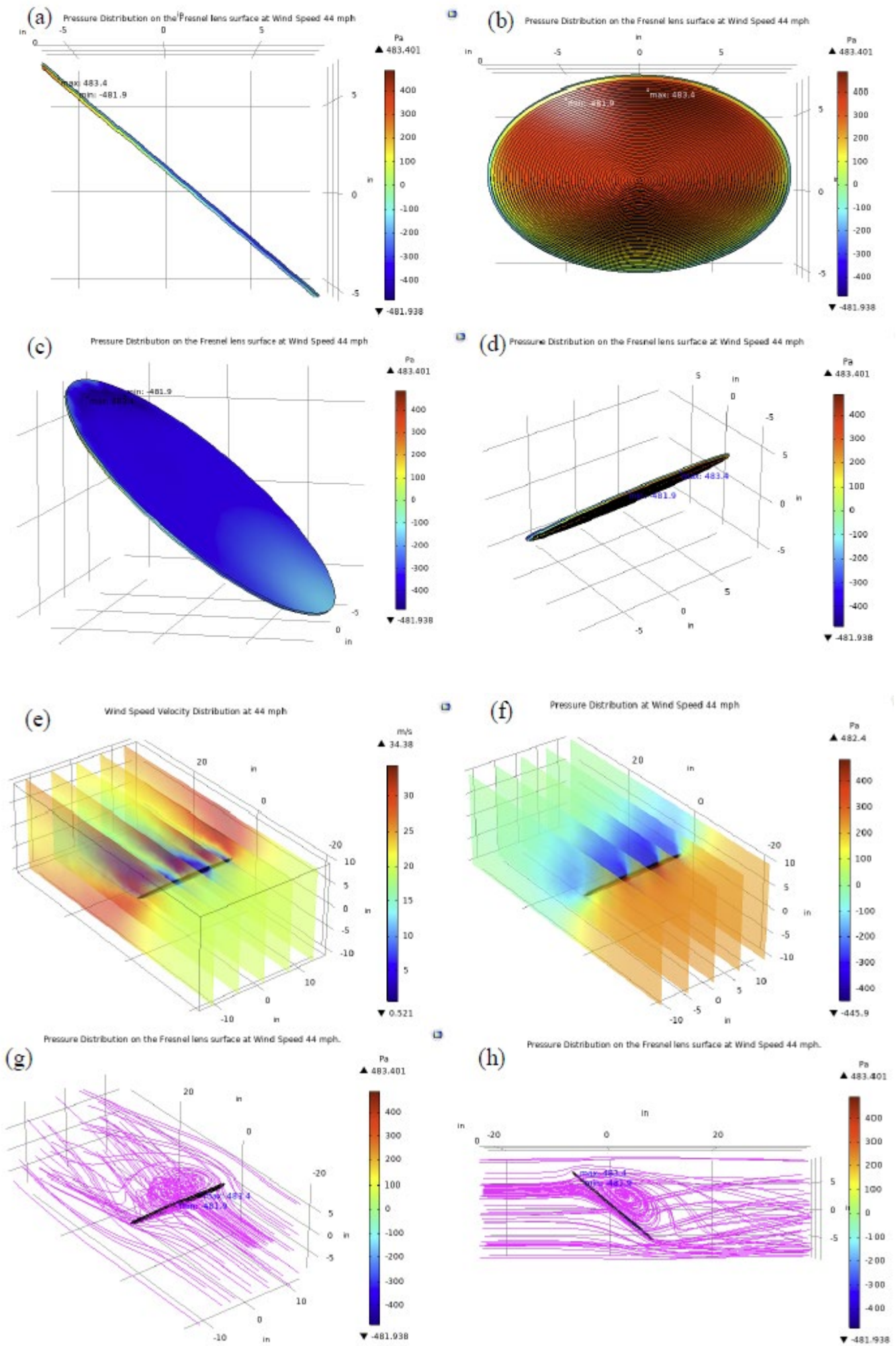


Figure 2.15: Wind simulation on the Fresnel lens surface applying a wind speed of 44 mph: (a)-(d) Different views of the lens showing the pressure distribution and maximum and minimum pressure locations, (e) and (f) Sliced view of wind speed velocity and pressure distribution around the lens, and (g) and (h) Wind streamline flow showing the maximum and minimum pressure values.

CHAPTER 3

DUAL-AXIS SOLAR TRACKING SYSTEM

3.1 Introduction

In order to get the expected energy concentrated on the evaporator, the Fresnel lens has to face perpendicular to the sun rays. As the sun moves through the day and year, it is necessary to provide some logic to perform mechanical movements to follow the sun.

The difference in luminosity in four LDR sensors is sensed by a microcontroller. Its logic drives two stepper motors in such a way to position the Fresnel lens facing to the sun with the sensors. It could be necessary, sometimes, to properly position the device; for this, a set of manual controls can override the operation of the light sensors, allowing to operate the tracker as desired.

This project presents a novel Dual Axis Solar Tracker (DAST) design. The LDR sensors command the rotation movements along the day, using a novel sensor holder and stopper motion pad.

3.2 Literature Review

According to recent literature, 42.57% of the analyzed studies present and discuss single axis tracking systems while 41.58% of these studies discuss dual axes tracking systems. In addition, only 12.22% of the studies use or apply dual-axis solar tracking techniques [10]. Single axis systems have better performance than fixed ones, and dual axis over single axis systems. A dual axis provides higher accuracy and improves the overall capture of solar power by 30-60% compared to single axis. For instance, an overall increase of 30-45% can be obtained using dual axis instead fixed PV systems [10]. Similar results were obtained by authors [11] [12] [13] [14].

A literature review about solar tracker systems was made, including a total of 30 recent publications (see Table 3.1). Publications about the application of Fresnel lens are much less frequent compared to solar panels. Seventy percent of the 30 publications is based on photovoltaic solar applications, 17% for other applications rather than PV panels and Fresnel lenses, and 13% use Fresnel lens for a project. See Figure 3.1.

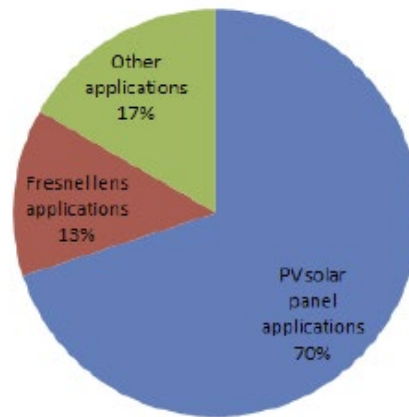
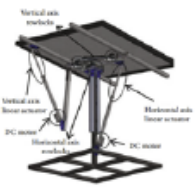



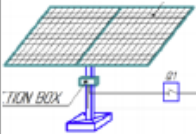

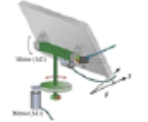






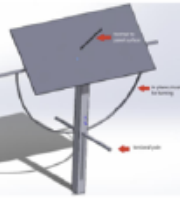


Figure 3.1: Number of publications based on tracking application.

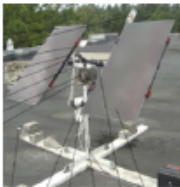
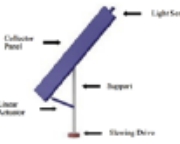
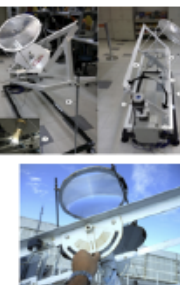
Table 3.1: Summary of solar tracker literature review.



Reference	N ^o	Publication Name	Journal	Year	Author/s	Solar Tracking Method	Tracking Application	Movement Concept	Project Picture
[21]	1	Development of a machine vision dual-axis solar tracking system	Elsevier. Solar Energy 160 (2018) 136–143.	2018	Masoumeh Abdollehpour, Mahmood Reza Goltarlan, Abbas Rohani, Hossein Abotorabi Zarchi	Dual Axis	PV Solar Panel	A camera captures images of a bar shadow to track the Sun. In the moment that when an opaque object comes into the path of light, the light rays stop, then a dark area (shadow) appears where the object blocks the light. The system automatically detect the shadow location within one of the four quarters of the trigonometric circle, and then calculate the panel angle to orient it vertically in direction of the irradiation. Accuracy: ± 2°.	
[10]	2	Solar tracking systems: Technologies and trackers drive types—A review	Elsevier. Renewable and Sustainable Energy Reviews 91 (2018) 754–782.	2018	A. Z. Hafez, A. M. Yousef, N. M. Harag	Dual Axis	PV Solar Panel	It uses two PMDCs (Permanent Magnet Direct Current). One to change the tilt angle (β) to move in the direction North–South. The other to change the azimuth angle (α_w) to move in the direction East–West. The changes between two axes acted by switching on and off the PMDC motors.	
[15]	3	Dual Axis Solar Tracking System in Perlis, Malaysia	Journal of Telecommunication, Electronic and Computer Engineering. 2018. eISSN: 2289-8131. Vol. 10 No. 1-14.	2018	R. S. Zulkefli, A. S. Bewazir, N. A. M. Amin, M. S. M. Hashim, M. S. A. Majid, N. F. M. Nasir	Dual Axis	PV Solar Panel	Light Dependent Resistors (LDR) sense the position of the Sun. They communicate to a microcontroller. An algorithm controls the DC geared motor. Two DC geared motors are used to rotate and position the solar panel to always perpendicular to the Sun. Not use shadow concept.	

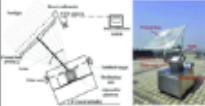


[22]	4	Evaluation and Design of Power Controller of Two-Axis Solar Tracking by PID and FL for a Photovoltaic Module	Hindawi. International Journal of Photoenergy. Volume 2020, Article ID 8813732, 13 pages. https://doi.org/10.1155/2020/8813732 .	2020	Joel J. Ontiveros, Carlos D. Ávalos, Faustino Loza, Néstor D. Galén, Guillermo J. Rubio	Dual Axis	PV Solar Panel	A gyroscope on the surface of the module that determines its position with respect to the hour angle and altitude of the sun. Two PMDCs (Permanent Magnet Direct Current). One change the tilt angle (North-South movement) and the other change the azimuth angle (East-West movement). The changes between two axes acted by switching on and off the PMDC motors.	
[16]	5	A Mechanical Design of an Altitude-Azimuth Two Axis Solar Tracking System for Sakarya, Turkey	International Journal of Mechanical Engineering and Robotics Research Vol. 7, No. 1, January 2018.	2018	Cayda Aksoy, Cenk Yavuz	Dual Axis	PV Solar Panel	Two linear actuators and linkages. The linear actuator converts the circular motion of an electric motor into linear motion. Altitude-azimuth tracking system. It uses equations.	
[17]	6	IoT based dual-axis solar tracking system	3rd International Conference on Advances in Mechanical Engineering (ICAME 2020), IOP Conf. Series: Materials Science and Engineering 912(2020) 032024. doi:10.1088/1757-899X/912/3/032024	2020	R. Vinodhkumar, Stalin John	Dual Axis	PV Solar Panel	IoT maneuver and remote monitor the orientation of the solar panel. An accelerometer and gyroscope sensor are used to check if the solar tracker is oriented correctly with the given angle. Two motors and two gears to rotate the axes.	
[18]	7	Design and Performance Evaluation of a Dual-Axis Solar Tracking System for Rural Applications	EJCE, European Journal of Electrical and Computer Engineering, Vol. 3, No. 1, January 2019. DOI: http://dx.doi.org/10.24018/ejce.2019.3.1.52 .	2019	Hachimenu Nyebechi Amadi, Sebastián Gutiérrez	Dual Axis	PV Solar Panel	Two set of light dependant resistor (LDR) sensors, direct current (DC) motors and microcontroller. One set LDR (placed on either side of the panel separated by an opaque plate) and one motor is used to tilt the tracker in the Sun's East-West direction. The other set of LDR and the second motor (fixed at the bottom of the tracker) are meant to tilt the tracker in the Sun's North-South direction. It uses the shadowed concept.	

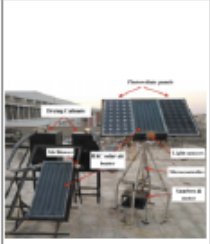

[23]	8	Operational experience of a Solar Power Plant with a Dual-Axis Solar Tracking System in the conditions of the Southern Urals	E3S Web of Conferences 124, 01022 (2019). https://doi.org/10.1051/e3s/conf/201912401022	2019	S. V. Mitrofanov, D. K. Baykasevov, A. U. Nematsev	Dual Axis	PV Solar Panel	It uses LDRs, but they leads to incorrect operation of the solar tracking system. So, to improve the reliability of the heliotracker and minimize the error of pointing to the sun, is needed the use of a GPS to track the Sun.	
[19]	9	An Improved Sunflower-Inspired Solar Tracking Strategy for Maximizing Photovoltaic Panel Power Generation	International Journal of Recent Technology and Engineering (IJRTE) ISSN: 2277-3878, Volume-8 Issue-2, July 2019. DOI: 10.35940/ijrte.81013.078219.	2019	Roxel U. Sabren, Arnel C. Fajardo	Single Axis	PV Solar Panel	Stepper motors, microcontroller, real time clock module and current sensor. Overall average tracking error: 0.114°.	
[20]	10	Date/Time Operated Two Axis Solar Radiation Tracking System for Baghdad City	International Journal of Applied Engineering Research ISSN 0973-4562 Volume 13, Number 7 (2018) pp. 5534-5537.	2018	Dr. Anas Leheef Mahmood	Dual Axis	PV Solar Panel	A microcontroller control two stepper motors. An algorithm uses the date/time mode. The computer calculates the Sun's position from formulae and send the signals to the motors.	
[11]	11	Evaluation of Photovoltaic Solar Power of a Dual-Axis Solar Tracking System	Journal of Southwest Jiaotong University, Vol. 55 No. 1, Feb. 2020. ISSN: 0258-2724 DOI: 10.35741/issn.0258-2724.55.1.52.	2020	Ali Sabri Alhw, Ikhlas Hameem Shellal	Dual Axis	PV Solar Panel	A microcontroller, two DC servo motors, a gearbox, two angle sensors, a timer circuit, a Bluetooth unit, motor module, control circuit and four LDR. It uses the shadowed concept. Small size.	
[24]	12	A Two-Dimensional Solar Tracking Stationary Guidance Method Based on Feature-Based Time Series	Hindawi. Mathematical Problems in Engineering Volume 2018, Article ID 3420649, 12 pages https://doi.org/10.1155/2018/3420649 .	2018	Keke Zhang, Chaoming Si, Zhencai Zhu, Chongbin Guo, Qi Shi	Dual Axis	PV Solar Panel	Two-dimensional solar tracking stationary guidance system. The tracking system is based on a time series model and a microsatellite platform. The sun position is calculated using equations, and the results are sent to the driving motors.	
[25]	13	Sun Following Solar Panel	Degree Project in Technology. Stockholm, Sweden 2018.	2018	Colin Lawless, Erik Kärrfelt	Dual Axis	PV Solar Panel	Two stepper motors, two stepper motor driver, a microcontroller and four LDR. The concept of shadowing is used.	

[26]	14	Remote Triggered Single-Axis Solar PV Tracking System with Varying Angle of Incidence	International Journal of Renewable Energy Research. M. Umesh et al., Vol.8, No.3, September, 2018.	2018	M. Umesh, Joshua Fraeman, Krishnashree Achuthan, Balakrishnan Shankar	Single Axis	PV Solar Panel	A DC unipolar stepper motor, a stepper motor driver card, a current sense, a data acquisition unit, a stepper motor gear and an external ring gear. The tracking angle is calculated using the NREL algorithm.	
[27]	15	Solar Tracking with Anti-Tracking Support for Ancillary Service	Conference Paper. June 2019. DOI: 10.1109/PVSC40753.2019.8980560.	2019	M. Zinaddinov, S. Mil'shtein	Single Axis	PV Solar Panel	Use quadrant photodetector. Shadow of a beam. One motor. Change the sun position in both elevation and azimuth. Power is applied to the torsional pole by a locally installed motor. The torsional pole moves the in-plane shoulder gear and the horizontal pole on which a solar module is resting tilts either to the left or to the right.	
[12]	16	An Automatic Multi-axis Solar Tracking System in Ramadi City: Design and Implementation	Indonesian Journal of Electrical Engineering and Computer Science. Vol. 19, No. 3, September 2020, pp. 1126-1234. ISSN: 2502-4752. DOI: 10.11591/ijeecs.v19.i3.pp1126-1234.	2020	Mustafa Hamid Al-Jumaili, Hussain M. Haglan, Mohammed Kareem Mohammed, Qusay Hatem Eteee	Dual Axis	PV Solar Panel	Four LDR (two for vertical movement and two for horizontal movement), super Jack motor and microcontroller. The controller compare the values from LDRs, the structure will move to the direction of the highest value.	
[13]	17	Implementation of Solar Tracking Design Using FPGA Tool	2019 International Conference on Computing, Mathematics and Engineering Technologies – ICoMET 2019.	2019	Izhar Ahmed Sohu, Syed Abid Ali Sheh Bukhari, Asif Ahmad Rahimoon, Arslan Ahmed Sohu, Asadullah Shaikh	Dual Axis	PV Solar Panel	Field Programmable Gate Array (FPGA) use four modules: digital clock, module for sunrise time, 2 pulse generator for altitude angle, and 2 pulse generator for azimuth angle. Two stepper motors (motor 1 changes the azimuth angle along the East-West direction, whereas motor 2 changes the elevation angle along the North-South direction), two horizontal gears and controller.	

	20	Solar Tracking Stand for Solar Panels and Collectors	Engineering for Rural Development. Jelgava, 23.-25.05.2018.	2018	Henriks Putans, Imants Ziemelis, Ilze Pelece, Andrejs Snegovs	Dual Axis	PV Solar Panel	It uses a solar sensor infrared diodes and a PV solar radiation indicator light sensor. A single motor with gearbox (change the length of their push bars in relation to the post) turns the frame with panels to the sun in vertical (zenith) and horizontal (azimuth) plane. The concept of shadowing is used. The device has to be intended periodically annually rotate in the zenith plane. Accuracy $< \pm 2^\circ$ (clear day).	
	21	Design and Development of a Laboratory-Scale Dual-Axis Solar Tracker System	International Journal of Engineering Research. September 2020.	2020	Junkun Ma, Min Joe Suh	Dual Axis	Solar energy collectors	Based on a slewing drive, an ambient light sensor with a built-in voltage divider, two microcontrollers and a linear actuator.	
	22	Solar tracker development based on a PCF bundle and Fresnel lens applied to environment illumination and microalgae cultivation	Elsevier. Solar Energy 174 (2018) 648-659.	2018	Regina Célia Allil, Alfredo Mancheço, Alexandre Allil, Igor Rodrigues, Arthur Werneck, Gisel Chenard Diaz, Fabio Toshio Dino, Yordanka Reyes, Marcelo Werneck	Dual Axis	POF bundle and Fresnel lens (microalgae cultivation and illumination of internal ambience)	A Fresnel lens is fixed at the main axis. Algorithm that calculates the Sun position based on the time of year, the longitude and the latitude of the location. In addition, sensors measure the right ascension and declination angles of the tracker and the solar radiation. It needs manually adjustment of the declination angle which allows the tracker to be directed to the sunrise direction. A microcontroller, a stepper motor, photodetector and an accelerometer. Average error $< 1^\circ$.	

[32]	23	Efficient and Low-Cost Arduino based Solar Tracking System	IOP Conf. Series: Materials Science and Engineering 745(2020) 012016. DOI: 10.1088/1757-899X/745/1/012016.	2020	Sohaib R. Awad, Mamoon A. Al Jbaar, Mohammed A. M. Abdullah	Dual Axis	PV Solar Panel	A microcontroller, two servomotors and eight LDRs. According to the light intensity, the servomotor would move the solar panel to the location of the maximum intensity captured by the LDR. The solar tracker has 9 positions vertically and 3 positions horizontally. The improvement of using 2-Axis solar tracker was 25% better compared to an immobile solar panel.	
[33]	24	A testbed of intelligent Sun tracking system and thermoelectric generator with Fresnel lens at solar cell system for maximizing generated energy	Journal of Physics: Conference Series. International Conference on Renewable Energy (ICORE) 2019. 1595 (2020) 012017. DOI: 10.1088/1742-6596/1595/1/012017.	2020	M. Muliadi, M. P. A. Jalil, A. Arpriharta, I. Fadlika, S. Hidayat, S. Sendari, A. N. A. Afandi, G. J. Horng, W. M. Utomo	Single Axis	Fresnel lens and solar cell (Intelligent Mobile Thermophotovoltaic (IMT))	Drivers move or rotate the motor 9 degrees per step for every 30 minutes. The optimum angle of this system is calculated by counting the angle of irradiation with the corner of the cross-section of the solar panel or the lens to obtain a 90° angle. Thermoelectric generator, Fresnel lens, solar panel, motor drive and heatsink.	
[34]	25	Performance evaluation of solar Fresnel lens cooker	Journal of Pharmacognosy and Phytochemistry 2019; 8(6): 2427-2431. E-ISSN: 2278-4136.	2019	BAU Dere, SR Kalbande, AJ Dhandge	Dual Axis	Fresnel lens solar concentrator (FLSC) (cooking)	Fresnel lens tracks the sun using a solar tracker. Lens, solar panel, two motors, heat exchanger, cooking pot with fluid pipe network and insulation. The lens is fixed on the heat exchanger. The system is powered by PV panels.	

[35]	26	Simulation and Experimental Study on the Optical Performance of a Fixed-Focus Fresnel lens Solar Concentrator Using Polar-Axis Tracking	MDPI. Energies. Energies 2018, 11, 887. DOI: 10.3390/en11040887	2018	Hai Wang, Jin Huang, Mengjie Song, Yanxin Hu, Yunfeng Wang, Zijian Lu	Polar Axis	Solar concentrator (Fresnel lens + polar-axis tracking system)	Fixed-focus Fresnel lens solar concentrator (FFFSC) using polar-axis tracking which allows the Fresnel lens to concentrate sunlight to a fixed small heat-receiving area and the receiver remained fixed in location and rotation. DC gear motor (controls the rotation of the polar axis that holds the entire system), manual lead screw adjustment device, solar pyranometer, an adjustable platform, a diffuse flat receiver, a CCD (charge-coupled device) camera and an absorptive-reflective neutral density filter (ND-filter). Polar-axis tracking unit: ±0.1° accuracy, ±75° and 1.5% error.	
[36]	27	Solar-tracking methodology based on refraction-polarization in Snell's window for underwater navigation	Chinese Journal of Aeronautics. https://doi.org/10.1016/j.cja.2021.02.011	2021	Pengwei Hu, Jian Yang, Lei Guo, Xiang Yu, Wenshuo Li		Underwater autonomous navigation	The solar position is determined by Underwater Polarization Pattern (UPP) which describes the spatial distribution of polarized light and is highly correlated with the solar position. Underwater solar-tracking algorithm is developed based on the underwater refraction-polarization pattern inside the Snell's window.	
[37]	28	Design and optimization of solar tracer with U-PRU-PUS parallel mechanism	Mechanism and Machine Theory 155 (2021) 104107	2021	Xiaoqiang Du, Yuechan Li, Pengcheng Wang, Zenghong Ma, Dangwei Li, Chuanyu Wu	U-PRU-PUS parallel	PV Solar Panel	The U-PRU-PUS parallel mechanism has two rotational DOFs about x-axis and y-axis, respectively. It consists on a moving platform, a static platform, a PUS chain, a PRU chain and a fixed-U chain. A motor controller and two motor drivers. Solar tracking error: < 2°.	

[38]	29	Incorporation of a solar tracking system for enhancing the performance of solar air heaters in drying apple slices	Renewable Energy 167 (2021) 070-084	2021	Ramadan ElGamel, Sameh Kishk, Salim Al-Rejale, Gamal ElMasry	Single Axis	Solar air heaters in drying apple slices using PV Solar Panel	It includes a drying cabinet, an air blower, RAC solar air heater, two light sensors, microcontroller, gearbox & motor, and two solar panels. The solar collector of the air heater will remain in a certain position when light intensity received by both light sensors is equal. If light intensity received by one sensor was different from the other sensor (due to movement of the sun), it means the sun moved to a new position and the whole collector should be rotated to face the sun in this new position.	
[39]	30	Experiment study of a hybrid concentrated photovoltaic/thermal(CPV/T) system	IOP Conf. Series: Earth and Environmental Science 657(2021) 012096. doi:10.1088/1755-1315/657/1/012096	2021	Shunxiang Zhang, Peng Li, Qi Luo, Yuntao Chen	Dual Axis	Hybrid concentrated photovoltaic/thermal(CPV/T)	A light sensor is equipped to detect and feedback the solar position. It includes a Fresnel lens and roll-bond heat collector.	

Regarding errors of tracking and accuracy, the following summarizes the efficiencies reported from the literature review. The work from authors [10] shows that the error tolerance of the position of the sun was between 0.5° to 1°. In addition, Wang et al. designed an automatic sun tracking system for parabolic solar concentrator using a PLC and hydraulic drive; the tracking error of the system was less than 0.6°. Abdallah and Badran showed a solar still with sun tracking system for improve the productivity by 22% compared to a fixed solar still, and an increase of overall efficiency by 2%.

The power obtained was 166.5 W for fixed solar tracker and 241 W for the dual axis solar tracker, representing 44.7% more power obtained in the dual axis sun tracking system when compared to the fixed solar tracking [15]. Fathabadi suggested a sensorless altitude-azimuth tracking system with a tracking error of 0.43° [16].

Authors [17] mentions that by placing four LDRs at each side of the photovoltaic panel, the sun can be tracked with ± 4% degree precision.

A dual axis tracking system (DAST) produces 31.4% more energy than the single axis tracking system (SATS) calculated by power conversion efficiencies (PCE), and 67.9% more than the fixed PV panel system (FPPS) [18].

On [19] an overall average tracking error was 0.114° (Clear: 0.124° , partly cloudy: 0.143° , cloudy: 0.191°), and the percentage power gained over a fixed tilted panel was 23.58%. Authors of [20] mention that methods that use the calculation of the solar position show error of $\pm 0.01^\circ$ in the calculations of the solar zenith and azimuth angle, and some of these methods are only valid for a specific number of years. For instance, calculations by Michalsky presented uncertainty greater than $\pm 0.01^\circ$ and Blanco-Muriel et al.'s with uncertainty greater than $\pm 0.01^\circ$. The best uncertainty achieved for a Solar Position Algorithm (SPA) to calculate the solar zenith and azimuth angle is described by Jean Meeus showing uncertainties equal to $\pm 0.0003^\circ$.

The values of accuracy, efficiency and error of tracking above listed can be used as guidelines for the present project.

There are publications about the design and study of Fresnel lenses; however there are fewer publications about projects where a Fresnel lens is used, and for a specific application. Clearly, it is field to expand.

Three projects similar to this work were found in the literature review. Allil et al. [31] suggested a dual axis solar tracker system based on POF bundle and Fresnel lens applied to microalgae cultivation and illumination of internal ambience. The Fresnel lens is fixed at the main axis, and, because the Sun rises every day in a slightest different position at the horizon, this axis has to be adjusted by a few degrees each day. Considering that this displacement is very small compared to the focus area, it can be manually adjusted every five days. The

structure was built using metal materials, and requires external source of energy to work. The structure appears to be larger compared with the work presented here, not portable nor dismantable, and heavy. Also, it does not have an empty area directly below of the Fresnel lens. The total cost of the project is \$5,000.

Dere et al. [34] presented a Fresnel lens solar concentrator (FLSC) for cooking application. The Fresnel lens is fixed on the heat exchanger. The metal structure appears to be heavy and larger than on this work, without an empty area directly below of the Fresnel lens, difficult to transport, and not dismantable. It is powered by PV panels.

Wang et al. [35] suggested a fixed-focus Fresnel lens solar concentrator (FFFSC) using polar axis tracking technique. To guarantee the tracking accuracy, the declination angle in the north-south direction was manually adjusted. The structure was built using metal materials, making it heavy and corrosion prone. It does not present an empty area directly below of the Fresnel lens, is difficult to transport, not dismantable, and requires external source of energy. The bottom platform is adjustable performing the inclination angles.

The three projects above mentioned have some weakness in the structural area, such as they are of metal, and therefore prone to corrosion, and heavy, neither dismantable nor portable due that generally the parts are welded. Regarding to application area, they are only designed to perform one specific application. In terms of costs, in general dual axis solar trackers systems are expensive in the order of thousands of dollars.

Besides of the azimuth and elevation rotation angles objectives, the project design presented in this work can fill the gaps in current solar tracker designs and techniques due to the incorporation of innovative features. The design presented in this work can be used for

more than one application (including distilled seawater). Some examples of applications are mentioned on section 1.3. The present design has an empty area right below of the lens, and some advantages over the previous designs, such as it works off-grid (electrical), use green energy (solar powered), is portable and dismountable, presents small size, is corrosion resistant and was designed in the way that the wires (electrical connection) are placed inside the pipes with the purpose to not obstruct or limit the rotation movements. Also, it automatically follows the sun, meaning that does need manual adjustment. The design is low cost and lightweight.

3.3 Overall View of the Project

3.3.1 CAD Model

The solar tracker system project has more than 400 parts, and all of them were drawn in detail and scale for this project.

Figure 3.2 shows an overall view of the solar tracker system, including the Fresnel lens and the evaporator. The SOLIDWORKS® model exhibits a preview of the design, showing the PVC structure, Fresnel lens, 3D printed parts in black color, location of the evaporator, worm-gear assembly, PV solar panel, and the controller box. Pictures show the interior of the controller box, the project from two view perspectives, and two views of upper frame of the structure representing a most unfavorable position regarding to inclination angle.

On the Figure 3.3, the COMSOL Multiphysics® model illustrates a cone of green rays between the lens and the receiver shows the ray trajectories simulating the sun rays. The rays created from the Fresnel lens are commented and focused very well on the receiver surface.

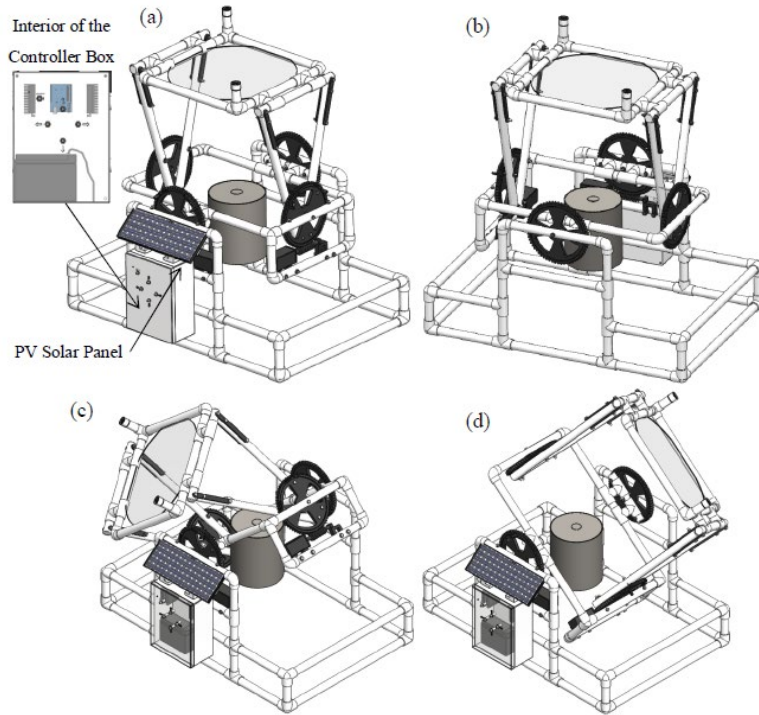


Figure 3.2: (a) Overall CAD model view of the dual-axis solar tracker system showing the interior of the controller box, (b) a different perspective of (a), (c) and (d) most unfavorable position regarding to inclination angle, being closer in a corner of the solar tracker.

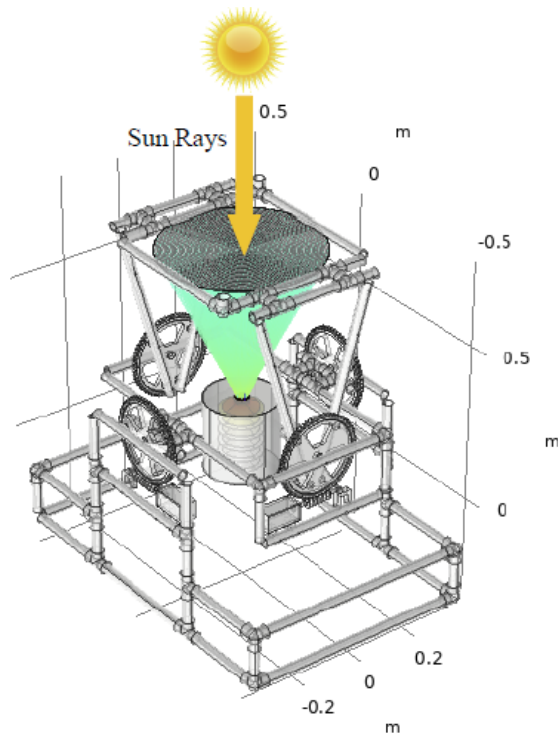


Figure 3.3: 3D Overall view of the dual-axis solar tracker system showing the rays trajectories focusing and concentrating on the receiver surface.

3.3.2 Fabrication Model

Figures 3.4 and 3.5 show the fabrication project finished main parts and dimensions, as well as different perspective views. The structure has 46 x 36 x 48 in.

More detailed information about different parts of the project is presented on the rest of this chapter and in chapter 4. In section 6.1 is given a detailed list of parts used in the project with total cost and total weight. For each component, the list also includes the quantities, unit weight and unit cost.

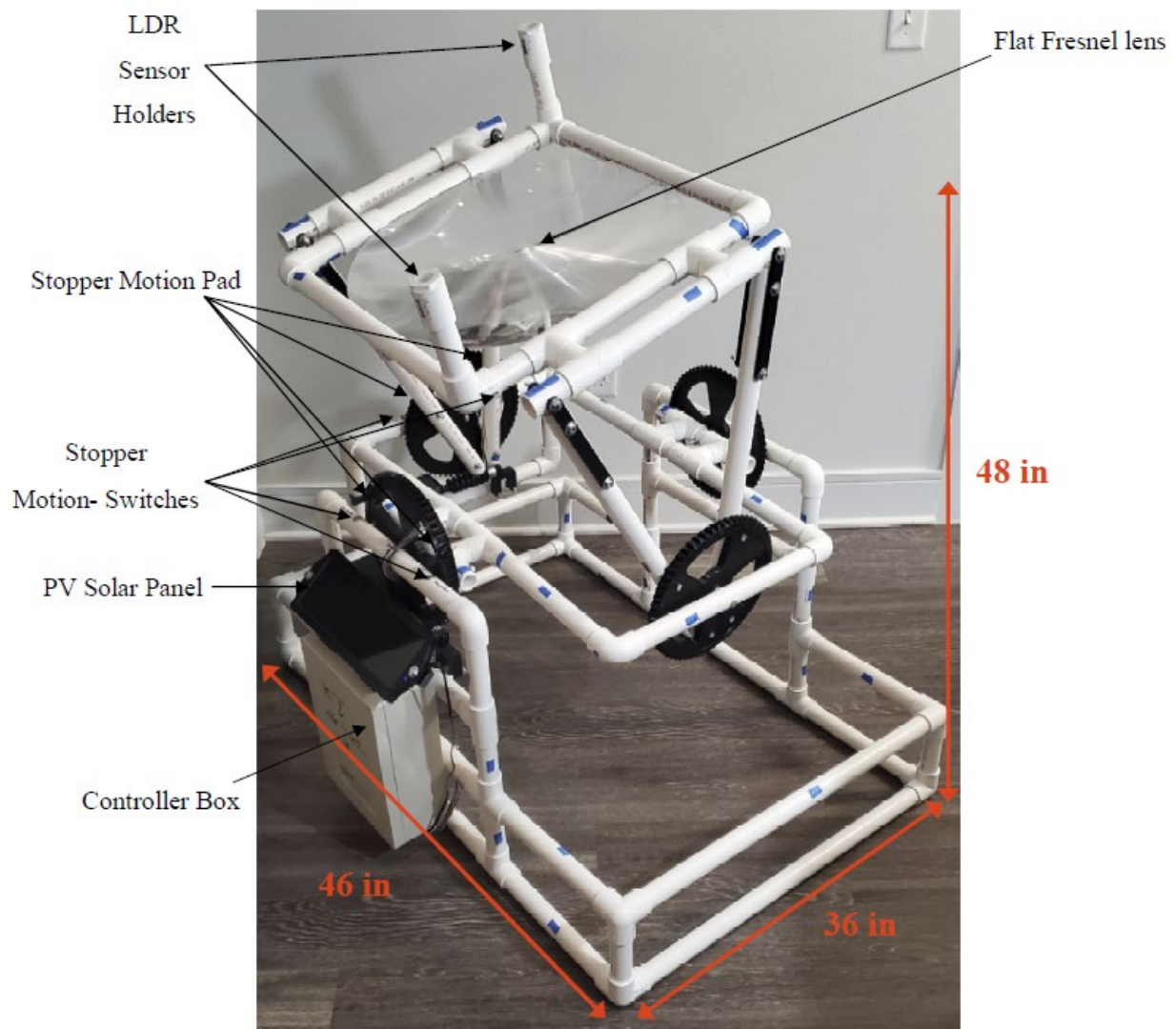


Figure 3.4: Solar tracker system project.



Figure 3.5: (a) – (c) Different perspectives of the solar tracker project.

3.4 Design

The dual-axis solar tracker was designed with the main objectives that the structure was portable, dismountable, lightweight, low cost and corrosion resistant. Also, the structure design should have an empty area directly below of the Fresnel lens (no obstacles on incoming sun rays to the receiver). It was selected PVC material and 3D printed parts as majority portion of the structure.

A total of 400 parts conform the project. The PVC structure is of pipes and deferent types of elbows. Also, includes bolts, washers, nuts and 3D printed parts such as gears, worms, stepper motor box, worm shaft holders, sensor holders, stopper motion pad, brackets, and solar brackets. 3D printed parts were detailed custom design for the project, and are made of ABS material.

The general design of the structure has frames shapes, layout in the ground without the needed of rotation of the base to follow the sun during the day. Selecting a circular base of the structure to rotate would have needed a more complex and expensive base design, more expensive mechanical devices to support the movement of the all structure weight, and presents issues with inlet and outlet pipes of water supply and vapors and internal movements of fluids and vapors created for the rotation.

3.4.1 Static Equilibrium Momentum Analysis

The simplified model of the project on Figure 3.6 is used as guide to perform the static equilibrium momentum analysis. The evaporator was excluded from the calculation because it is on the ground and it is not attached to the solar tracker structure.

To perform the analysis, it was selected the worst angle of inclination of the upper frame; this way, the majority part of the weight of the entire structure is located on one side.

For the analysis, it was considered the weight parts that most influence in the stability of the structure. The maximum value of Fresnel lens pressure due to wind, 483.4 Pa, was selected from the results of section 2.2.3.1. The weight of 0.337 kg in the figure corresponds to the two gears which are in parallel in the plane, faced with each other.

The sum of all moments with respect a point is equal to zero, point 1 and 2 in the diagram.

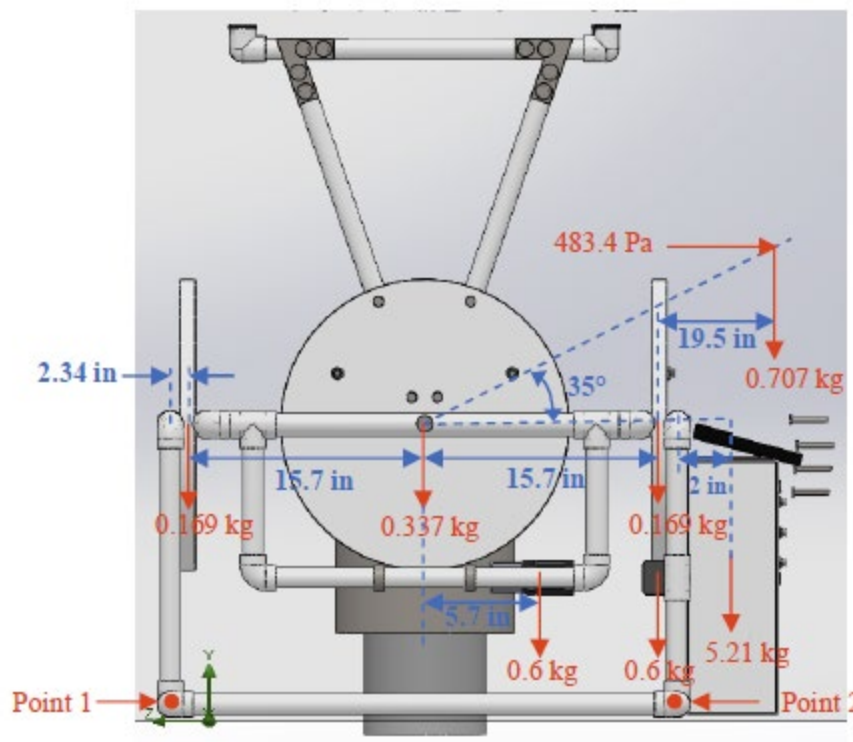


Figure 3.6: Diagram of dimensions and forces for the DAST.

- Maximum Fresnel lens Pressure Wind: $P_{max} = 483.4 Pa = 0.00493 \frac{kg}{cm^2}$
- Gear weight: $W_{Gear} = 0.169 kg$
- Box Controller and Solar PV panel weight: $W_{Box} = 5.21 kg$

- Stepper Motor weight: $W_{StepperM} = 0.60 \text{ kg}$
- Fresnel lens weight: $W_{Lens} = 0.3 \text{ cm} \cdot \pi \cdot \frac{(50 \text{ cm})^2}{4} \cdot 1.2 \frac{\text{g}}{\text{cm}^3} \cdot 0.001 \frac{\text{kg}}{\text{g}} = 0.707 \text{ kg}$

Using the values and relative distances, and applying forces and momentum concepts, it can be shown that the structure is in static equilibrium.

3.4.2 Worm Gear

The worm and gear wheel pair drive the mechanical movement of the solar tracker system, and they have very slow movement during the sun part of the day. The worm is connected through the worm shaft with a key in the shaft of the stepper motor.

Since the rotation of the upper frame of the structure should be very smooth and slowly to be accurate following the sun, the worm gear pair was designed with a gear ratio of 63:1. This means that, for each complete turn of the gear wheel, are needed 63 rotations of the worm. The design of the worm gear was made using Inventor® software. The design requirements for worm and gear on this project are listed in Table 3.2.

Table 3.2: Design parameters of the worm gear.

Parameter		Value
Common	Gear Ratio	63:1
	Tan. Module	4 mm
	Tan. Pressure Angle	20 °
	Helix Angle	9.0193 °
Worm	Number of Threads	1
	Worm Length	3.5 in
	Pitch Diameter	25.2 mm
	Diameter Factor	6.3
Worm gear	Number of Teeth	63
	Facewidth	19 mm

Parameter		Value
	Unit Correction	0
Loads	Efficiency	0.754
Driving Part - Worm	Power	0.1 kW
	Speed	1000 rpm
	Torque	0.955 N m
Driving Part – Worm gear	Power	0.075 kW
	Speed	15.87 rpm
	Torque	45.386 N m

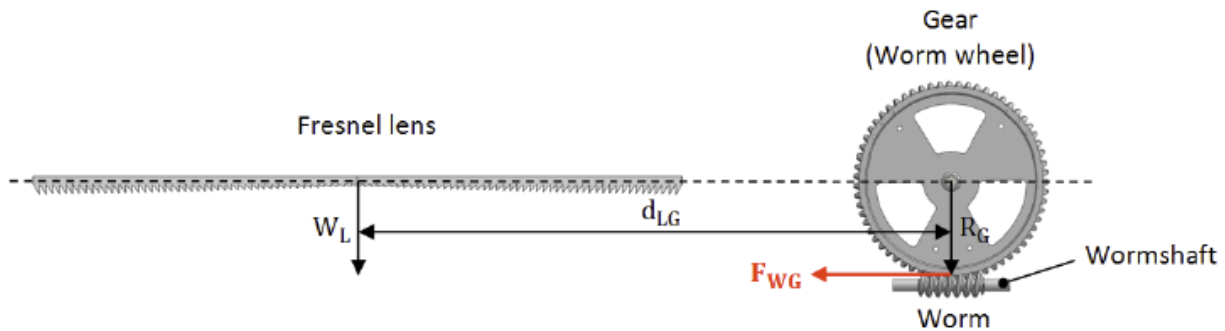


Figure 3.7: Schematic diagram of the worm-gear pair force.

Based on Figure 3.7 and considering the momentum equilibrium and the relation of forces between two gears, the worm gear force is given by:

$$F_{WG} = (W_L + W_{lens_frame}) \cdot \frac{d_{LG}}{R_G} \cdot \frac{\text{Number of worm teeth}}{\text{Number of the gear teeth}} = (W_L + W_{lens_frame}) \cdot \frac{d_{LG}}{R_G} \cdot m_G$$

$$F_{WG} = \left(0.706 \text{ kg} \cdot 9.81 \frac{\text{m}}{\text{s}^2} + 1.996 \text{ kg} \cdot 9.81 \frac{\text{m}}{\text{s}^2} \right) \cdot \frac{0.5 \text{ m}}{0.1316 \text{ m}} \cdot \frac{1}{63}$$

$$F_{WG} = 1628 \text{ N} = 0.366 \text{ lbf}$$

$$\text{Torque} = R_G F_{WG}$$

$$\text{Torque} = 0.1316 \text{ m} \cdot 1628 \text{ N} = 0.2143 \text{ N} \cdot \text{m} = 0.158 \text{ lbf} \cdot \text{ft}$$

where W_L is the weight of the Fresnel lens, W_{lens_frame} is the weight of the upper lens PVC

frame [kg], d_{LG} is the distance between the center of the Fresnel lens and the center of the gear, R_G is the radius of the gear, m_G is the gear ratio, and F_{WG} is the worm gear force.

Therefore, the torque has a value of $0.2143 \text{ N} \cdot \text{m}$ ($0.158 \text{ lbf} \cdot \text{ft}$).

3.4.3 LDR Sensors Analysis

LDRs are also called light dependent resistor or photo-resistor.

In this project, the solar intensity is translated to electrical values using a light dependent resistor (LDR). These are devices that change their electrical resistance according to the light that they receive.

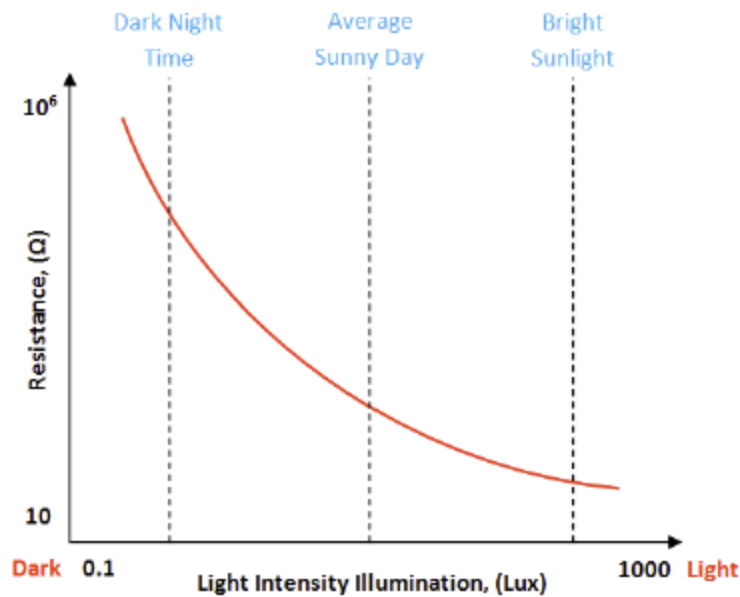


Figure 3.8: Variation of efficiency of LDR with solar radiation.

There are several models, mainly differing in the sensitive material: Cadmium Sulfide (CdS), Lead Sulfur (PbS) or Selenium (PbSe). The sensitivity depends on the incident wavelength, though, for this application, it can be considered constant in the visible light spectrum.

These devices present latency, which is the time elapsed between a light change and a resistance change. It can be 0.1 second from light to darkness, to 1 second from dark to light. As

these values are much less than the sun light variation during the day, the devices are acceptable for this application.

The value of the electrical resistance as a function of incident light was measured with a lux meter and a multi-meter. The results are plotted in the following graphic, presenting very similar shape to Figure 3.8:

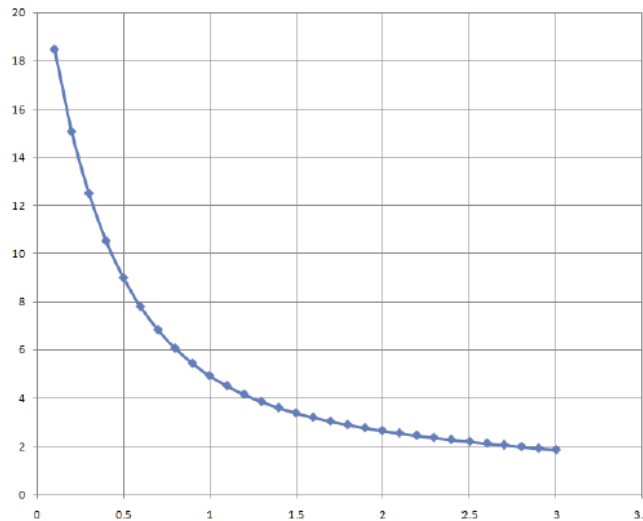


Figure 3.9: Resistance [kOhms] vs. Light [Lux].

Note that the resistance scale, vertical, is logarithmic. This electrical resistance can be approximated by a decreasing function.

The plot can be analyzed in three main areas: the initial part, for low luminosity, the resistance values are high, and seem to have small variation with light intensity. The final part, for high light intensity, tends also to have small variations after some light intensity. Both these areas would be inconvenient to use as a sensor, because they present low variation and saturation.

The central resistance zone, between about 12 kOhms and 2 kOhms is the part of the curve that this project will use. To be able to sense values in direct sun light it is necessary to

lower the LDR response, which is accomplished putting a translucent filter in front of the sensor.

3.4.3.1 Light Measurement

As there are large variations in electrical resistance, this project uses a differential approach. Two sensors are set to point in the sun direction, with slightly different conditions. The electric circuit uses a voltage divider that depends on the received light by each of the sensors, and the logic reacts to the difference between them to drive the mechanical parts.

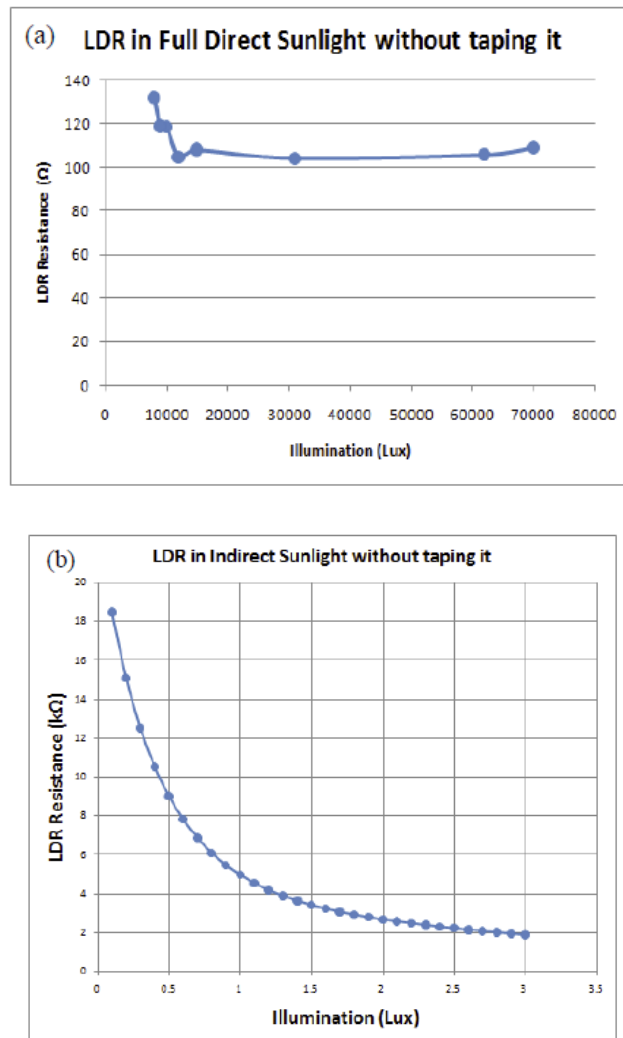


Figure 3.10: Measurement of LDR resistance as a function of illumination: (a) Full direct sunlight without taping the LDR, (b) Indirect sunlight without taping the LDR.

On Figure 3.10 (a), the resistance of the LDR sensor stabilizes in direct sunlight to small values of around 100 Ohms, meaning that the system lacks sensitivity, and the stepper motor only goes in one direction. On (b), the LDR has a working zone that presents variations at lower light intensities. Therefore, for this project is needed to operate in a specific range/zone of the curve to obtain the desired results.

The low resistance of the sensor in full direct sunlight puts the measuring electronic systems in the limits, and the small variations originated by sun changing positions are mixed with measurement fluctuations.

One way to move the operating zone of the sensor to a more usable region is reducing its sensibility. This can be done taping or putting a filter on its surface.

To be exposed at full direct sunlight, it is needed to put a filter or to tape the surface of the sensors to get resistance values more compatible with the controller.

A first preliminary test of the LDR sensor was conducted. Conclusions were obtained from the analysis of the measurements of light intensity with sensors at different sunlight conditions. Two experimental test were performed: one considering the LDR without taping (as come from fabric), and another taping the sensor. For each Graphs

3.4.3.2 Study Case 1: LDR without Taping

Figure 3.11 show the set up of the test using a LDR without taping.

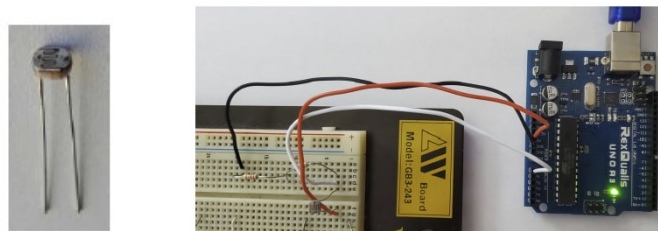


Figure 3.11: Sensor without taping used in the test.

3.4.3.3 Study Case 2: LDR with Taping

The test was performed using two taped LDRs with three layers of 3M blue scotch tape (see Figure 3.12 (a)) and one stepper motor, applying solar shadows with full direct sunlight.

The following picture shows the circuit set up of the taped LDR sensor experimental test. When one of the sensors is in the shadow, the other sensor is in light, and the stepper motor changes the rotational direction (from one direction to the opposite direction of the shaft occurs). When both sensors get the light same intensity, the motor stops; no rotation of the shaft occurs. The obtained results of the test were the desired and expected.

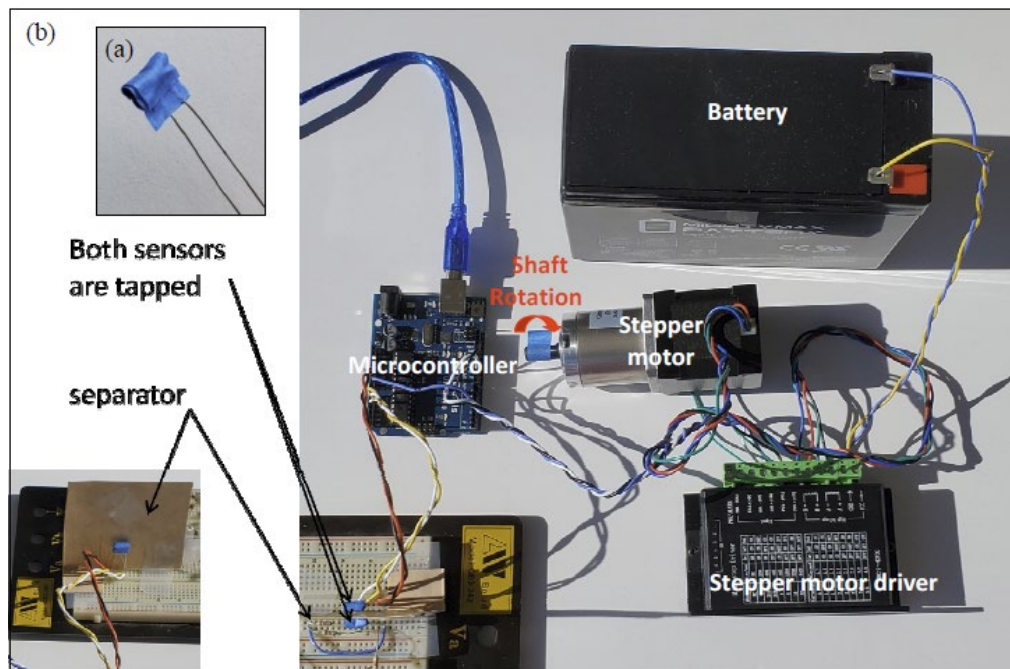


Figure 3.12: (a) LDR sensor taped. (b) Full direct sun experimental set up of the circuit with taped sensors.

3.4.4 Novel Sensor Holder

There are designs and prototypes that apply the concept of shadow to generate a difference of sunlight sensing. When the light falls in the shadow (dark) zone, the device can take an action.

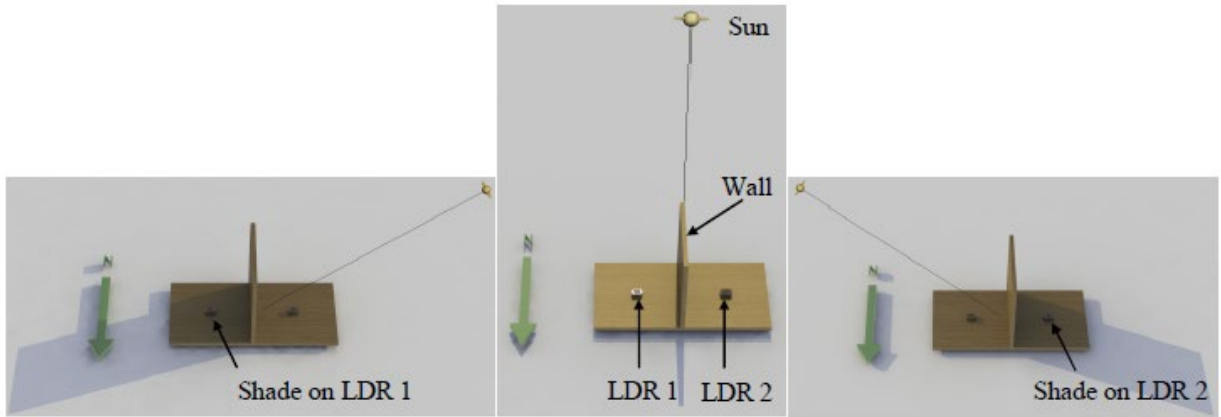


Figure 3.13: Shadow concept.

This concept can be extended and made more sensible, using two hollow tubes, and putting the sensors at the extremes of them.

Two sensor holders are located in opposite corner of the frame that contains the lens.

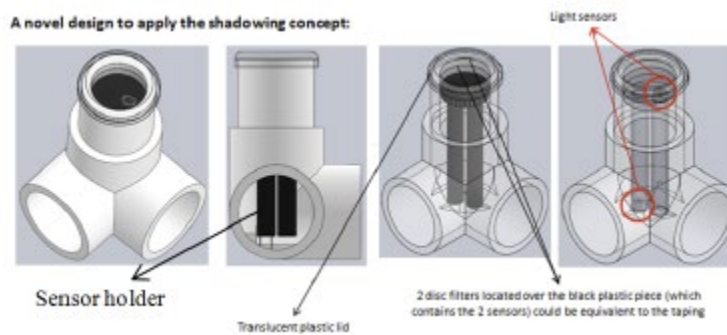


Figure 3.14: Sensor holder components.

The vertical difference between them is to sense the sunlight at different angles. This way, the Fresnel lens will be pointing with precision to the direct sun when both sensors receive the same intensity.

3.4.5 Stopper Motion Pad

The position of the left and right stopper motion pads on each side of the wheel is adjustable, depending of the inclination angle of the upper lens frame that be wanted, to limit

the gear movements to avoid damaging parts when the sun has low elevation or azimuth.

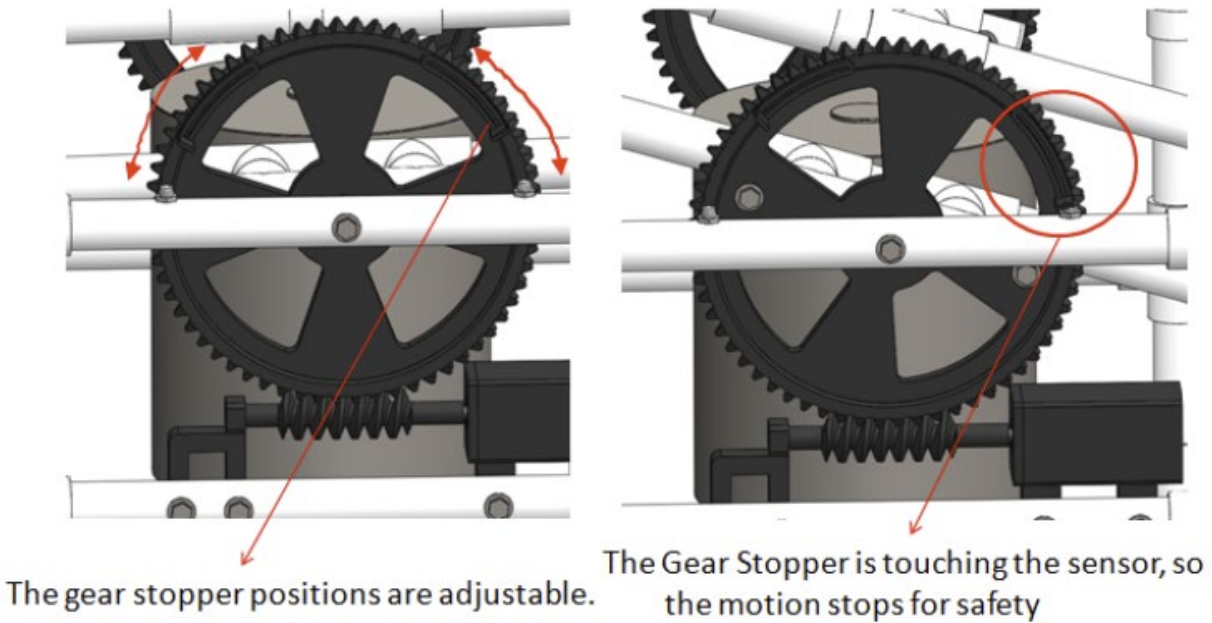


Figure 3.15: Stopper motion pad.

3.5 Simulations

In the following sections are presented simulation, analysis and results of the worm-gear assembly, wind speed velocity and pressure on the solar tracker system, representation of sun rotation from 40° to 140° inclination angle, and an overview of the entire project.

3.5.1 Worm-Gear Assembly

A Transient Structural analysis on worm gear and worm shaft support assembly was performed to evaluate the forces, using ANSYS® simulation. The gear selected for this simulation was the one which is attached to the “V” PVC structure that holds the frame lens in the upper part. This gear could be the most demanded in terms of forces.

Figures 3.17 to 3.19 show the conditions considered for the simulation, and Figure 3.20 illustrates the obtained results.

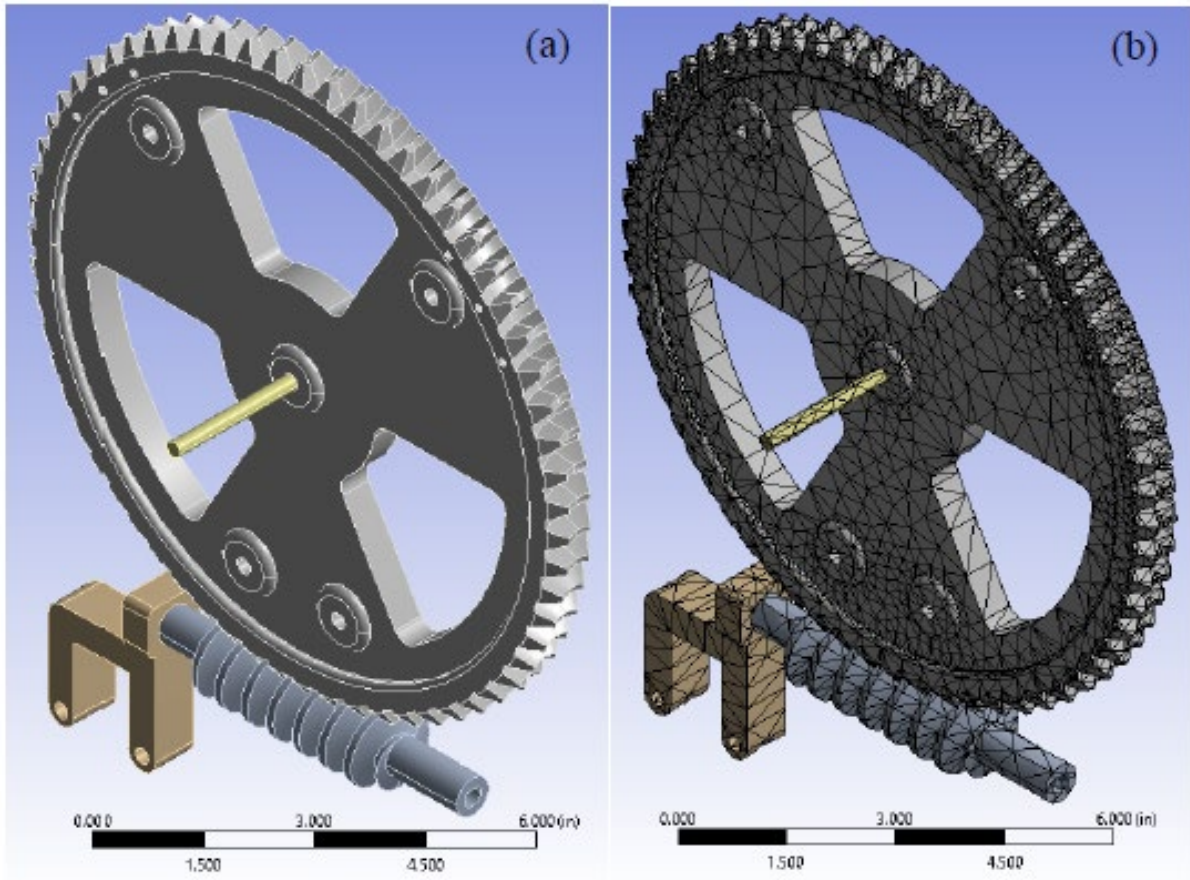


Figure 3.16: Worm gear simulation: (a) geometry of the model, and (b) mesh of the geometry model.

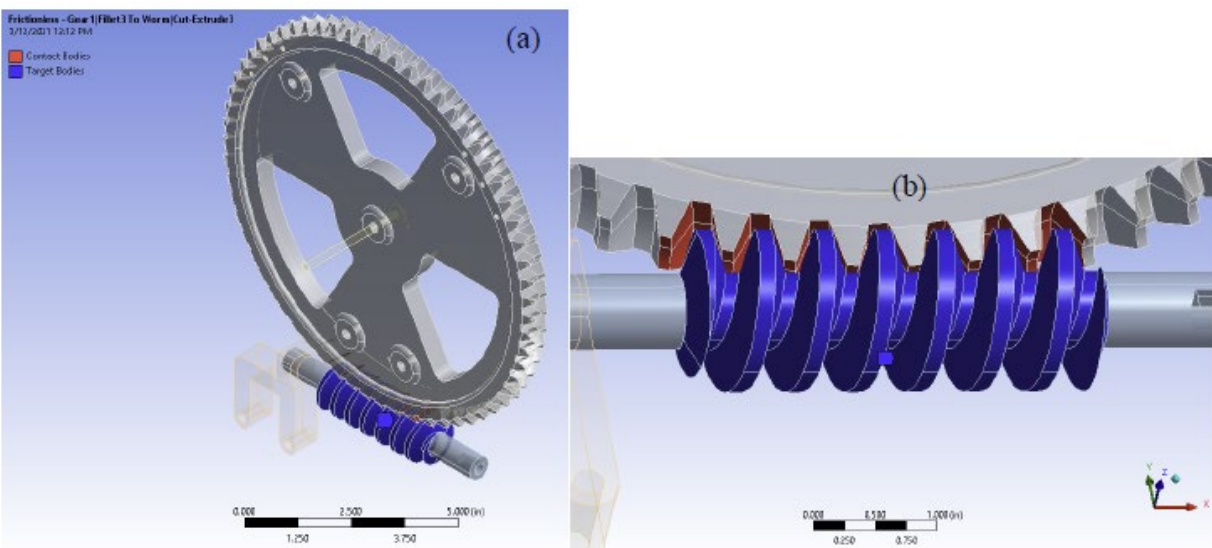


Figure 3.17: Worm gear simulation: (a) frictionless contact type between the worm and gear, and (b) worm gear teeth contact body view.

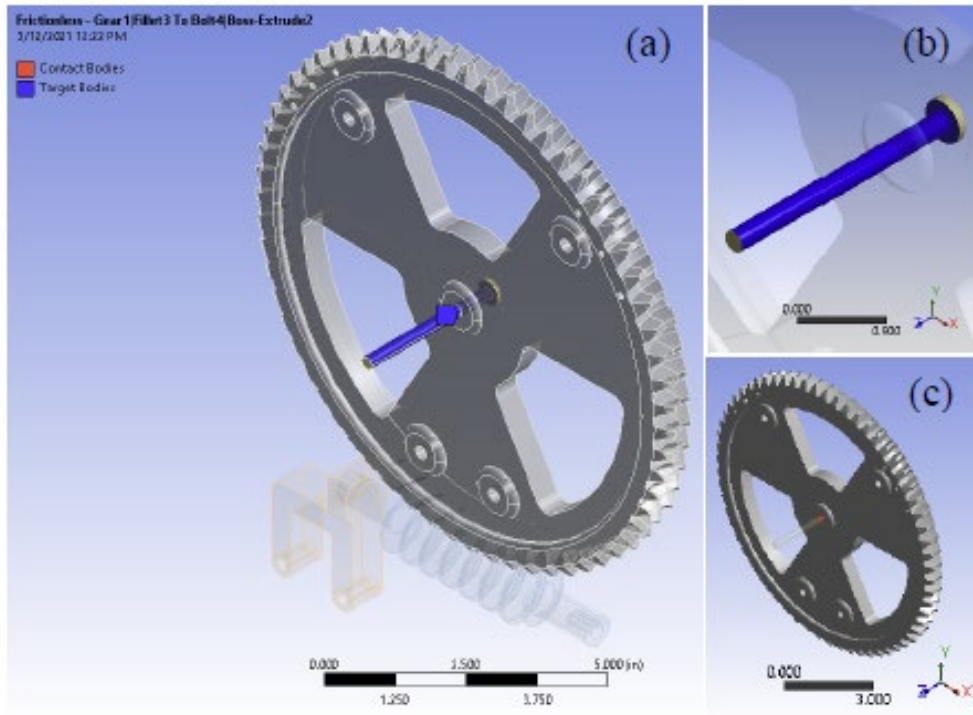


Figure 3.18: Worm gear simulation: (a) frictionless contact type between the bolt and the gear shaft hole, (b) bolt contact body view, and (c) gear shaft hole contact body view.

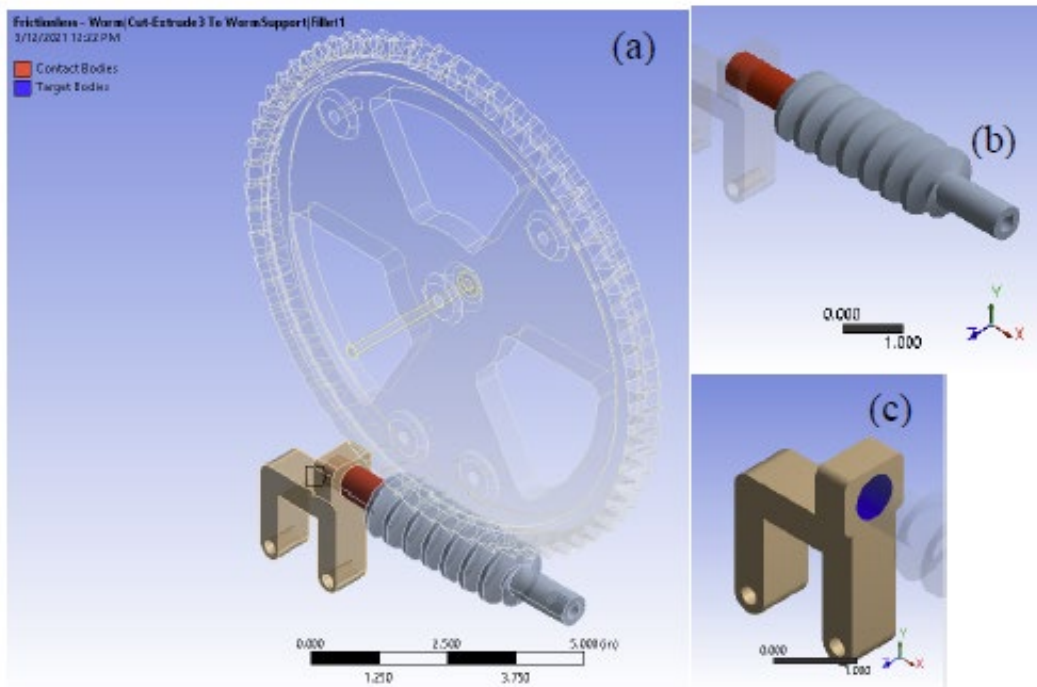


Figure 3.19: Worm gear simulation: (a) frictionless contact type between the shaft support and the worm shaft, (b) worm shaft contact body view, and (c) shaft support contact body view.

A moment of 0.158 lbf-in was applied to the worm shaft to generate the rotation. This torque value was calculated on Chapter 3. The simulation demonstrates results for equivalent stress, equivalent elastic strain and the total deformation in the model. The results obtained were: 0.0011163 inches maximum total deformation, 0.002433 maximum equivalent elastic strain, and 659.41 psi as maximum equivalent stress.

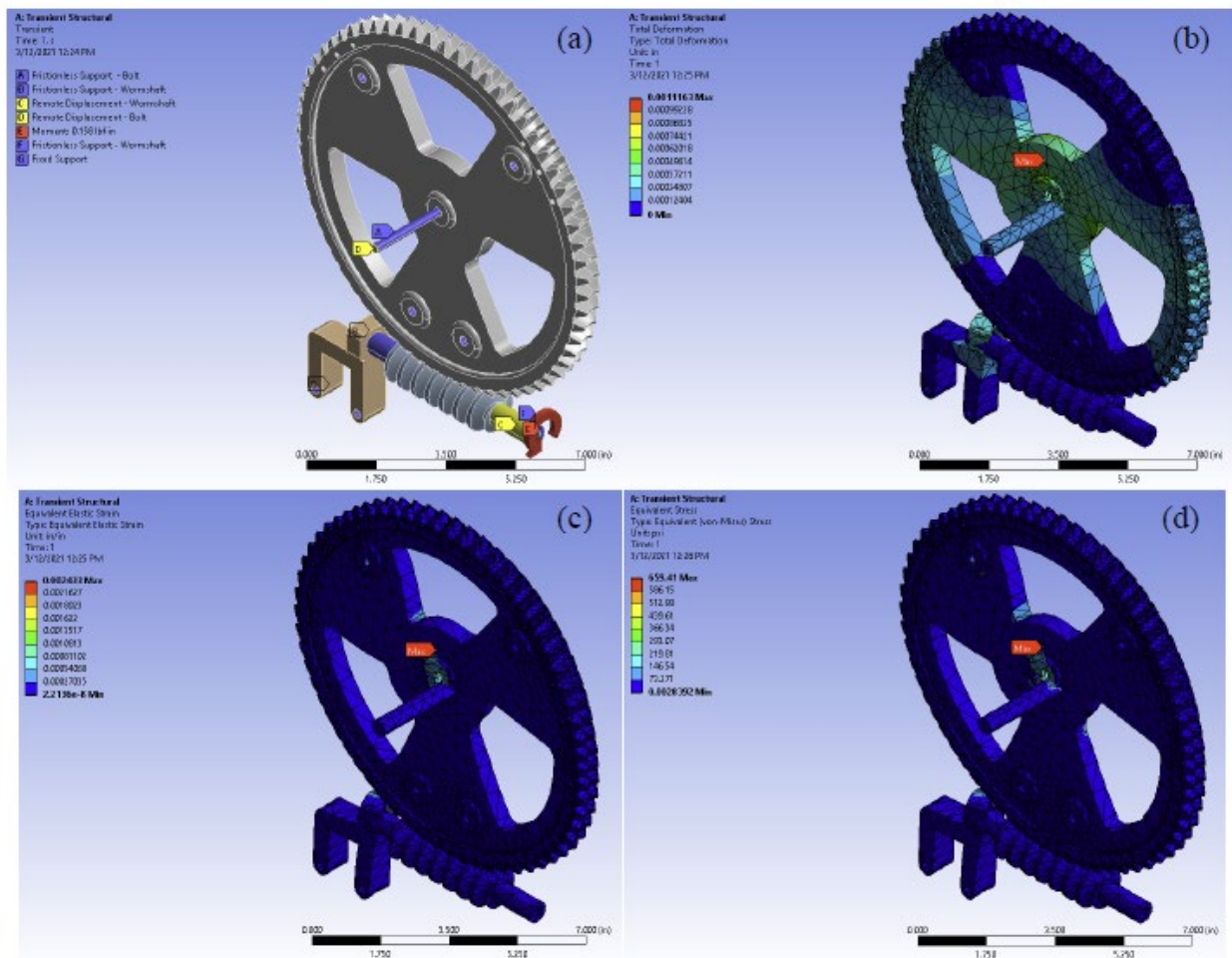


Figure 3.20: Worm gear simulation: (a) types of loads and supports applied on the model, (b) total deformation result, (c) equivalent elastic strain result, and (d) equivalent stress result.

3.5.2 Wind Speed Velocity and Pressure Simulation of the Dual-Axis Solar Tracker System

A wind simulation of the solar tracker systems was done, exposed to the most unfavorable conditions of wind speed and position. The simulations considered turbulent flow.

Due to the solar tracker system has more than 400 parts; the model was simplified to be supported by the software. An adverse inclination angle of the lens frame and Fresnel lens was considered (40° from ground level), similarly with the conditions of the wind simulation applied on the Fresnel lens surface in the section 2.4.3., being the Fresnel lens the part that could encompass most of the area facing the wind and creating more force.

Figure 3.21 shows the wind velocity distribution on the solar tracker system surface considering 20 mph wind speed. In this case, the position of the frame lens, which includes the Fresnel lens, is at 90° . The highest values of velocity profile are located in the upper part of the system, the frame lens.

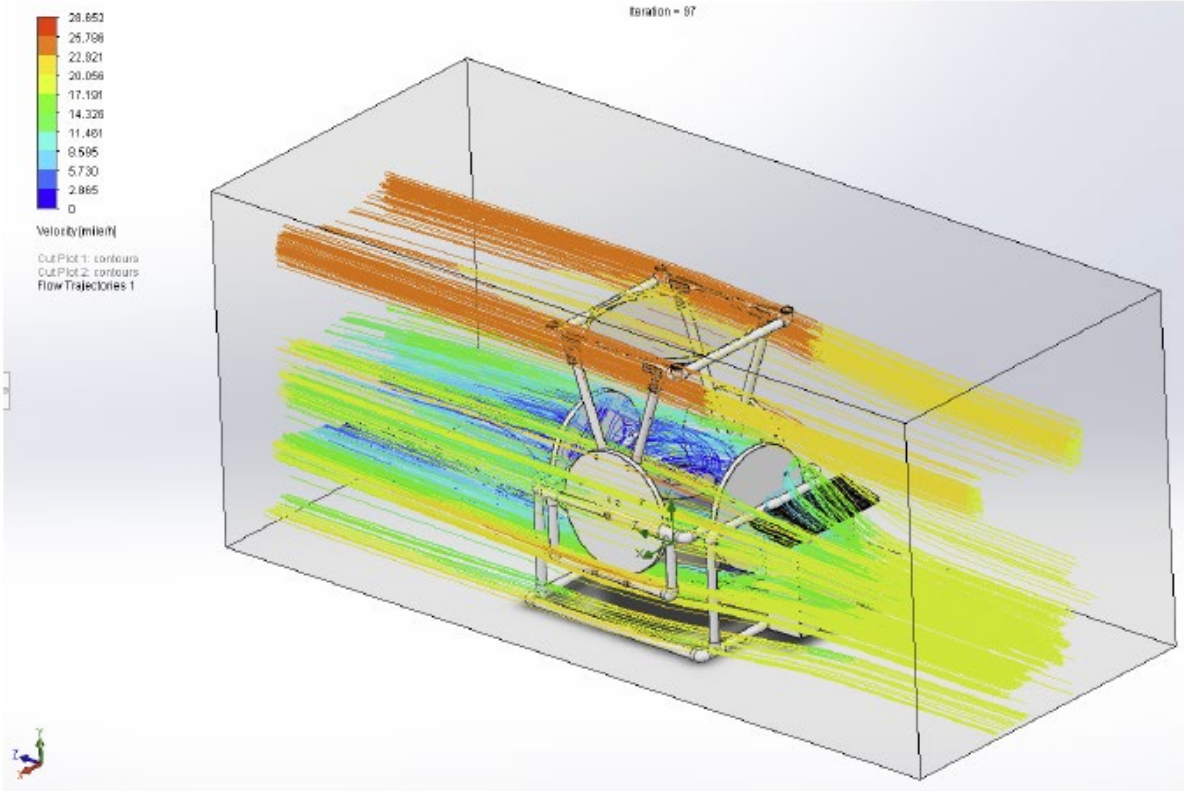
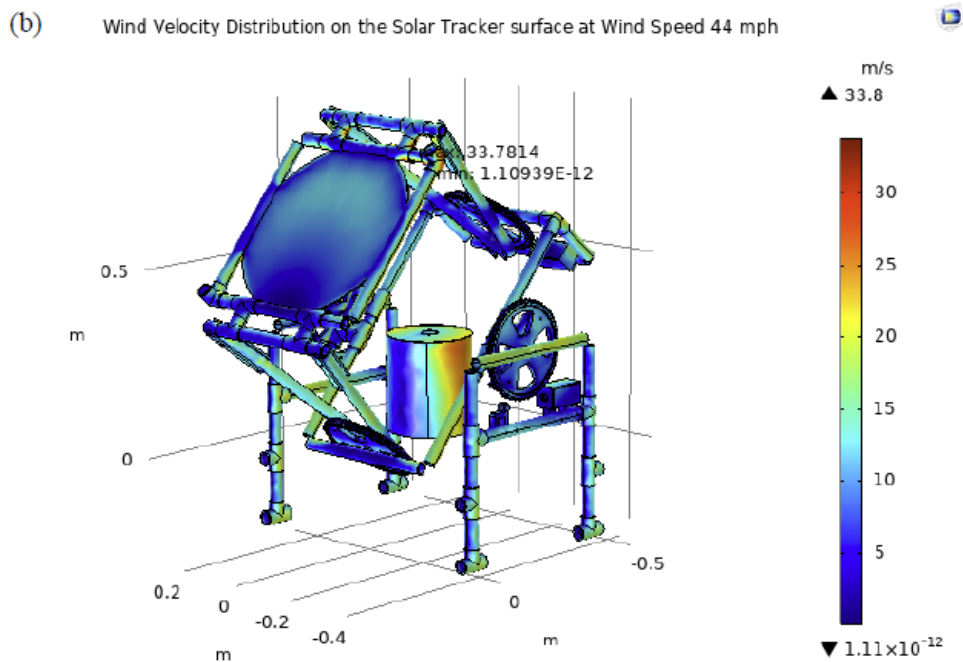
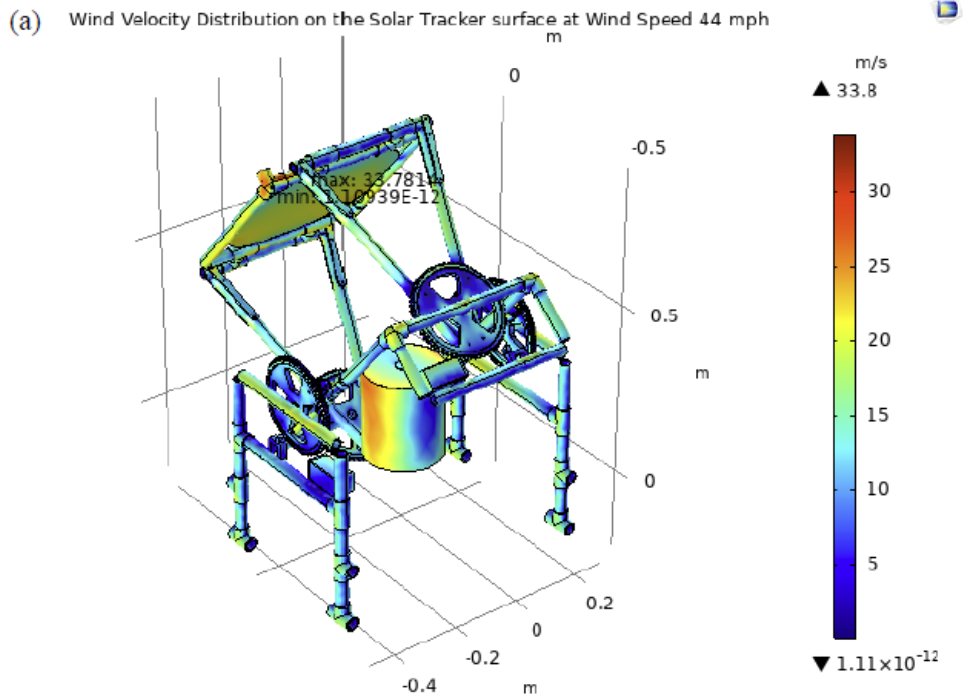


Figure 3.21: Wind velocity distribution on the solar tracker system surface at 20 mph wind speed.

Figure 3.22 and 3.23 show the results of simulating the simplified solar tracker model, using other software, at 44 and 65 miles per hour, respectively. In this case, it was considered an adverse inclination angle of the frame lens to see now the locations of maximum value of velocities and pressures.



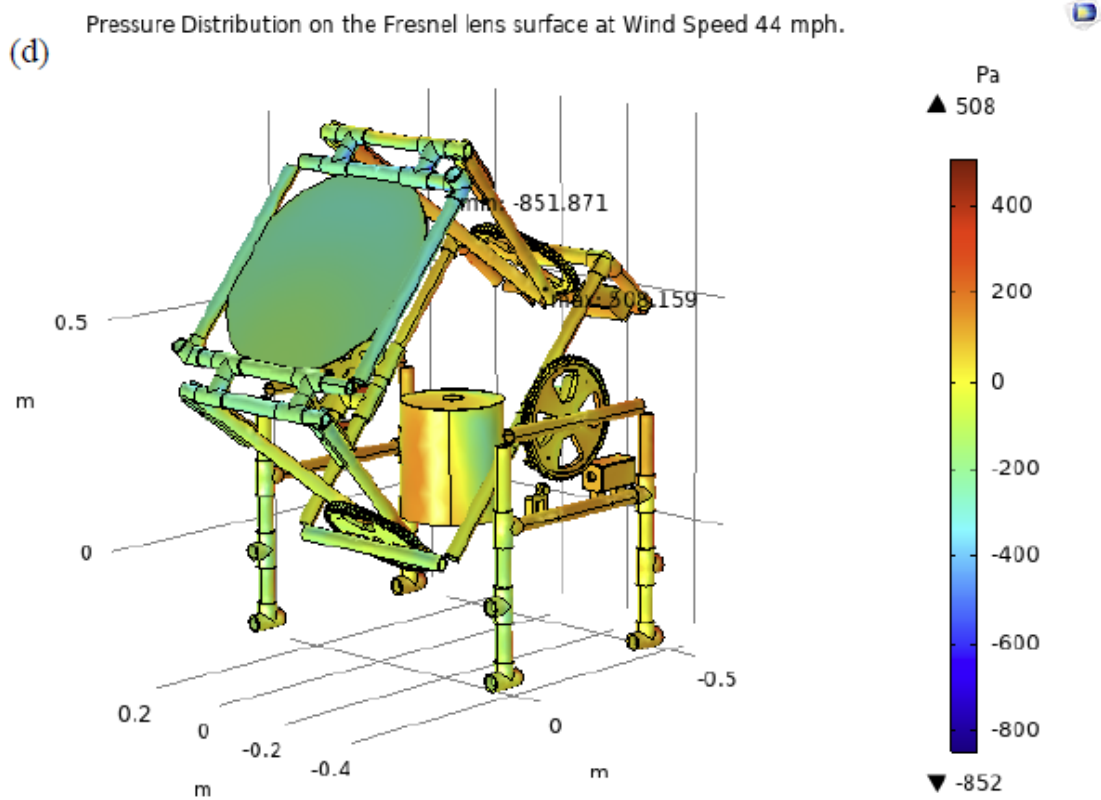
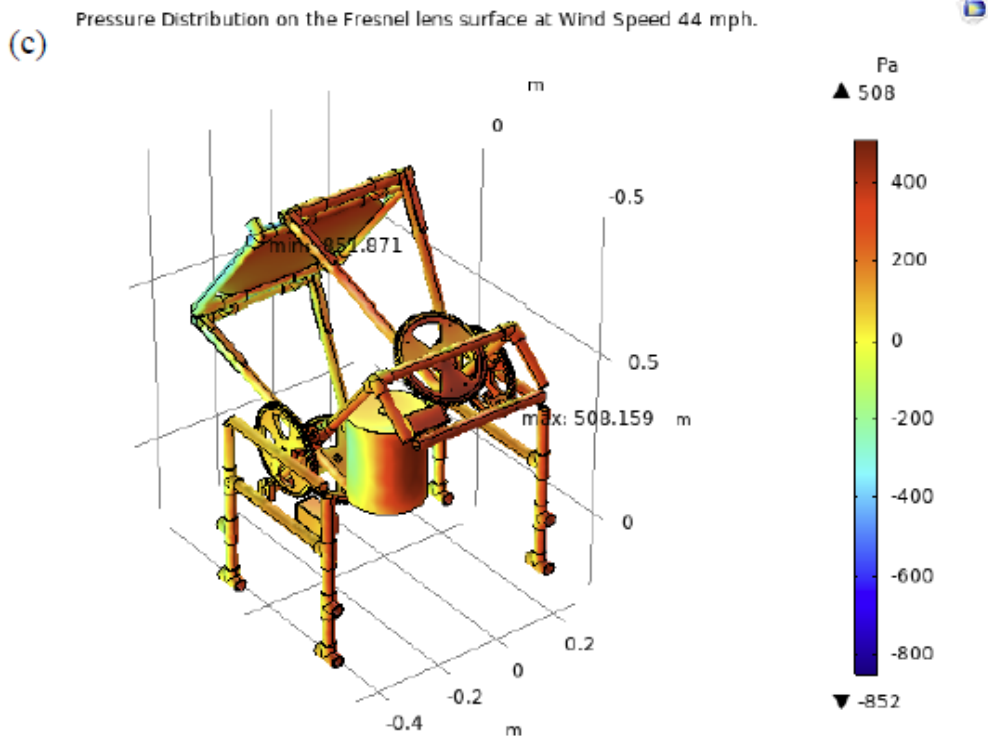
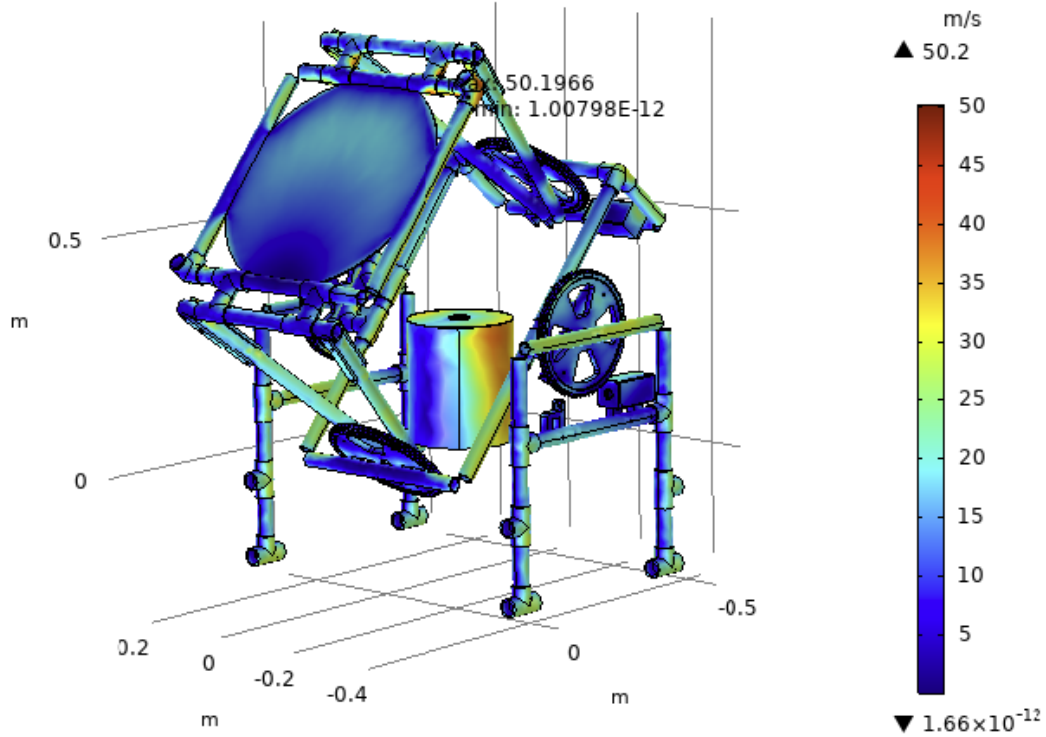
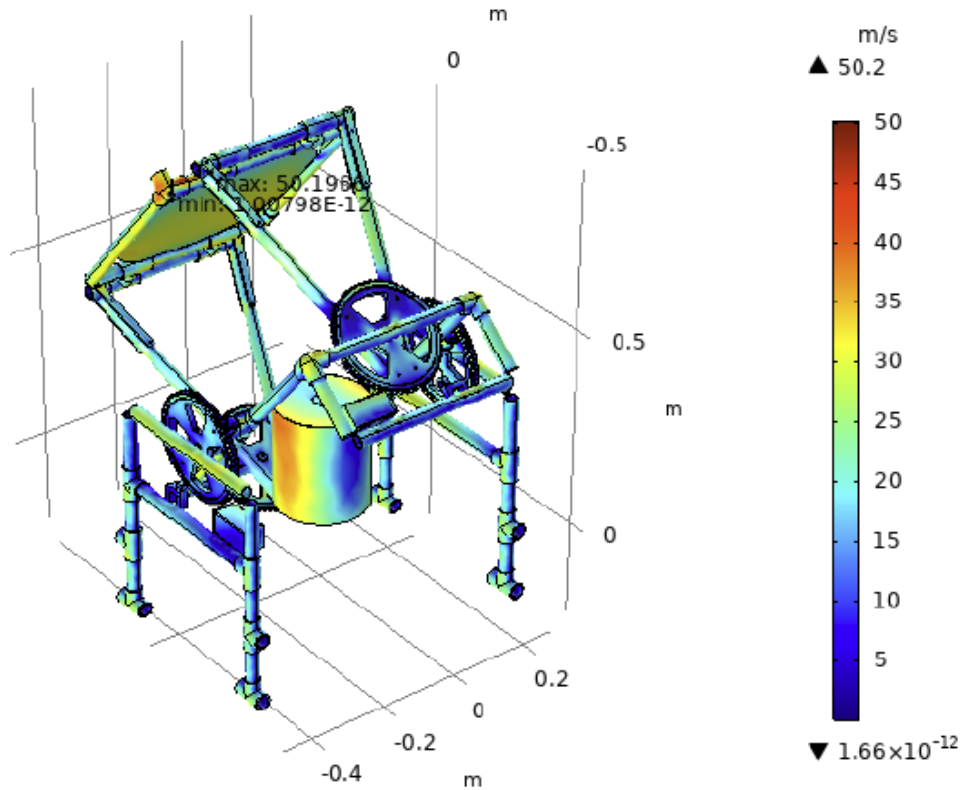


Figure 3.22: Wind simulation applying 44 mph wind speed on the solar tracker system surface: (a) and (b) distribution, location, and maximum/minimum values of wind velocity, and (c) and (d) distribution, location, and maximum/minimum values of pressure.

(a) Wind Velocity Distribution on the Solar Tracker surface at Wind Speed 65 mph



(b) Wind Velocity Distribution on the Solar Tracker surface at Wind Speed 65 mph



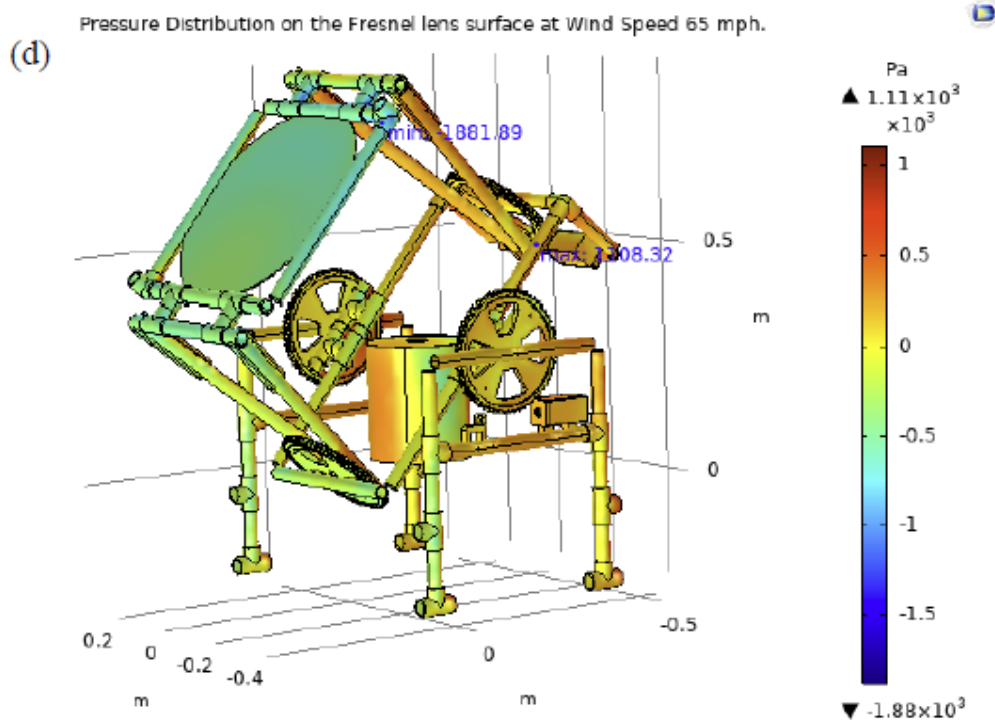
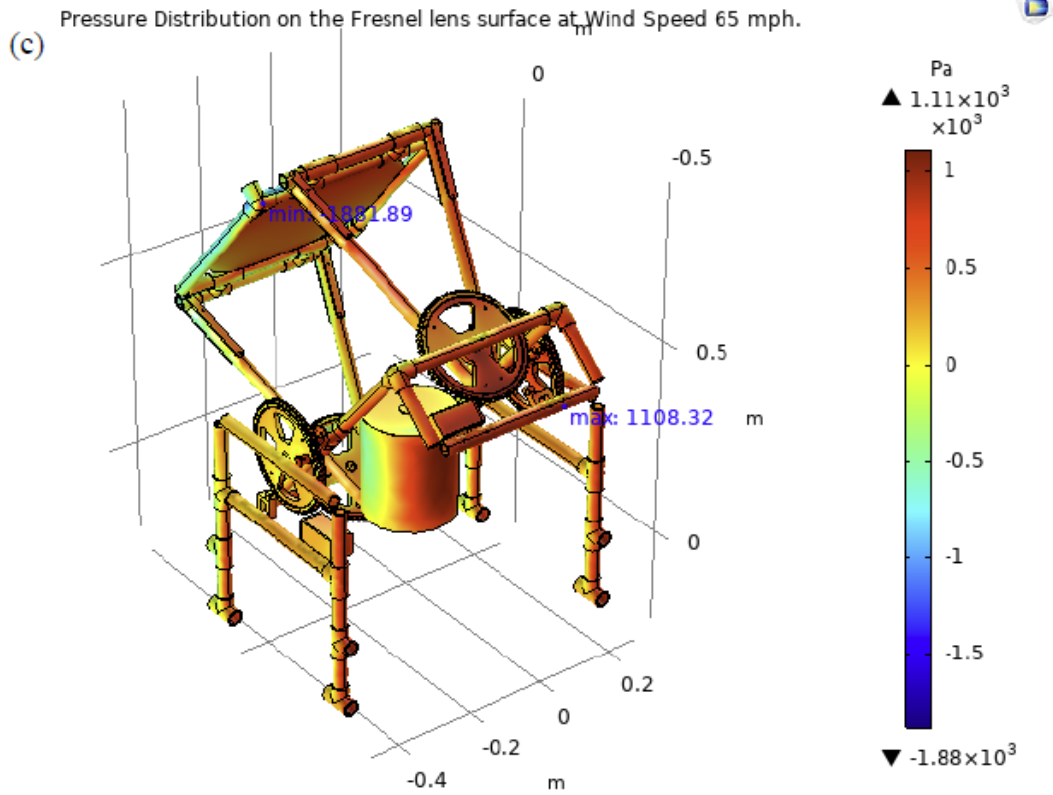


Figure 3.23: Wind simulation applying 65 mph wind speed on the solar tracker system surface: (a) and (b) distribution, location, and maximum/minimum values of wind velocity, and (c) and (d) distribution, location, and maximum/minimum values of pressure.

At 44 mph wind speed, the maximum speed velocity was 33.8 m/s (15.11 mph) located at the upper front of the frame lens, the minimum value is almost zero and it is in the back upper side of the frame. Regarding to pressure, the maximum achieved was 508 Pa at the center front frame which holds the stopper motor and worm-gear.

Applying 65 mph wind speed, the maximum speed velocity obtained was 50.2 m/s (22.44 mph), and the maximum pressure achieved was 1.11×10^3 Pa. Both maximum wind velocity and pressure locations were the same as applying 44 mph wind speed.

3.5.3 Visualization and Results for 40° to 140° Inclination Angle Representation

A representation of the solar tracker system considering angles of rotation across the day was made to visualize the rotation tracking of the sun during the harvest day time, from sunrise to sunset. Simulation results for each inclination angle were made applying ray heating. As outcomes, maximum temperature and heat flux values, peaks and distributions, are presented. Next figure shows a visualization considering some rotation angles as example during the day. For each inclination angle, there is a representation of the solar tracker system showing the position of the frame lens (upper part of the solar tracker system), also the concentration and the focussed rays on the receiver surface.

To simulate the sunlight angle of rotation through the harvesting day time, a 1.5 inches receiver diameter, 0.5 inches receiver thickness, and 0.06252 inches hollow rod thickness was used for inclination angles from 40° to 140° over ground. The receiver, rod and fins are inside of an evaporator tank. An insulating foam ring was placed between the wall of the receiver and the evaporator tank.

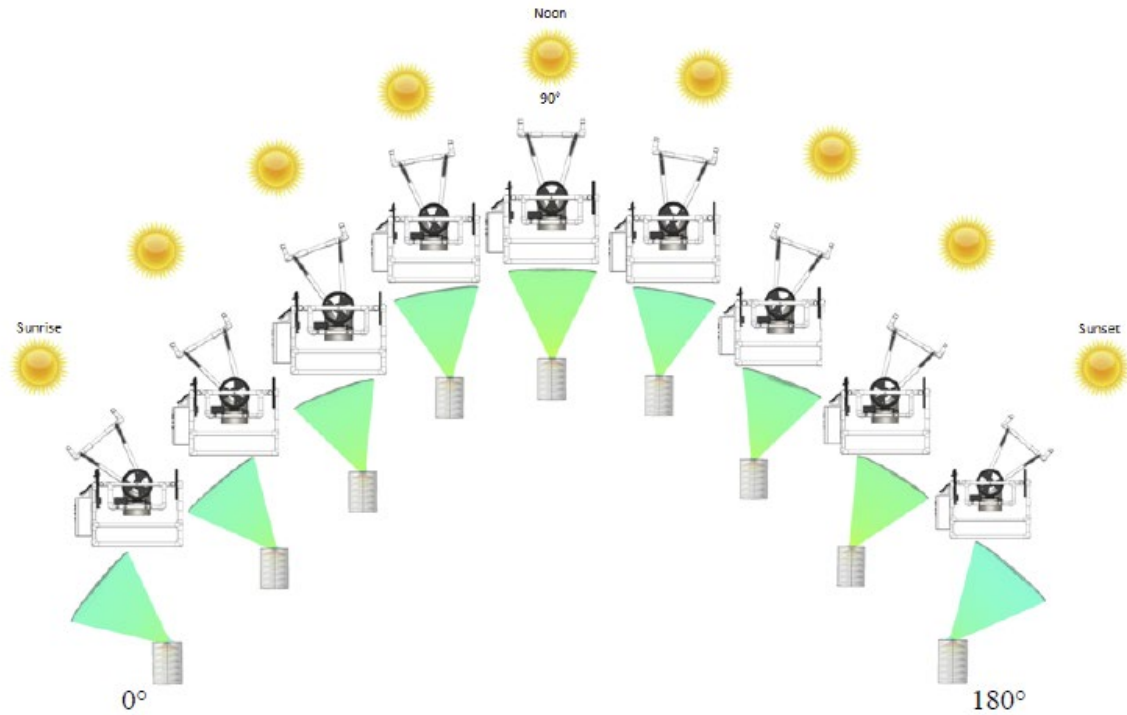


Figure 3.24: Representation of different inclination angles that takes the solar tracker system during the day, following the sun light.

Eleven simulations results, see Table 3.3, show that the temperature variation according the inclination angle from 40° to 90° the temperature increased and from 90° to 140° the temperature decreased, obtaining a peak maximum temperature of 840.96 [K] when the solar tracker with the Fresnel lens are located at 90° respect the horizontal plane (ground). Moreover, between 70° and 110° the values remain similar being reasonable. The temperature curve presents a symmetrical form respect to 90° inclination angle, and it follows the Gaussian function form of the Figure 2.8 (a) and (b). Figure 3.25 illustrates the described temperature behavior.

Results also show values of heat flux on the receiver surface. The maximum value, $1.68 \times 10^6 \text{ [W/m}^2\text{]}$, was archived at 90° respect the horizontal plane (ground), coinciding with the angle of maximum temperature. The heat flux curve also presents symmetry with respect to

the 90° inclination angle and a Gaussian function form in the center range of inclination angles.

See Figure 3.25.

Table 3.3: Maximum temperature and heat flux on the receiver surface due to ray heating, from 40° to 140° inclination angle respect ground of the dual-axis solar tracker.

Receiver Diameter [inches]	Receiver Thickness [inches]	Rod Thickness [inches]	Inclination Angle [°]	Max. Temperature [K]	Receiver Surface Heat Flux [W/m ²]
1.5	0.5	0.06252	40	766.35	1.30E+06
			50	801.11	1.41E+06
			60	823.20	1.16E+06
			70	838.01	1.45E+06
			80	839.14	1.59E+06
			90	840.96	1.68E+06
			100	839.88	1.60E+06
			110	839.45	1.60E+06
			120	824.03	1.08E+06
			130	802.36	1.44E+06
			140	767.26	1.22E+06

Figure 3.25: Values of maximum temperature and heat flux on the receiver surface due to ray heating, from 40° to 140° inclination angle respect ground of the dual-axis solar tracker.

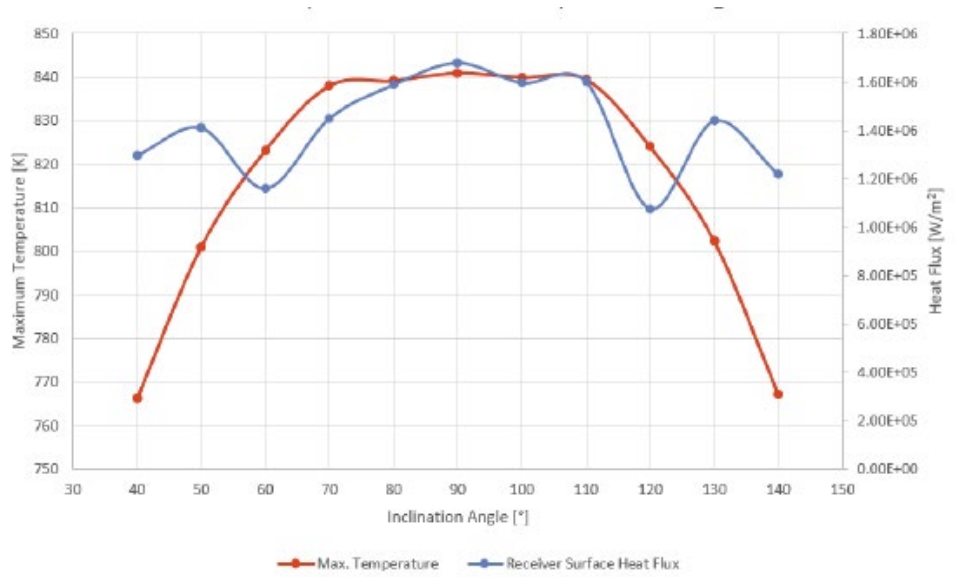
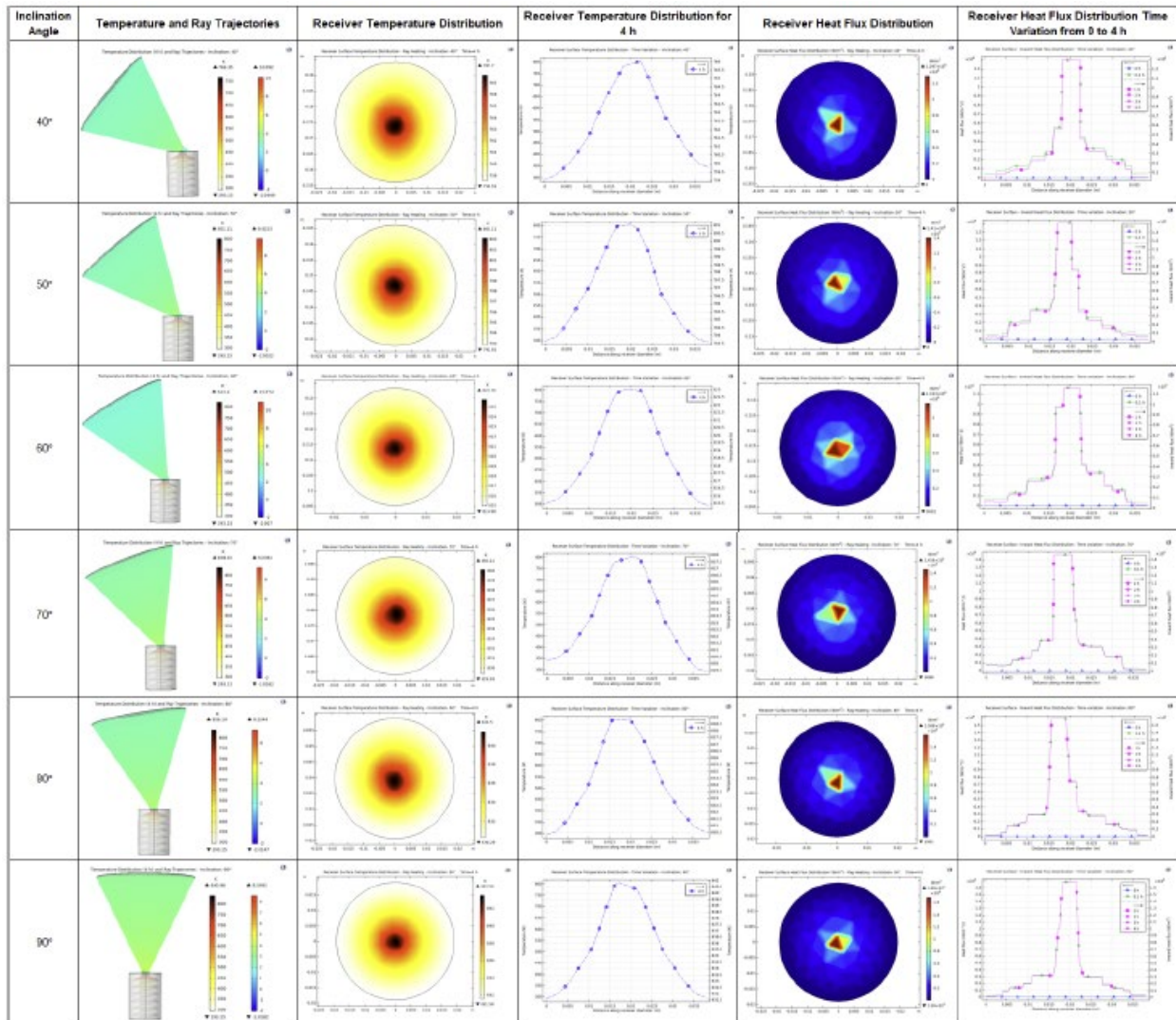


Figure 3.26 presents a visual summary by variation angle, from 40° to 140°, of the dual-axis solar tracker showing values of maximum temperature and heat flux applying Ray Heating COMSOL Multiphysics® simulation. Second and third columns illustrate a SOLIDWORKS® and COMSOL Multiphysics® position of the solar tracker depending on the inclination angle. Fourth

and sixth columns show the variation of maximum temperature and heat flux on the receiver surface, respectively. On both cases the maximum values are located in the center of the receiver, meaning that the concentration of rays created by and coming from the Fresnel lens are focusing correctly in the center of the receiver (focal point). Fifth and last column show temperature distribution along the receiver surface for 4 hours simulation, and heat flux distribution along the receiver surface, from 0 to 4 hours respectively, using COMSOL Multiphysics®. From the fifth and last column we can observe that the heat and heat flux, along the receiver surface, have a Gaussian function form.



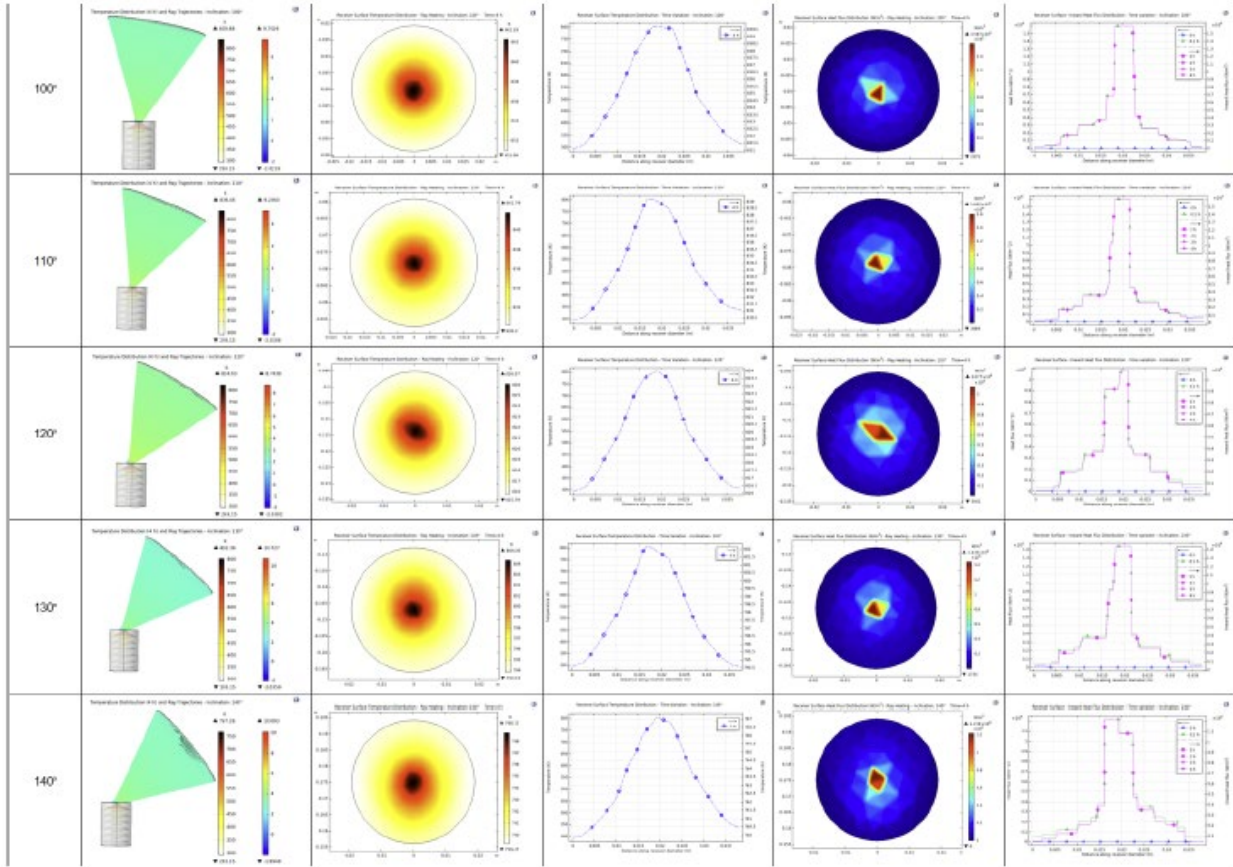


Figure 3.26: Visual inclination angle variation, from 40° to 140° , of the dual-axis solar tracker with values of maximum temperature and heat flux on the receiver surface due to ray heating.

CHAPTER 4

FABRICATION

4.1 Fabrication

The fabrication includes two main parts: hardware and software. The hardware conforms the PVC pipes structure, joints with washers, nuts, bolts, brackets, the flat Fresnel lens and parts that are part of the mobile structure, etcetera. On the other hand, there are the electric, electronic, and the controller logic code.

Appendix E presents a chronological construction photo gallery. It shows the fabrication process, from the raw materials to the final solar tracker system construction.

4.2 Hardware

A research of companies that produce or sell Fresnel lenses was done. However, their design offers did not match in shape (diameter, thickness, etc.) with the present project design. Another option considered was to buy an acrylic with the dimensions needed and fabricate the lens in the University laboratory. Because the budget to fabricate the lens was \$4,245, other options were considered. Therefore, the flat Fresnel lens was bought in Amazon. It has a diameter and focal length of 500 mm and a thickness of 3mm. It is of acrylic PMMA (Polymethyl methacrylate) material, with a transmission of 92% (from 400-1100 nm). The groove pitch is 0.5mm. It can operate at temperature of 80 °C (maximum).

The resistors and capacitors for the electronics were selected to be normalized.

4.2.1 LDR (Photoresistor)

Figure 4.1 shows a LDR sensor used in the project.



Figure 4.1: LDR sensor.

4.2.2 Sensor Holder Assembly

The sensor holder, black part in the next picture, is located inside of the short PVC tube, at the extremes of the Fresnel lens. This tube is closed in the upper side by a cap that has a hole in the center, allowing the sun rays enter to LDRs. On the top of each of this caps is attached a transparent plastic piece, which allows the sun light to enter, but avoids the dust and rain. Two small blue plastic pieces are located and attached on the top LDR surface, making it less sensible to the intensity of the sun, to have a better response without saturation.



Figure 4.2: Sensor holder assembly and components.

4.2.3 Stepper Motor

The selected stepper motor has a small angle for each impulse, making the device more precise in its positioning and following the sun.

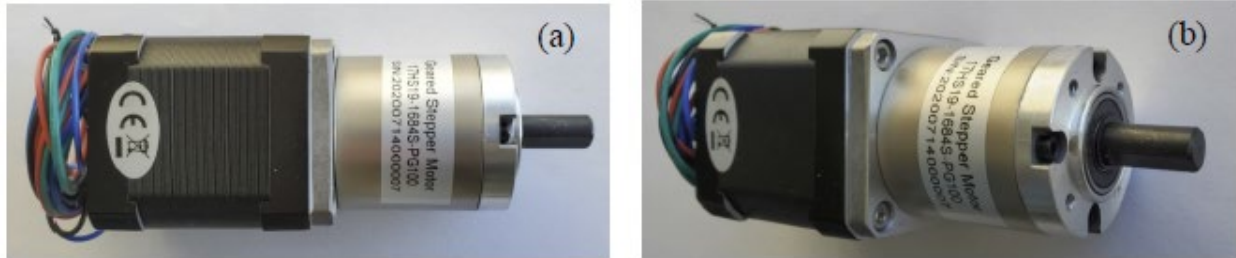


Figure 4.3: (a) Stepper motor, (b) Different point of view of (a).

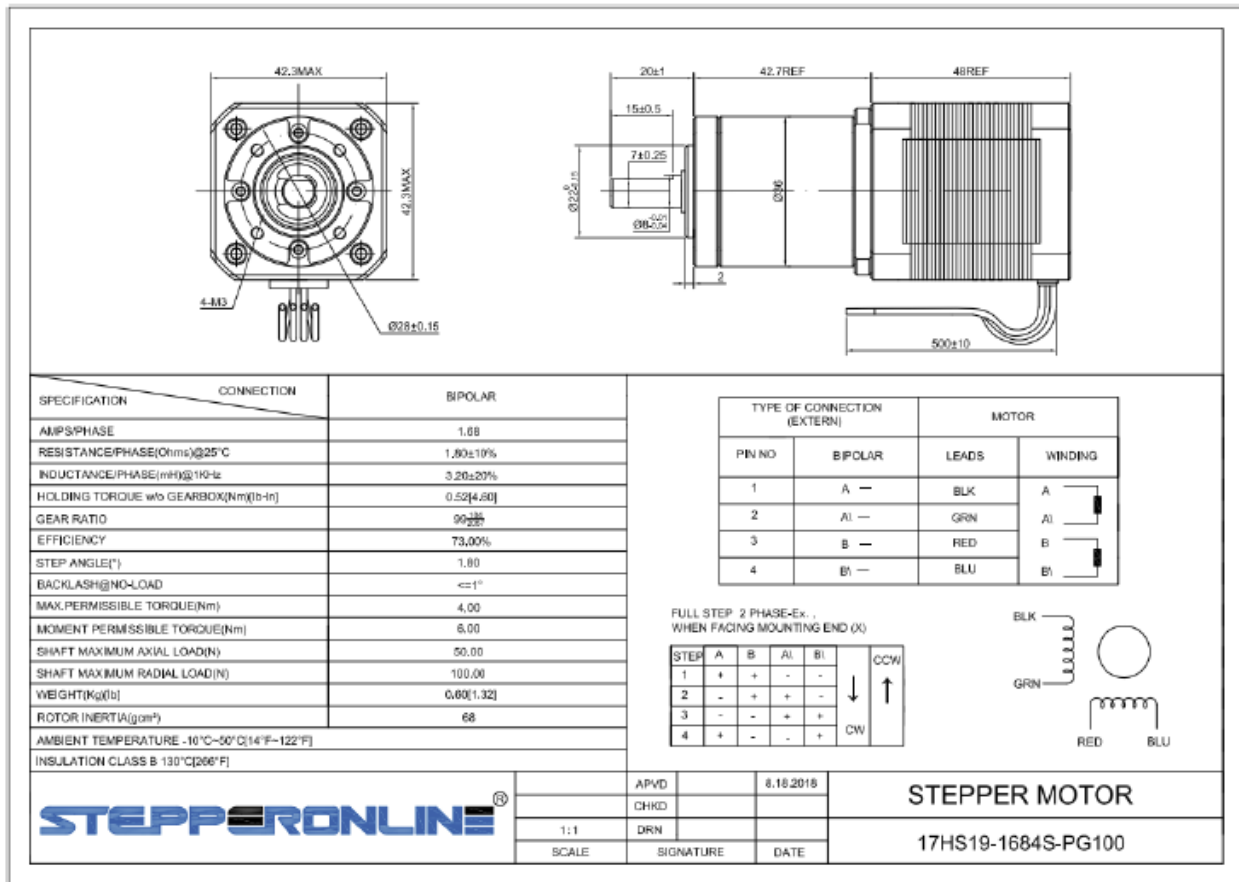


Figure 4.4: Technical characteristics of the selected stepper motor.

4.2.4 Security Limit Switches

As the system is based on light measurements, it can potentially generate movements that could go beyond what the mechanical parts are designed to do. This is why there are four bush button switches at the end of each allowed displacement that are being sensed by the controller. Once the allowed movement reaches its end or limit, the logic stops sending orders to move in this direction, but accept commands to move in the opposite way.

These security limits are enforced whether the movement is automatic, following the sun, or manual, originated by a user pushing the front buttons.

There are four stop motion buttons, two for each axis rotation frame. These buttons are labeled with a legend saying “Stop Motion.”

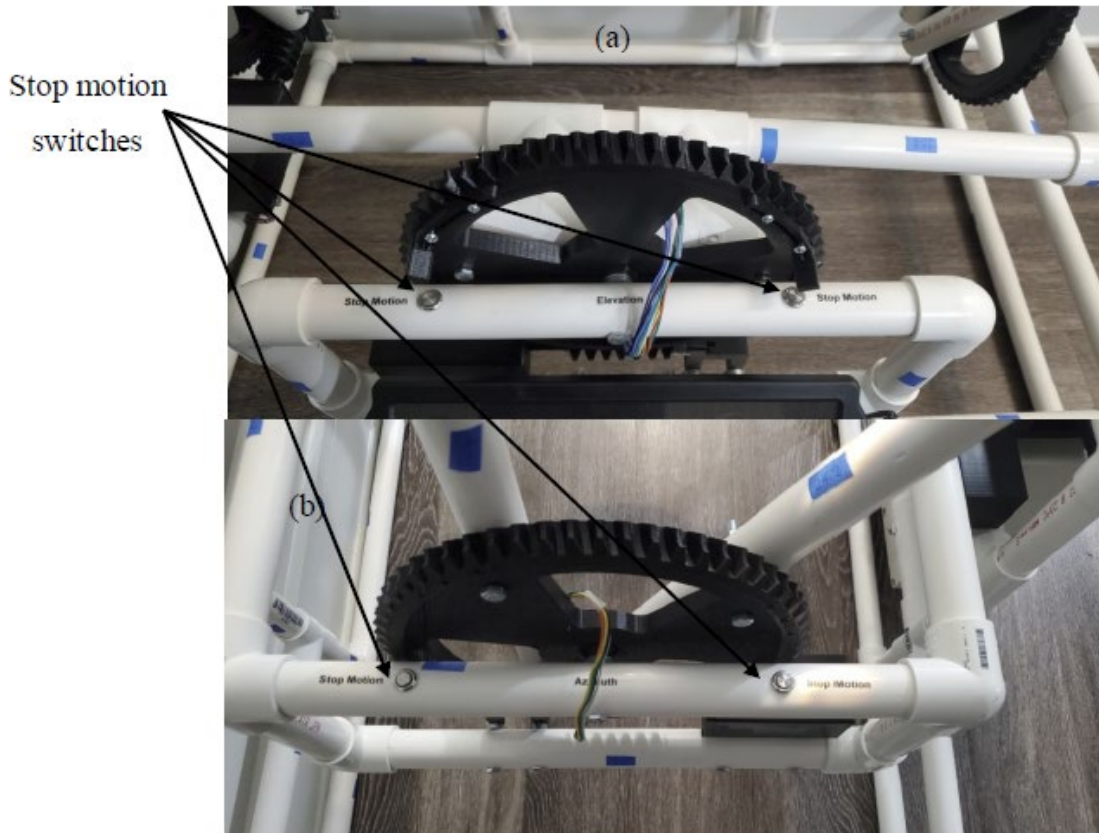


Figure 4.5: Security limits switches: (a)-(b) they located in two different frames, one for each axis rotation.

4.2.5 Manual Controls

The mechanical system has a speed reduction by a worm gear system, and the stepper motors have a speed reduction 100:1. This high reduction means that it is not possible to move the Fresnel lens by hand. This is why the controller has four buttons to override the presence of light measurements, and to manually generate the signals to move the motors. There are buttons to manually adjust the azimuth and elevation of the lens to any value.

In addition, indicating labels were added to the controller box cover to easily identify its functions. See Figure 4.6.

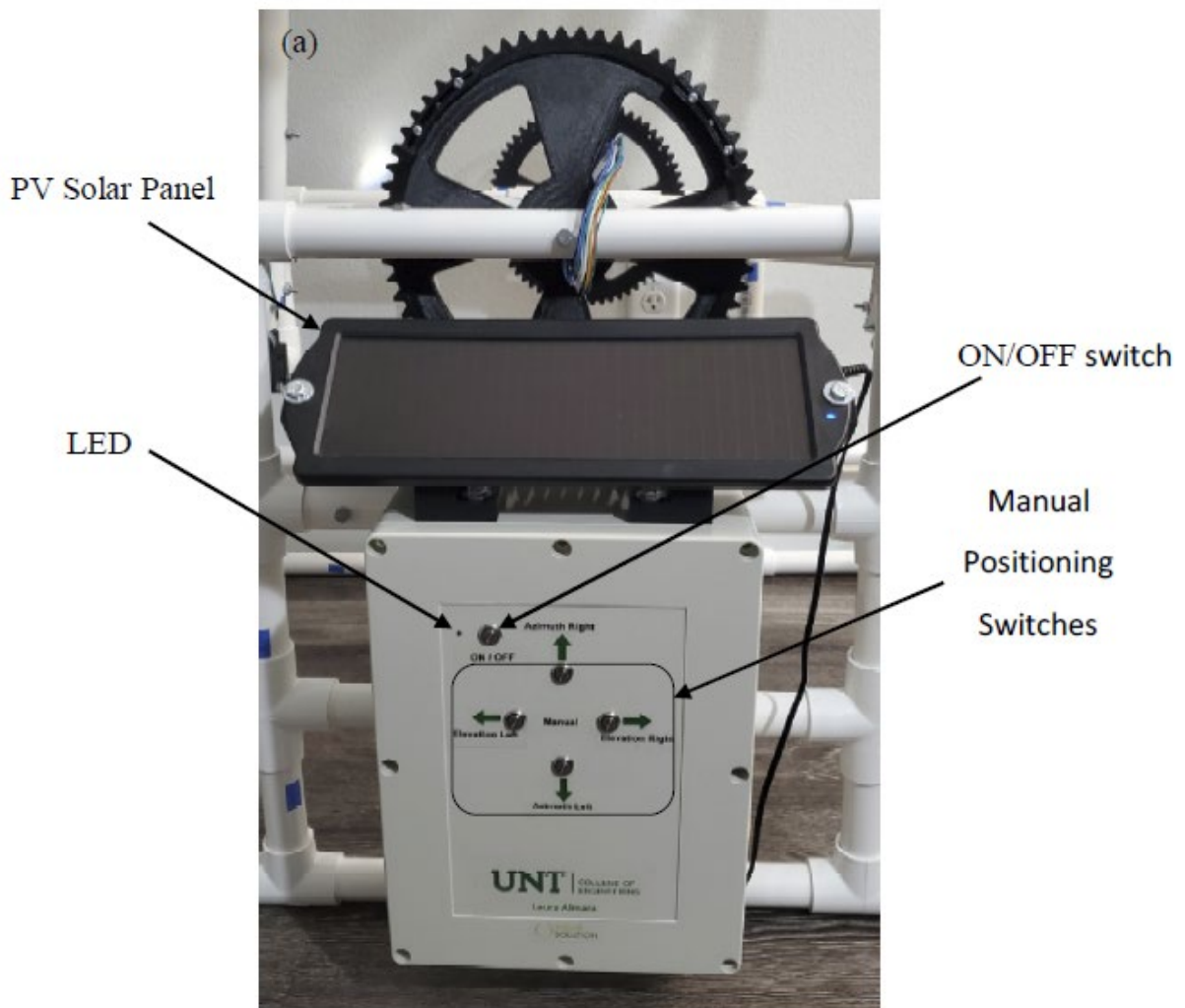


Figure 4.6: Controller box: outside.

4.2.6 Controller Box

The controller box cover includes a red LED light to indicate the ON/OFF state, an ON/OFF switch, and four manual positioning switches.

The electric safety of all the wires of the electric connections was increased using heat shrink tubes. This was also, appearance and better look of the overall project. Figure 4.7 illustrates the use of these plastic tubes.

Directly above of the controller box, is located the PV solar panel attached with two designed 3D printed brackets.

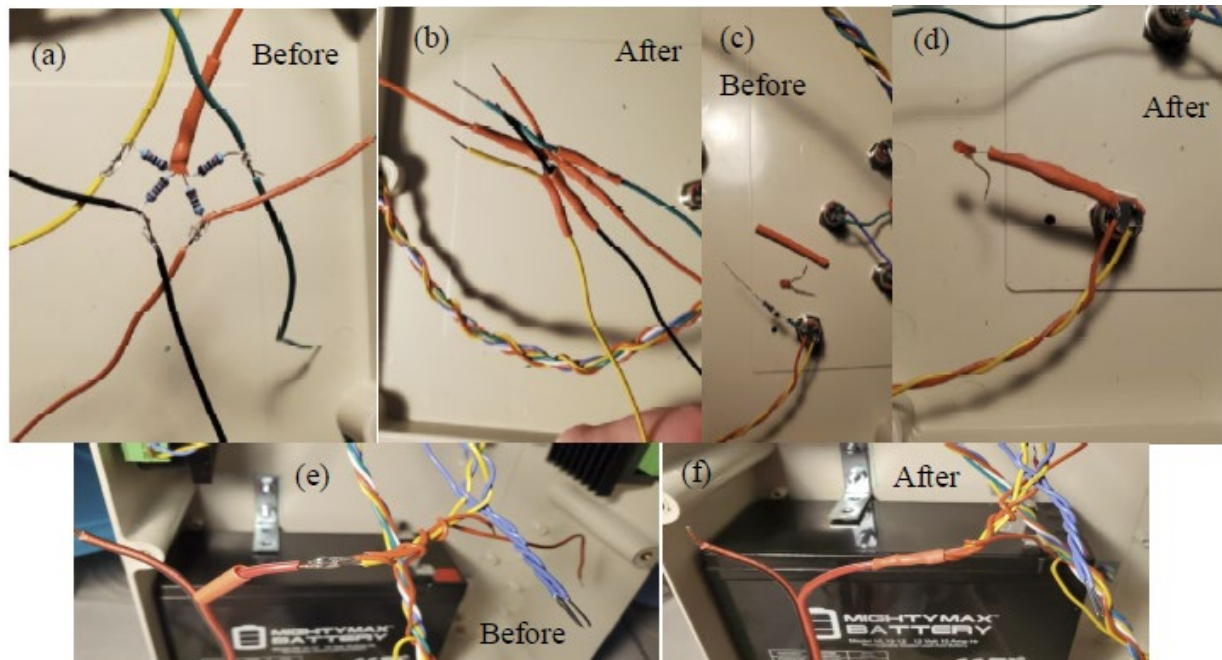


Figure 4.7: (a)-(f) Before and after of using heat shrink tubes in the connection wires.

4.2.7 3D Printed Parts

Because the dual-axis solar tracker automatic system is a novel design, some important parts of the structure were needed to be printed in 3D printed machines in the University

laboratories, such as the two types of gears, worms, sensors holders, shaft supports, and the right and left gear stoppers. All these parts were custom designed for this project.

The solar brackets and the box support of the stepper motors were designed to be fixed to the main structure. In addition, the stepper motor box also protects the stepper motors from corrosion (sea environment) and from rain, due that they work with electricity.

The objectives to print in 3D these parts were the corrosion resistance, weightless, and custom design for the novel solar tracker presented. The ABS material supply needed for all these pieces was 97.83 in³ and 35.92 in³ of support material. The 3D printed parts are the color black in the project.

There were used two types of 3D printed machines, one has very good finishing of the part, and for the other it was necessary to redo the holes because of extra material attached.

Table 4.1 lists the parts printed in 3D and theirs quantities.

Table 4.1: Name Part Description and Quantity of 3D Printed Parts.

Part	Qty
Gear 1	2
Gear 2	2
Worm	2
Sensor Holder	2
Bracket	8
Stepper Motor Support Cap	2
Stepper Motor Support Only	2
Shaft Support	2
Right Stopper Motion Pad	2
Left Stopper Motion Pad	2
Solar Bracket Right	1
Solar Bracket Left	1

The following images show the 3D printed parts finished.

There are four gear wheels in total in the solar tracker system, of two different types. See Figure 4.8. The three small holes near the outer border of the gear are to attach the stopper motion pads, one in the left and other in the right upper side. The gears were designed to have less material, being cheaper and lighter.

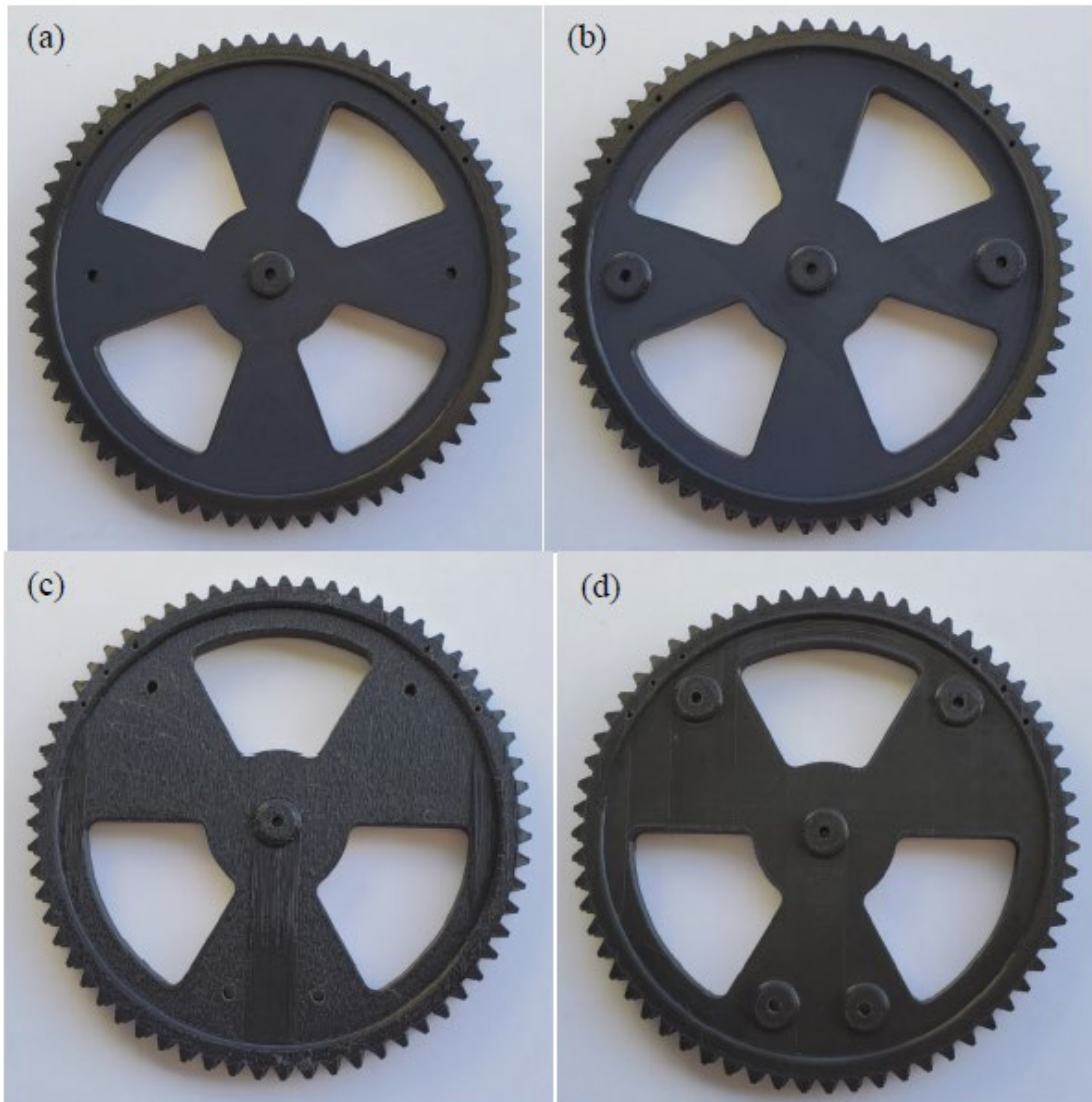


Figure 4.8: 3D printed gears: (a) gear type 1-front side, (b) gear type 1-rear side, (c) gear type 2-front side, and (d) gear type 2-rear side.

Figure 4.9 shows the worm design and its key. The model includes two worms; each drives a gear wheel on each axis rotation.

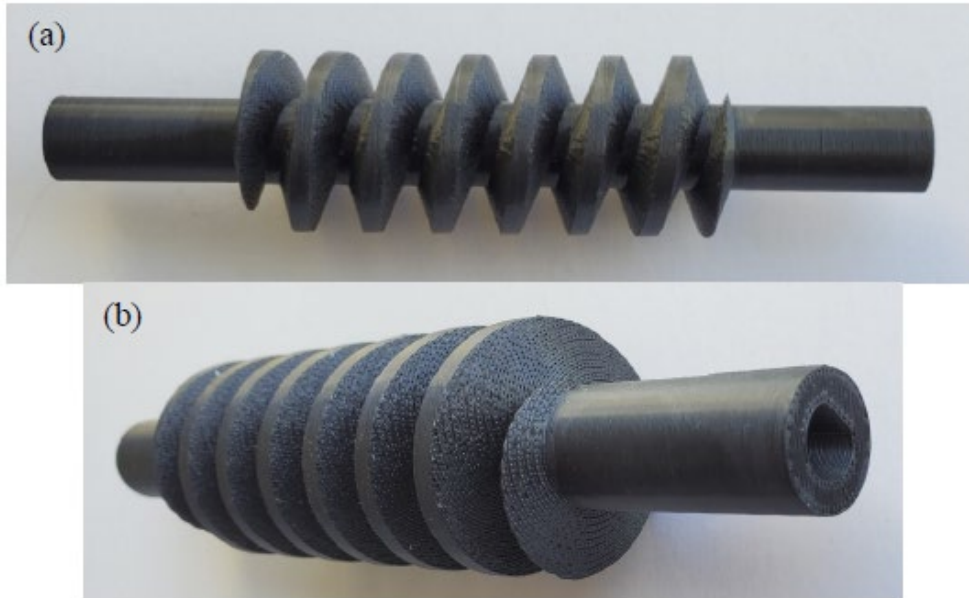


Figure 4.9: 3D Printed worm: (a) front view, and (b) perspective view showing the key of the worm shaft on the right side.

Located at the side of each worm there is a novel worm shaft support. In the upper hole of this support goes the worm shaft with the objective to keep alignment and hold the worm shaft. The two small holes in the bottom part have the function to be attached to the PCV pipe. See Figure 4.10.

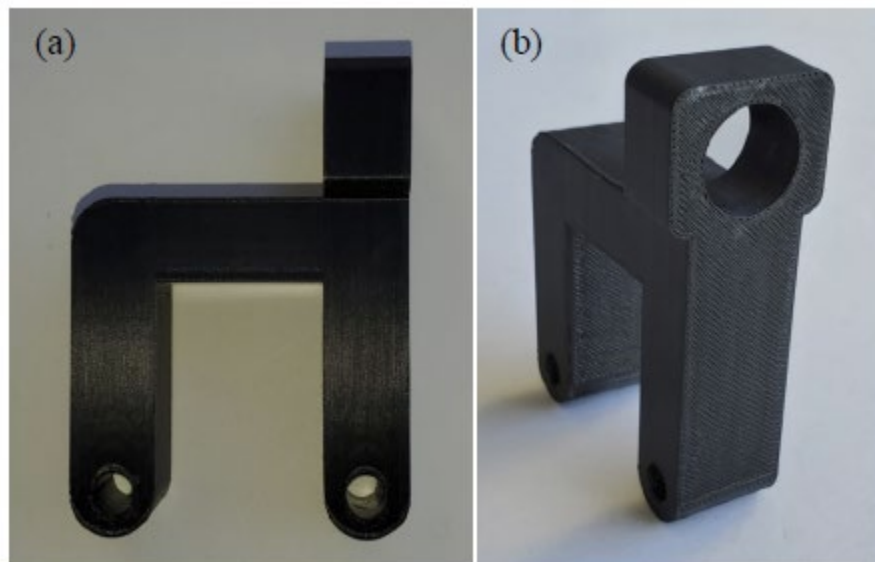


Figure 4.10: 3D printed worm shaft support: (a) and (b) are two different views of the part.

The project includes two novel sensor holders in the upper frame lens, located in opposite corners. Each of one contains two LDRs. See Figure 4.11.

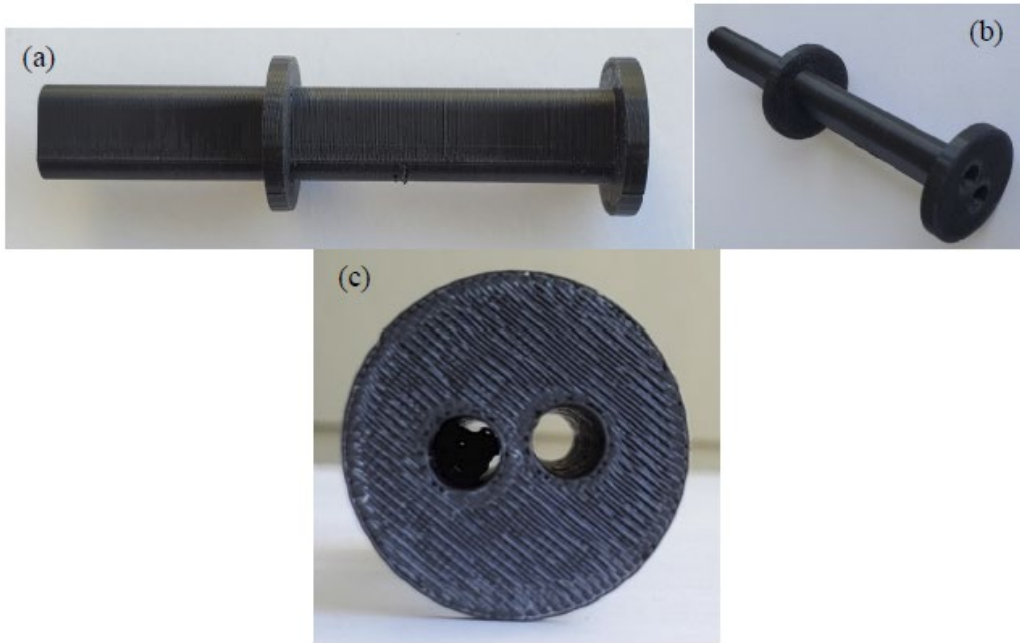


Figure 4.11: 3D printed sensor holder: (a) side view, (b) other view of (a), and (c) front view-before drilled, left side obstructed hole.

There are eight brackets. Attaching them by three holes with bolts, is possible to maintain joined each “V” vertical shape of PCV pipes to the upper frame. See Figure 4.12.



Figure 4.12: 3D printed brackets: (a) front view of the bracket showing three holes, and (b) other view of (a).

There are two stepper motor support boxes, each of them contains inside one stepper motor. By the two holes in the bottom part, they can be attached to the PCV pipe structure. The box support has a small hole in the bottom base of it to pass the wires of the stepper motor inside of the pipe. In addition, also there is a custom designed cap to avoid environmental issues due that these components work with electricity. The cap has four holes in each corner to be attached to its box using screws. See Figure 4.13.

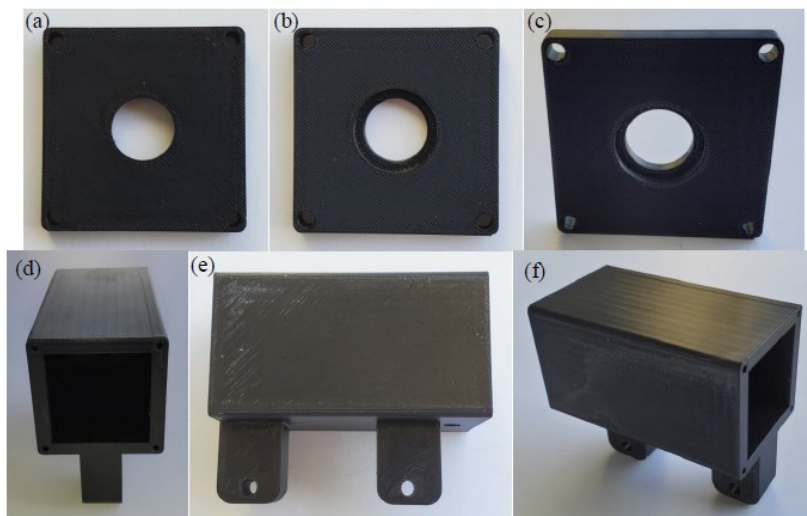


Figure 4.13: 3D printed stepper motor support: (a) front view of the cap, (b) rear view of the cap, (c) different rear view of the cap, (d) front side of the box support, (e) side view of the box support, are (f) two different views of the part.

Two novel stopper motion pads are located on each driver gear wheel. There four of these in the model. Figure 4.14.

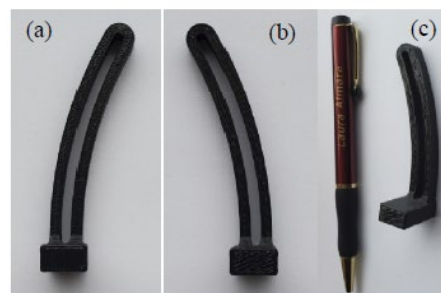


Figure 4.14: 3D stopper motion pad: (a) front view of the left stopper motion pad, (b) front view of the right stopper motion pad, and (c) other view and size comparison of (b).

Two brackets, one right and one left, support and hold the PV solar panel attached directly above of the controller box. The two holes are for be attached to the controller box, and the one hole in the further side id for attach the PV panel. See Figure 4.15.

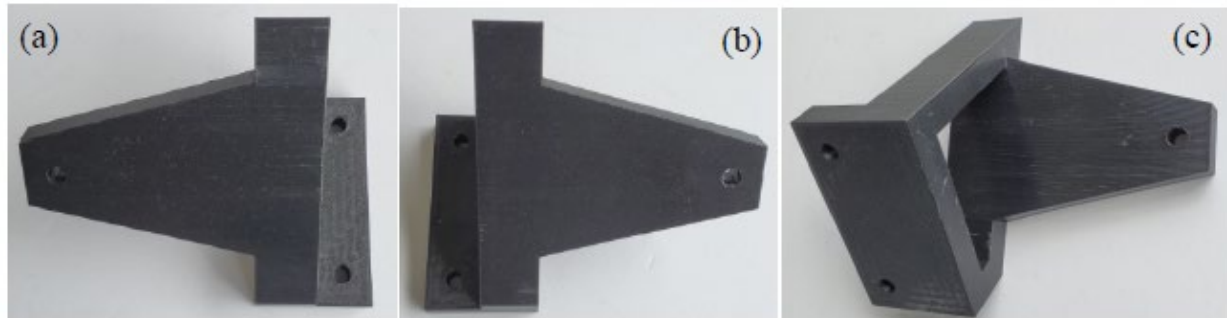


Figure 4.15: 3D printed solar brackets: (a) front view of the solar bracket left, (b) front view of the solar bracket right, and (c) downside view of (a).

4.3 Software

For this project was custom designed a logic code to perform automatically the movements of the solar tracker system. The code listing is in Appendix C.

4.3.1 Controller Logic

The values of the light measurements are processed by a microcontroller. For this project, the AMTEL328P was selected because it is a proven solution, confirmed by its use in several other projects about solar tracking.

One of the most common commercial implementations of this microcontroller is the Arduino Uno R3 board. This circuit board was selected because it integrates the microcontroller, the USB to program and debug it, several LED's that indicate the state, several options to power it, and analog and digital inputs and outputs.

This microcontroller is programmed is a language very similar to C, for which there are

many libraries. In this project, the routines for timers and stepper motors are used. The program used was created with Arduino 1.8.13, and is listed in Appendix C.

The microcontroller logic is based on a timer that is periodically activated. While inactive, the device consumes low energy. There are actions, like manual control, that are performed at short activation periods, but other actions, such as sensing and moving the mechanical parts to follow the sun, can be executed at larger intervals, using a countdown.

The logic obtains the difference in light from the sensors, and activates the stepper motors to move in the direction that makes the difference less than a set sensitivity threshold. This is so because the Arduino board analog to digital converters (ADC), which translate the input voltages from the sensors in a number between 0 and 1023, present small variations from measurement to measurement. To avoid random mechanical movements, the logic is set to activate the motors if the measured values are greater than some small threshold.

The logic is designed so that, after following the sun all day, the mechanical parts reach a position facing West, at a very low angle with the horizontal. There is a sensor (a simple switch) that is activated at the point. If the light levels are low (meaning that night has come), the logic generates the signals to move Fresnel to the East position, to be prepared for the next morning.

The tracking logic becomes inactive for low light intensities, at night, to prevent unwanted movements.

4.3.1.1 The Mechanical Movements

The microcontroller provides the signals to generate mechanical movements, but these are low power signals. There is a special device, the stepper motor driver, that takes the

microcontroller outputs as inputs, the energy from the power source, and generates the currents to produce motion.

The stepper motors transform the current from the stepper motor drivers into movement. These devices have an internal mechanical gear system to reduce speed in a 100:1 relation, meaning that the rotation of the motor shaft is very smooth.

The stepper motor shaft drives a worm gear to move the Fresnel lens. This provides more speed reduction, according to the relative slow motion of the sun along the day and year.

4.3.1.2 The Power Source

These are the elements that require energy to work: the stepper motors, the stepper motor driver, and the microcontroller. All these devices can work with a voltage between 5 and 24 volts, though the recommended value is 12 V.

The energy for this project is provided by a 12 volts battery with a capacity of 10 Ampere Hour, making this device self powered, being off electrical grid.

The energy used by the controller logic is higher when active, but low when inactive.

This current needs adds up to less than 1 A when the device is activated, meaning that, on average, the current requirement is very small. This makes the 10 Ampere Hour battery capacity able to last longer.

4.3.2 Electronic and Electric Circuit

An electronic and electric circuit was designed for the automatic dual-axis solar tracker system. Next diagram shows the relationship and connections between the main components, such as two stepper motors, a microcontroller, and two stepper motor drivers. Other

components are the four push buttons switches for manual positioning, the four push buttons switches to stop the motors when they reach a limit, an ON/OFF switch, a battery, a LED light, the four LDRs, resistances, capacitors, and the solar panel to keep the battery charged.

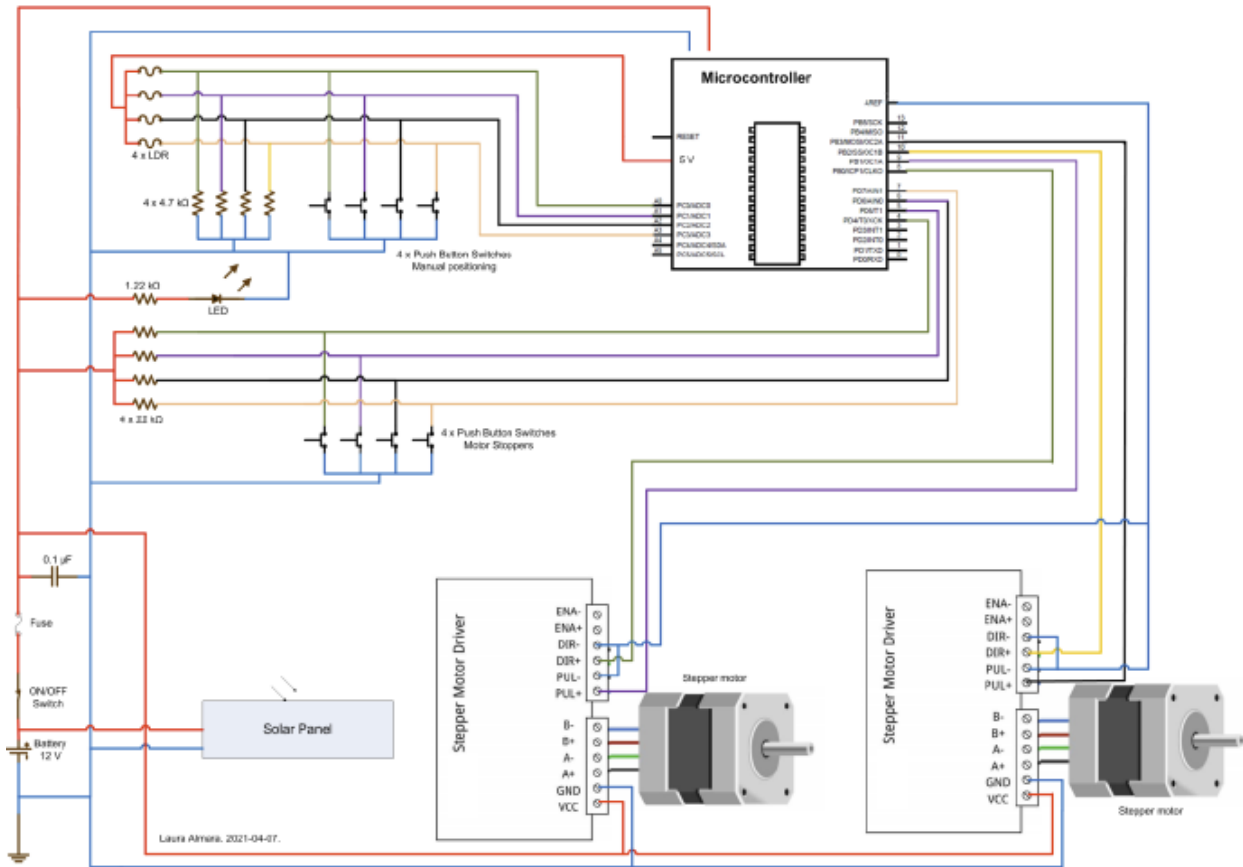


Figure 4.16: Electronic and electric circuit of the dual-axis solar tracking system.

4.3.3 Flowchart of the Algorithm Logic of the Automatic Dual Solar Tracking System

An algorithm was designed for the automatic dual-axis solar tracker system. The code presents two main parts: the light sensing and the manual positioning.

The light sensing part of the code commands the orientation of the upper lens frame, which holds the lens, directs it perpendicular to the sun, to obtain the maximum energy and heat during the day time harvesting. The algorithm was designed to automatically track the sun.

The logic is activated periodically, at configurable intervals. This time interval (configurable seconds, minutes, hours), currently 0.7 seconds, determines how frequently the logic in the microcontroller (brain) processes the signals from the photo-resistors (LDRs) to make a physical movement if it is needed. This custom time will depend mainly in the energy consumption of the stepper motors. If the energy consumption is higher than the harvesting solar energy in a particular application, then a larger time interval will be needed to save energy. If the time interval is set up to be every 4 minutes the microcontroller runs the code and makes runs the action. The solar tracker project runs unconnected to a power grid, using energy from a battery, recharged by a solar panel.

The simplified flowchart in Figure 4.17 shows the logic design. The constant *NIGHT* represents the illumination value after sunset. It can be setup to a value of about 100 analog-digital converter units.

The constant *SENSITIVITY* represents a dead zone, where none of the sensors is activated. It has a low value, such as 15. This is because the analog-digital converters present some variation in their measurements, making the system somehow unstable. The sensitivity band prevents that the fast electronic variations affect the physical parts.

The variables *azR* and *azL* represent the luminosity measured by the microcontroller in the azimuth direction, in the range 0-1023. The values of *e/R* and *e/L* represent the values in the elevation direction.

The variable *diff* is the difference between azimuth or elevation measured values. The device works on the difference of light received by two sensors.

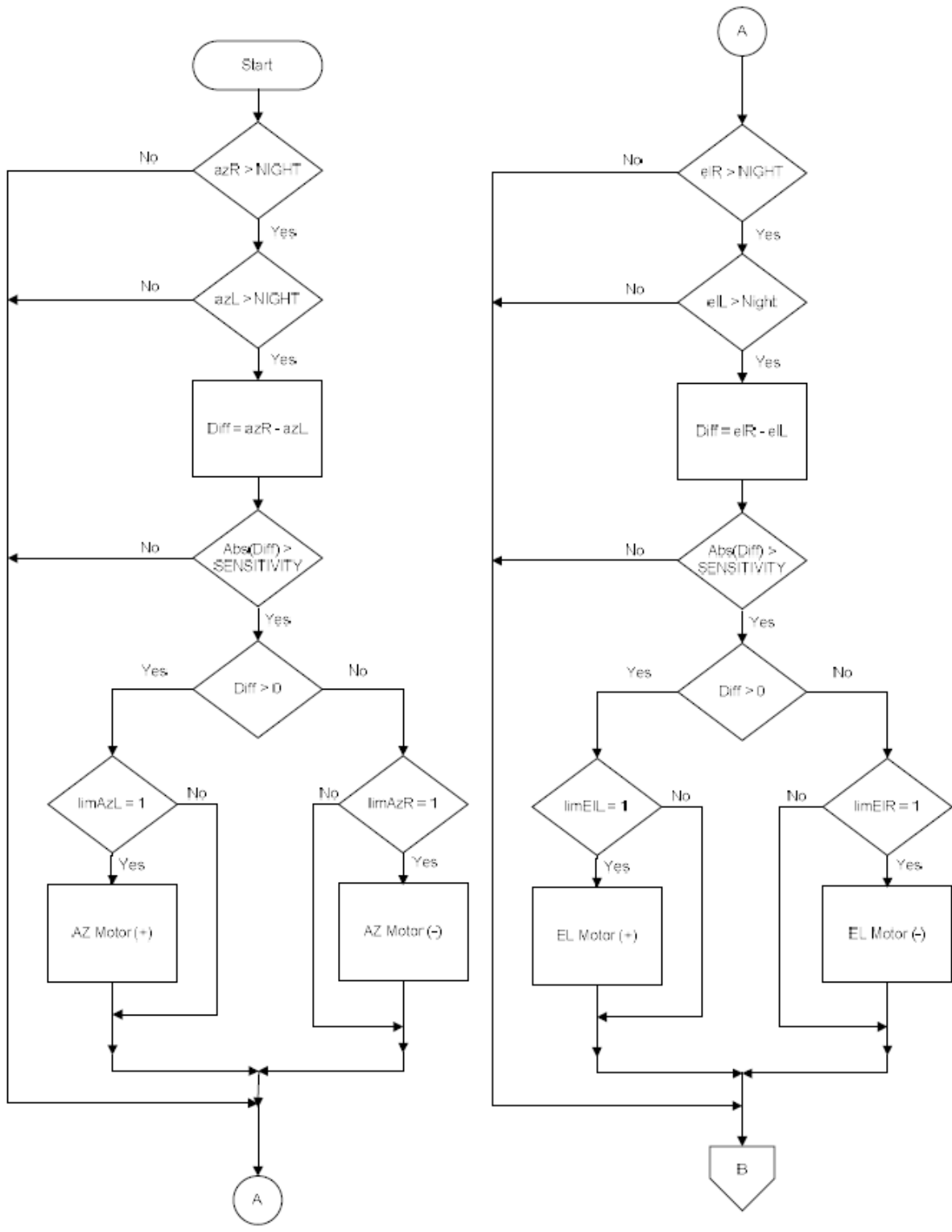


Figure 4.17: Flowchart of algorithm for light sensing of the automatic dual solar tracking system.

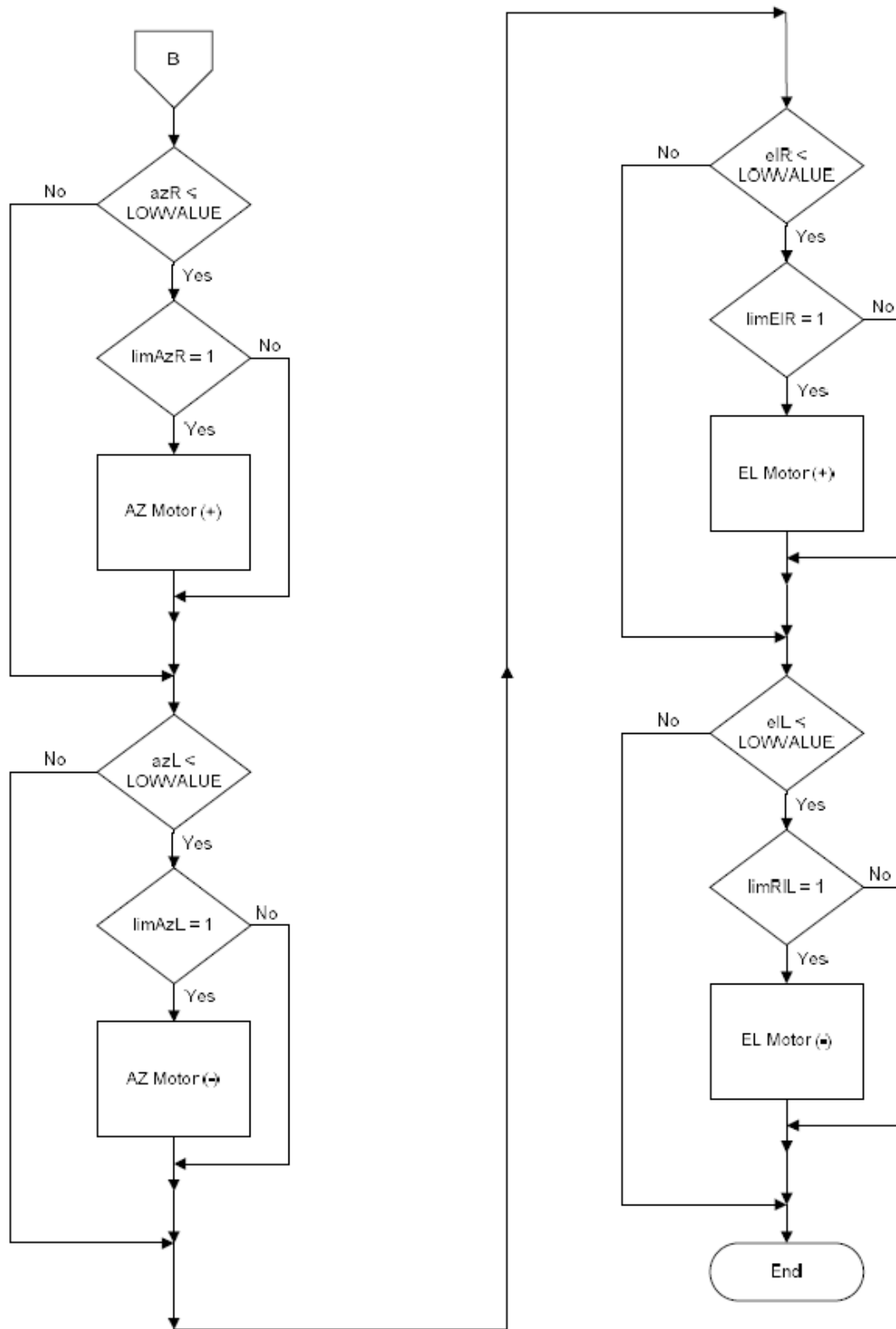


Figure 4.18: Flowchart of algorithm for manual positioning of the automatic dual solar tracking system.

As a safe action, there are four limiting switches in total, two for each axis of rotation. When the gear rotation reaches a maximum adjustable angle of inclination, the limiting switch is activated due to the touch gear stopper motion component attached to the gear as explained in sections 3.4.5 and 4.1.1.4. The variables *limAzR* and *limAzL* hold true/false values, representing if the limiting switches are activated or not, the same for *limEIR* and *limEIL*. The blocks containing *AzMotor* and *EIMotor* represent the activation of each of the motors.

The second part of the flowchart corresponds to the manual positioning of the solar tracker. These are the four push button switches located in the cover of the controller box. There are circumstances in which it could be needed to rotate the upper lens frame using these buttons without the automatic light sensors. For instance, during cloudy time if a movement of the upper lens frame is needed because of device relocation, it is still possible to move it due to this manual positioning option. The logic for these four buttons is shown in Figure 4.18.

4.3.4 Day/Night Mode

The circuit is setup with the concept that it becomes inactive in darkness. It is the simpler and cheaper form. The sensors are active if the measured light is over a customizable threshold. Given the sensor placements and this threshold, a night passing vehicle or surrounding lights would not activate movements. Also, at periodically configurable intervals it wakes up and checks the light sensor state, to rotate the stepper motors.

The other option would be to use a Real Time Clock (RTC), but it has the following disadvantages:

- Independent Battery

- This hardware would require some of the following items to set and update the configuration (maybe once a month). The options to perform the time adjustment would be:
 - a service person on site to set the time for a specific location (there may be thousands of desalination systems).
 - a computer application (PC, Apple and Linux) that connects to USB to be run by the final user.
 - wireless hardware (Bluetooth or internet) and a cell phone application.
 - wireless hardware and internet access to an NTP server to synchronize the clock. This may require dealing with firewalls, IP addresses and home networks.

4.3.5 Automatic Relocation of the Fresnel lens for the Next Day

Relocating the lens at the horizontal position has the disadvantage that this would require to sense this horizontal position, adding more sensors and more complex code.

Because of this, the design is that at the end of the day, the frame will be pointing to the West, and we can sense the end of the movement. The device will automatically return to the East position if the light level is below a threshold, meaning we are at night, until the East position is verified with another sensor. These two position sensors, which sense the position for relocation, are the same that do the function to make safety the run movement range of the solar tracking system. Therefore, with this relocation logic, there is no need to add extra sensors and complexity to the code.

CHAPTER 5

PROTOTYPE TESTING

5.1 Worm-Gear Assembly

The worm gear and wheel assembly was tested to verify that they run smoothly, and that the parts fit in their places. The housing of the stepper motors had the right size, and the shaft support was at the required distance.



Figure 5.1: Worm gear assembly testing.

5.2 Novel Sensor Holder

The sensor assembly is composed of the cylindrical hollow holders. One of the photo-resistors goes at the top, and the other one is at the bottom. This way, one of the sensors receives all the sun light, but the other one is only fully illuminated when the two cylinders are

pointing to the sun. As the device works on light differences, any variation in luminosity causes the microcontroller generate movements in the stepper motors to compensate.

This assembly was tested to perform as expected.

Figure 5.2 shows a picture of the test performed with full direct sunlight and 35% cloud cover at 4:42 PM (unfavorable inclination), in Winter.

When one of the sensors is in the shadow, the other sensor is in light, and the stepper motor changes the rotational direction. When both sensors get the same light intensity, the motor stops. The last second of the video shows how the stepper motor stops when the sensors receive the same amount of sunlight.

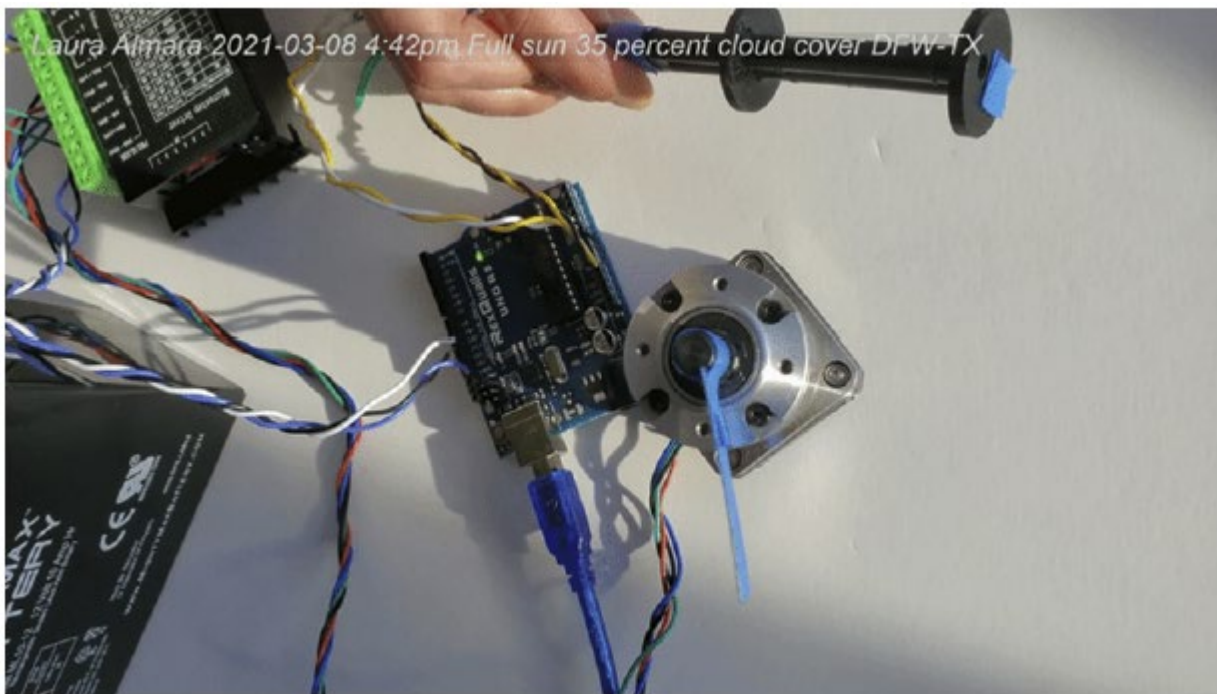


Figure 5.2: Testing of the sensor holder with full direct sunlight: 35% cloud cover.

Figure 5.3 illustrates picture of another test performed with full direct sunlight and, in this case, in Winter, 1% cloud cover at 4:09 PM (unfavorable inclination). This hour was selected because the Sun had an inclination and the sunlight had less intensity. Therefore, if in this

conditions the sensor support works, is expected that it also works during the all range sunny day. The results were the expected ones. The novel design of the sensor support applies very well the shadow concept, with highly precision at the moment to sense the incoming light.

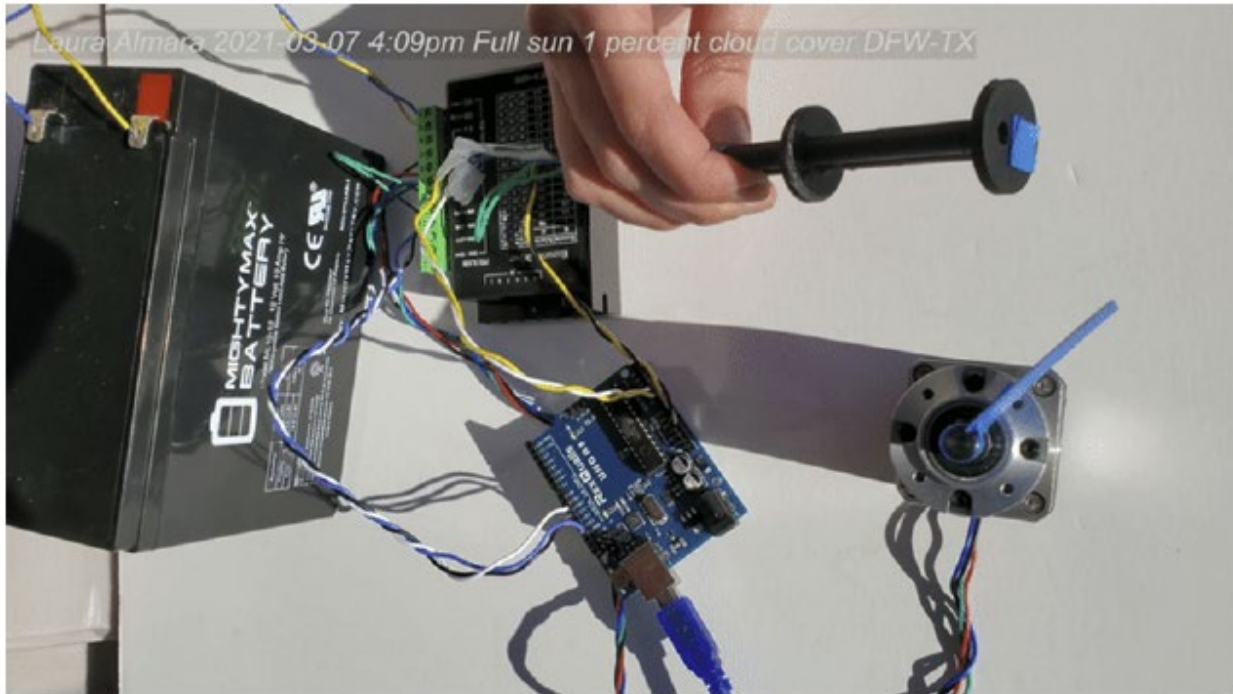


Figure 5.3: Testing of the sensor holder with full direct sunlight: 1% cloud cover.

5.3 Manual Positioning Switches and Stopper Motion Pads

Figure 5.4 shows two pictures of a video: (a) when a switch of the manual control is activated, the movement of the solar tracker change according to the button activated, and (b) illustrates the switch of stopping motion when is touched by the right side stopper motion pad, the movement of rotation stops. The human arm in Figure 5.4 (a) gives a size scale comparison respect to the solar tracker system.

The four manual positioning switches and the four stopper motion pads worked as expected.



Figure 5.4: Testing of (a) manual positioning switches, and (b) switches of stopping motion and the right side stopper motion pad.

5.4 Solar Tracker System

The assembled device was tested to follow a bright light source; both, azimuth and elevation sensors, worked as expected.

Figure 5.5 is a picture of a video in which the solar tracking system is being tested. The PVC parts that cover the sensor holder were removed due to the test was performed indoors

and there is less sun intensity inside. The covers help to make smooth the intensity of the incoming sun rays. Solar tracker worked as expected.

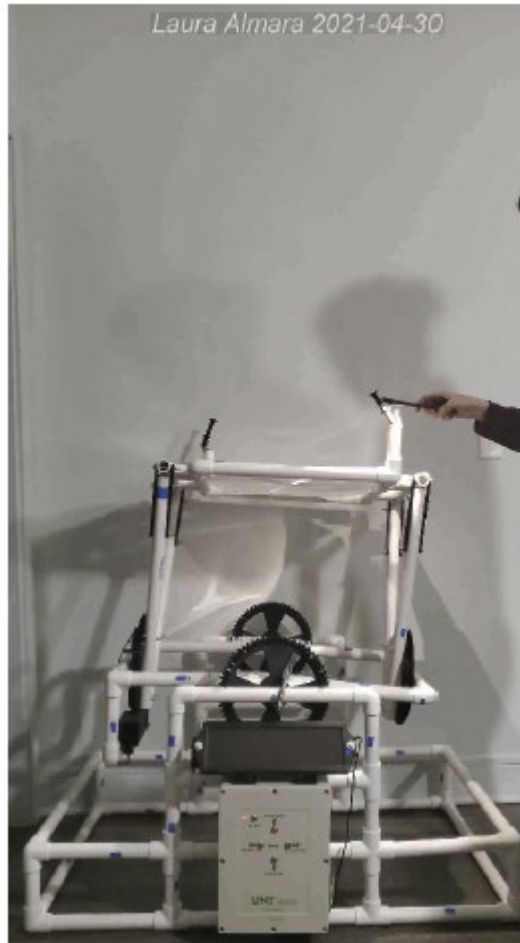


Figure 5.5: Test of the dual-axis solar tracker system.

CHAPTER 6

PROJECT COST AND ANALYSIS







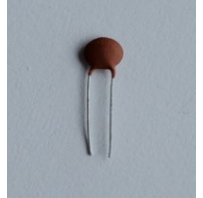
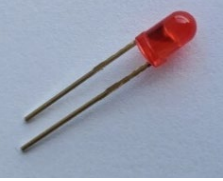




6.1 Project Cost











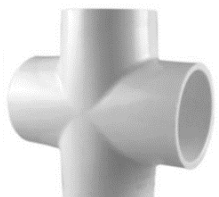

Table 6.1 lists in detail the bill of materials and costs corresponding to the fabrication of the dual-axis solar tracker system. A description, picture, quantities used, unit and total weights and prices are mentioned, as well as the assembly category to which each of the components belong. In addition, the totals of weight and price are also provided.

The solar tracker project has approximately a total weight of 37.82 lbs (16.59 kg).

Table 6.2 summarizes the total costs of the fabrication of the project, grouped by categories. The author constructed the prototype; therefore there are no construction costs. Electronic components are the cheapest, with a value of \$36.53, being the most expensive parts the microcontroller and stepper motor drivers. The Fresnel lens, optics category, has a value of \$198. Electric components have a total cost of \$230.96, and the most expensive parts are the stepper motors. Structure cost category is divided into two parts: structural frame and 3D printing. Structural frame includes the parts that form the structure of the solar tracker system, which are not 3D printed parts. For example, PVC pipes, elbows, nuts, washers, etcetera. This category is the cheapest inside the structure category, having a cost of \$124.35. On the other hand, 3D printing category includes all 3D printed parts, which are black color in the whole structure. 3D printed parts are the most expensive in this prototype project, \$1,549.85. In total, the project cost is \$2,139.69.

Table 6.1: Detailed bill of materials and costs of the dual-axis solar tracker system.

Item	Part	Picture	Assembly Category	Qty	Unit Weight		Total Weight		Unit Price [USD]	Total Price [USD]
					[lbs]	[kg]	[lbs]	[kg]		
1	Fresnel lens Diameter: 500 mm Thickness: 3 mm		Optics	1	1.56	0.707	1.56	0.707	198.00	198.00
2	LDR		Electronic	4	0	0	0	0	0.14	0.57
3	Microcontroller		Electronic	1	0.13	0.059	0.13	0.059	11.98	11.98
4	Heat Shrink Tubing Tube		Electronic	Qty Req	0	0	0	0	0.00	0.00
5	Stepper motor driver		Electronic	2	0.35	0.159	0.35	0.159	11.99	23.98
6	Resistors 22 and 4.7 kΩ		Electronic	9	0	0	0	0	0.00	0.00
7	Capacitors 0.1μF		Electronic	3	0	0	0	0	0.00	0.00
8	LED light		Electronic	1	0	0	0	0	0.00	0.00
9	Stepper motor		Electric	2	1.32	0.60	2.64	1.2	41.75	83.50
10	On/off button		Electric	1	0.04	0.018	0.04	0.018	5.95	5.95
11	Safety stop motion push button		Electric	8	0.04	0.018	0.16	0.071	6.00	47.96
12	Automotive Extension Cable 18AWG		Electric	1 pair	0.033	0.0283	0.033	0.0283	1.00	1.00

Item	Part	Picture	Assembly Category	Qty	Unit Weight		Total Weight		Unit Price [USD]	Total Price [USD]
					[lbs]	[kg]	[lbs]	[kg]		
13	Cable Wire, 12V 5A Male & Female Connectors		Electric	1 pair	0.0625	0.015	0.0625	0.015	1.00	1.00
14	Battery		Electric	1	5.85	2.654	5.85	2.654	23.99	23.99
15	Battery terminal		Electric	2	0.03	0.012	0.03	0.012	0.80	1.59
16	Connecting wires		Electric	1 pack	0.95	0.431	0.95	0.431	14.99	14.99
17	Outdoor plastic electrical box		Electric	1	2.14	0.971	2.14	0.971	29.99	29.99
18	Solar battery charger		Electric	1	2.74	1.243	2.74	1.243	21.00	21.00
19	1" x 10' PVC Tube SCH 40		Structure	5			6.66	3.021	4.37	21.85
20	1" PVC side outlet 90 Deg Elbow sxsxs		Structure	12	0.099	0.045	1.188	0.54	2.80	33.60
21	1" PVC 90 Deg Elbow		Structure	10	0.06	0.027	0.6	0.27	0.55	5.49
22	1" PVC Tee sxsxs		Structure	26	0.08	0.036	2.08	0.936	0.99	25.69
23	1 in. PVC Schedule 40 SxSxSxS Cross		Structure	2	0.221	0.1	0.442	0.2	3.13	6.26
24	1 in. x 1/2 in. PVC Sch. 40 Bushing		Structure	2	0.053	0.024	0.106	0.048	1.02	2.04

Item	Part	Picture	Assembly Category	Qty	Unit Weight		Total Weight		Unit Price [USD]	Total Price [USD]
					[lbs]	[kg]	[lbs]	[kg]		
25	1 in. PVC Schedule 40 SxS Coupling		Structure	2	0.075	0.034	0.15	0.068	0.66	1.32
26	Hex Bolt Zinc 1/4 x 4-1/2		Structure	2	0.05	0.0227	0.1	0.0453	0.45	0.90
27	Hex Bolt Zinc 1/4 x 2-1/2		Structure	34	0.04	0.0181	1.36	0.6154	0.25	8.50
28	Flat Washers Zinc 1/4		Structure	76	0.06	0.02	4.56	1.52	0.13	9.88
29	Hex Nut Zinc 1/4		Structure	46	0.02	0.009	0.92	0.414	0.08	3.68
30	Gutter Screws #8 x 3/8 in		Structure	4	0.036	0.0163	0.144	0.0653	0.11	0.44
31	Hinge Screws #7 x 3/4 in		Structure	6	0.002	0.0009	0.012	0.0054	0.08	0.48
32	Machine Screws #8-32x5/8 in		Structure	6	0.01	0.0045	0.06	0.027	0.15	0.89
33	Machine Screws #6-32x1 in		Structure	8	0.01	0.0045	0.08	0.036	0.15	1.18
34	Corner Braces 1-1/2"		Structure	3	0.0195	0.0088	0.0585	0.0265	0.72	2.16
35	Gear type 1		Structure	2	0.371	0.169	0.743	0.337	1,549.85	

Item	Part	Picture	Assembly Category	Qty	Unit Weight		Total Weight		Unit Price [USD]	Total Price [USD]
					[lbs]	[kg]	[lbs]	[kg]		
36	Gear type 2		Structure	2	0.355	0.161	0.710	0.322		
37	Worm		Structure	2	0.120	0.055	0.240	0.109		
38	LDR Sensor Holder		Structure	2	0.009	0.004	0.018	0.008		
39	Stepper Motor Support Cap		Structure	2	0.013	0.006	0.026	0.012		
40	Stepper Motor Support Only		Structure	2	0.179	0.081	0.357	0.162		
41	Shaft Support		Structure	2	0.046	0.021	0.093	0.042		
42	Right Stopper Motion Pad		Structure	2	0	0	0	0		
43	Left Stopper Motion Pad		Structure	2	0	0	0	0		
44	Bracket 7.5" x 3/4"-1/4 Thick		Structure	8	0.018	0.008	0.148	0.067		
45	Solar Bracket Right		Structure	1	0.139	0.063	0.139	0.063		
46	Solar Bracket Left		Structure	1	0.138	0.063	0.138	0.063		
Total							37.82	16.59		2,139.69

Table 6.2: Summarize of project cost by categories.

Part Category		Cost [USD]
Construction		0.00
Electronic		36.53
Optics		198.00
Electric		230.96
Structure	Structural Structure	124.35
	3D Printing	1,549.85
TOTAL		2,139.69

Figure 6.1 and 6.2 illustrate a comparison of costs by categories. Clearly, 72.43% of the total cost of the project is due to 3D printing, and this is represented by a red bar in Figure 6.1. Regarding 3D printing, technician hours were 0.0833 and cost \$2.92, \$35 per hour, representing 0.19% of the total 3D printing cost work. The total machine hours were 117.17 and cost \$1,406.04, \$12 per hour, being 91% of the total 3D printing cost work. Lastly, the overhead costs (machine space occupancy, administrative costs, power, etc.) represent 9.1%, therefore, the overhead costs was \$140.09. See Figure 6.3. These forms a total 3D printing work cost of \$1,549.85.

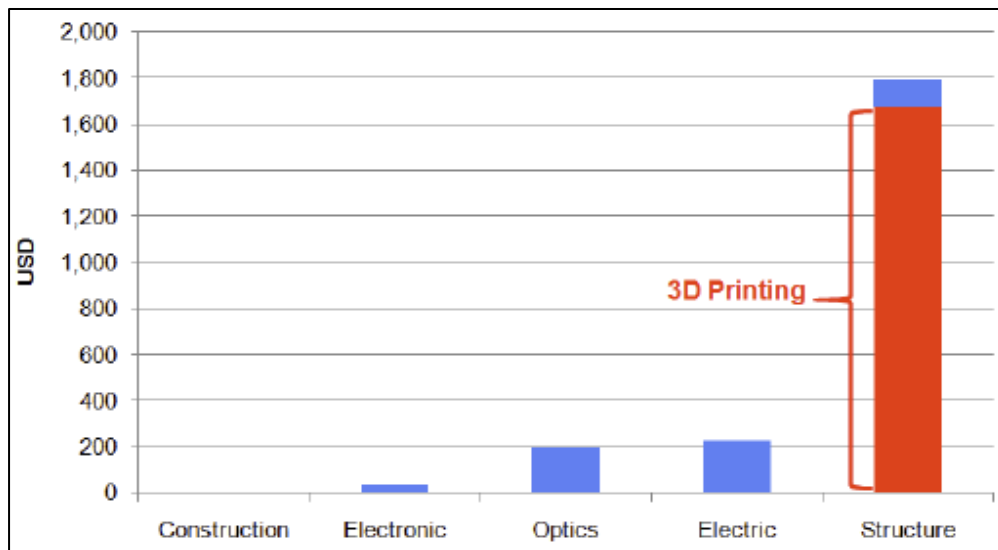


Figure 6.1: Summary of the project cost by categories.

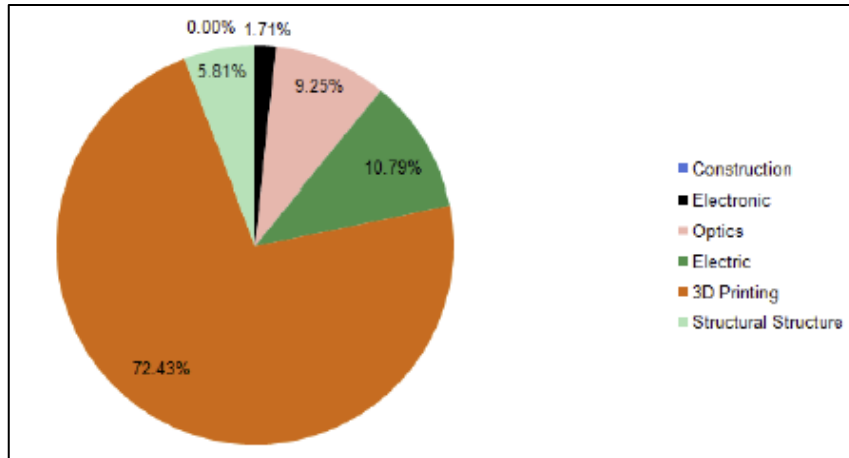


Figure 6.2: Prototype cost by percentage contribution of each part category.

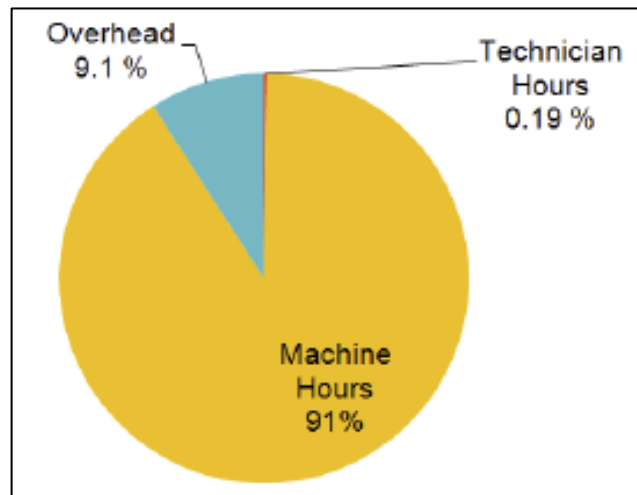


Figure 6.3: 3D printing costs.

6.2 Comparison with Other Projects

It is difficult to find cost of the projects presented on publications. Generally, designs that are fabricated in research are also prototypes, having also high costs because they are not a product yet, which can be made by mass fabrication (less total cost and prices per unit). As mentioned in the literature review section, there is more research about projects including PV solar panel than using Fresnel lenses, becoming a challenge the comparison of the cost of this project.

However, a project suggested by Özer et al. [28], shows a total cost of \$90.09, and

Amadi et al. [18] presents a total cost of \$1,402.20, both cases for PV solar panel applications. Using a Fresnel lens, Allil [31] suggested a project with a total cost of \$5,000.

Notice that fabrication of the structures for a Fresnel lens application may have higher costs than PV solar panel application, due that the former one needs to have an empty area below the Fresnel lens to perform its purpose, meaning more components and materials being used.

6.3 Conclusions

The total project cost is reasonable considering the application for what it was designed. It could be mostly reduced by two forms: buying bulk materials and changing from 3D printing to custom parts fabrication.

Although the 3D printed parts are expensive, they have some advantages, such as unaffected by corrosion on the sea environment, lightweight, or the easy of customization if needed. In the case that the solar tracker is for placed near the sea to desalinate seawater, as is intended for the present project, the materials would have a longer life time span compared to other designs. Notice that 3D technology becomes cheaper with time, and machines provide better finishing. Structures built with steel tend to be heavier and prone to corrosion.

CHAPTER 7

CONCLUSIONS AND FUTURE WORK

7.1 Conclusions

The present project combines mechanical, electronic, electric, energy, software and simulation knowledge. It has two main parts, a variety of simulations using different software packages, and a design and fabrication part.

Four novel ideas were presented: dual-axis solar tracker system itself, sensor holder, the stopper motion pads (left and right), and the worm shaft support.

The dual-axis solar tracker was designed with the main objectives that the structure was portable, dismountable, lightweight, low cost, corrosion resistant, accurate, small size, follow the sun automatically, off-grid (electrical) and use green energy (solar powered). Also, the structure design should have an empty area directly below of the Fresnel lens (no obstacles on incoming sun rays to the receiver). The wiring goes inside the PVC pipes, being an advantage for movements and for the environment what surrounds the solar tracker.

The solar tracker project has approximately a total weight of 37.82 lbs (16.59 kg), dimensions of 46 x 36 x 48 in, and a total cost of \$2,139.69, 72.43% of it corresponds to 3D printed parts cost. The design presented on this project can be made with PVC pipes and 3D printed parts, as suggested, or substituting them by metal materials. The project has more than 400 parts, which in the CAD model, were detailed drawn in real scale. The 3D printed parts were detailed custom design.

Testing of sensing and movements parts were done, obtaining the expected performance.

Although the solar tracker design can be used for solve a tangible scarcity of fresh water issue with a concrete solution, the design can be used for other applications such as solar cooking, solar welding, PV panels, among others applications mentioned in section 1.3. The results of this work will be used to analyze the best chamber design and diameter of flat Fresnel lens, according to the fresh water output requirements. Results of temperature and heat flux values on the receiver surface obtained in this study can be used as a reference to investigate and apply in other Fresnel lens applications.

7.2 Future Work

The work and research previously detailed can be extended with complementary studies about the following points, (some of them could be a research project):

1. Perform tests to obtain the temperature measurements on the receiver surface due to the heat concentration created from the Fresnel lens, and compare to the results obtained in the simulations.
2. Perform tests of rotation of the dual axis tracking system during the harvesting daytime in all seasons, to obtain tracking error and accuracy values, and compare them to the corresponding values extracted from the literature review.
3. Explore options of receiver materials with high absorptive coating or thin plate, with the purpose to optimize the harvesting temperature.
4. In case that the application of the presented design in this project is to distill seawater, an interesting analysis would be to collect the data from a medium-sized family, to seek the water consumption needs, study the payback period of the dual axis solar tracking system, the costs that the family could save avoiding use on grid electricity, buying fresh water or fuel and time searching in town fresh water. Based on the obtained results, the project could be scaled up to whole communities.

APPENDIX A
SOLAR TRACKER TESTING PROCEDURES

Test	Action	Expected result
1	Push the Right labeled button.	The Fresnel lens should move to the right.
2	Push the Left labeled button.	The Fresnel lens should move to the left.
3	Push the Up labeled button.	The Fresnel lens should elevate.
4	Push the Down labeled button.	The Fresnel lens should move downwards.
5	Push the Right labeled button until the Fresnel lens reaches the limit.	The Fresnel lens should move to the right until it reaches the limit, and then stops
6	Push the Left labeled button until the Fresnel lens reaches the limit.	The Fresnel lens should move to the left until it reaches the limit, and then stops.
7	Push the Up labeled button until the Fresnel lens reaches the limit.	The Fresnel lens should elevate until it reaches the limit, and then stops.
8	Push the Down labeled button until the Fresnel lens reaches the limit.	The Fresnel lens should move downwards until it reaches the limit, and then stops.
9	After sunset, push the Right labeled button until the Fresnel lens reaches the limit.	The Fresnel lens should move to the right until it reaches the limit, and then it should move to the left, to the dawn position, and then stops.
10	Push the On/Off button.	The device should turn On and Off.
11	Using the Right labeled button, move the lens to the dawn position, and wait.	The Fresnel lens should follow the sun movement along the day.
12	Verify that there is no daylight, and wait.	The device should not activate itself. It does not follow the sun in a dark environment.

APPENDIX B

SOLAR TRACKER TROUBLESHOOTING PROCEDURES

Case	Symptom	Possible causes/fixes
1	The Fresnel lens does not move.	<p>The Fresnel lens tracking logic is periodically activated (about every 4 minutes). At inactive times, only the front panel push buttons are active.</p> <p>The internal battery is discharged.</p> <p>The luminosity is below daylight level. The device disconnects at night.</p> <p>The On/Off button is in the Off state.</p> <p>The system may require technical service.</p>
2	The Fresnel lens seems to lag tracking the sun.	<p>The lag is expected. The Fresnel lens tracking logic is periodically activated (about every 4 minutes). At inactive times, only the front panel push buttons are active.</p>
3	The Fresnel lens stops moving when it reaches a low angle with the horizontal.	<p>This is expected. There is a security switch that activates to prevent damage.</p>
4	The Fresnel lens does not track the sun.	<p>There may exist some obstruction in the light path to the sensors.</p>
5	The device does not move.	<p>This device requires sunlight to operate. Make sure that enough luminosity is present.</p>

APPENDIX C
MICROCONTROLLER CODE


```

// Solar tracker.

// Laura Almara, under GPL v3 license.
// 2021-02-13.

/*
Paul Stoffregen's modified TimerOne.
http://www.pjrc.com/teensy/td_libs_TimerOne.html
https://github.com/PaulStoffregen/TimerOne
http://playground.arduino.cc/Code/Timer1
TimerOne is free software. You can redistribute it and/or modify it under
the terms of Creative Commons Attribution 3.0 United States License.
To view a copy of this license, visit
http://creativecommons.org/licenses/by/3.0/us/
*/

/*
= Stepper Library for Arduino =
This library allows you to control unipolar or bipolar stepper motors.
http://www.arduino.cc/en/Reference/Stepper
Copyright (c) Arduino LLC. All right reserved.
Copyright (c) Sebastian Gassner. All right reserved.
Copyright (c) Noah Shibley. All right reserved.

This library is free software; you can redistribute it and/or
modify it under the terms of the GNU Lesser General Public
License as published by the Free Software Foundation; either
version 2.1 of the License, or (at your option) any later version.
*/

// Library routines.
#include <TimerOne.h>
#include <Stepper.h>

// Board verification pin.
#define boardLED 13

// LDR analog sensor pins.
#define azimuthLeftPin 2 // azimuth left LDR
#define azimuthRightPin 3 // azimuth right LDR
#define elevationLeftPin 0 // elevation left LDR
#define elevationRightPin 1 // elevation right LDR

// Security digital pins.
#define limitAzimuthLeft 6
#define limitAzimuthRight 5
#define limitElevationLeft 7
#define limitElevationRight 4

// Timmings.
#define ReadDelay 25
#define StepperDelay 200

```

```

// Thresholds
#define SENSIBILITY 10
#define NIGHT      7
#define LOWVALUE   2

// Timer1 variables.
volatile bool isBusy;

#define stepsPerRevolution 32767

// Azimuth servo motor variables.
Stepper stepperAzimuth(stepsPerRevolution, 10, 11);
volatile int azLeft = 0;
volatile int azRight = 0;
volatile int azimuthDelta = 0;

// Elevation stepper motor variables.
Stepper stepperElevation(stepsPerRevolution, 8, 9);
volatile int elLeft = 0;
volatile int elRight = 0;
volatile int elevationDelta = 0;

// Security limits.
volatile int limAzLeft;
volatile int limAzRight;
volatile int limElLeft;
volatile int limElRight;

// Misc variables
volatile int total = 0;

// Simulated delay because inside timer service.
void simulatedDelay(int aTimes)
{
  int a;
  int iters = 1000 * aTimes;
  for (long i = 1; i < iters; i++)
  {
    a = 987;
  }
  if (a == 0)
  {
  }
}

// Setup pins and stepper motors.
void setup ()
{
  Timer1.initialize(700000); // microseconds = 0.7 seconds
  Timer1.attachInterrupt(timerHandler);

  isBusy = false;
  pinMode(boardLED, OUTPUT);

```

```

pinMode(limitAzimuthLeft, INPUT_PULLUP);
pinMode(limitAzimuthRight, INPUT_PULLUP);
stepperAzimuth.setSpeed(60);
pinMode(limitElevationLeft, INPUT_PULLUP);
pinMode(limitElevationRight, INPUT_PULLUP);
stepperElevation.setSpeed(60);

simulatedDelay(StepperDelay);
}

// Main loop routine.
void loop()
{
  // Do nothing in the main loop.
  // All happens in the timer handler.
}

// Timer1 interrupt service routine.
void timerHandler()
{
  if (! isBusy)
  {
    isBusy = true;

    // Read the azimuth LDR sensor values.
    azLeft = analogRead(azimuthLeftPin);
    simulatedDelay(ReadDelay);
    azRight = analogRead(azimuthRightPin);
    simulatedDelay(ReadDelay);

    limAzLeft = digitalRead(limitAzimuthLeft);
    simulatedDelay(ReadDelay);
    limAzRight = digitalRead(limitAzimuthRight);
    simulatedDelay(ReadDelay);

    // Read the elevation LDR sensor values.
    elLeft = analogRead(elevationLeftPin);
    simulatedDelay(ReadDelay);
    elRight = analogRead(elevationRightPin);
    simulatedDelay(ReadDelay);

    limElLeft = digitalRead(limitElevationLeft);
    simulatedDelay(ReadDelay);
    limElRight = digitalRead(limitElevationRight);
    simulatedDelay(ReadDelay);

    if (true)
    {
      total = total + 1;

      // Follow the light source only if there is enough luminosity and not stopped.
      if (true)

```

```

{
  azimuthDelta = abs(azRight - azLeft);
  if ((azimuthDelta > SENSIBILITY) && (azLeft > NIGHT) && (azRight > NIGHT) && limAzLeft && limAzRight)
  {
    if (azRight > azLeft)
    {
      digitalWrite(boardLED, HIGH);
      if (limAzLeft)
      {
        stepperAzimuth.step(stepsPerRevolution);
        simulatedDelay(StepperDelay);
      }
    }
    else
    {
      digitalWrite(boardLED, LOW);
      if (limAzRight)
      {
        stepperAzimuth.step(-stepsPerRevolution);
        simulatedDelay(StepperDelay);
      }
    }
  }
}

elevationDelta = abs(eIRight - eLeft);
if ((elevationDelta > SENSIBILITY) && (eLeft > NIGHT) && (eRight > NIGHT) && limELeft && limERight)
{
  //Serial.println(elevationDelta, DEC);
  if (eRight > eLeft)
  {
    digitalWrite(boardLED, HIGH);
    if (limELeft)
    {
      stepperElevation.step(stepsPerRevolution);
      simulatedDelay(StepperDelay);
    }
  }
  else
  {
    digitalWrite(boardLED, LOW);
    if (limERight)
    {
      stepperElevation.step(-stepsPerRevolution);
      simulatedDelay(StepperDelay);
    }
  }
}

}
}

// Manual azimuth left adjustment.
if ((azLeft <= LOWVALUE) && (azRight > NIGHT) && limAzLeft)

```

```

{
  digitalWrite(boardLED, HIGH);
  stepperAzimuth.step(-stepsPerRevolution);
  simulatedDelay(StepperDelay);
}

// Manual azimuth right adjustment.
if ((azRight <= LOWVALUE) && (azLeft > NIGHT) && limAzRight)
{
  digitalWrite(boardLED, HIGH);
  stepperAzimuth.step(stepsPerRevolution);
  simulatedDelay(StepperDelay);
}

// Manual elevation left adjustment.
if ((elLeft <= LOWVALUE) && (elRight > NIGHT) && limElLeft)
{
  digitalWrite(boardLED, HIGH);
  stepperElevation.step(stepsPerRevolution);
  simulatedDelay(StepperDelay);
}

// Manual elevation right adjustment.
if ((elRight <= LOWVALUE) && (elLeft > NIGHT) && limElRight)
{
  digitalWrite(boardLED, HIGH);
  stepperElevation.step(-stepsPerRevolution);
  simulatedDelay(StepperDelay);
}

// Return to the East after sunset.
if ((! limAzLeft) && (azRight < NIGHT) && (azLeft < NIGHT) && (elRight < NIGHT) && (elLeft < NIGHT) )
{
  while (! limAzRight)
  {
    stepperAzimuth.step(-stepsPerRevolution);
    simulatedDelay(StepperDelay);
    limAzRight = digitalRead(limitAzimuthRight);
  }
  for (int i = 0; i < 1000; i++)
  {
    stepperAzimuth.step(stepsPerRevolution);
    simulatedDelay(StepperDelay);
  }
}

digitalWrite(boardLED, LOW);
isBusy = false;
}
}

```

APPENDIX D
POSSIBLE IMPROVEMENTS

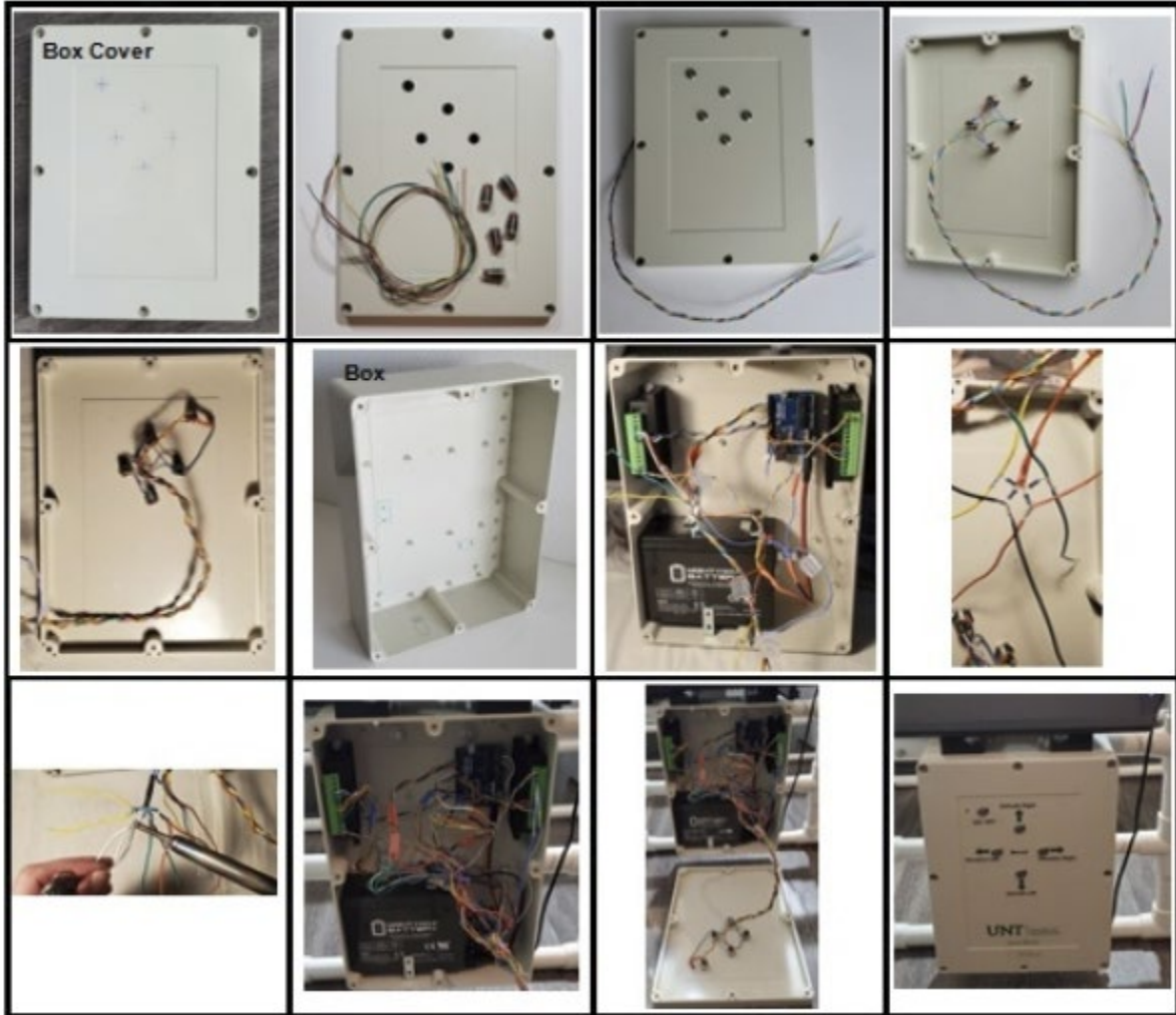
The following improvements can be made as results of observations during testing:

- The worm gears and wheel could be metallic.
- The worm gears could have a globoid design, to improve contact and durability.
- The mechanical structure could be reinforced, or even be made of metal.
- The positioning of the motor stopper switches could be some millimeters closer to the pads.
- Some electric connectors could be added in strategic places, to make flexible disassemblies.
- In the shaft hole of the stepper motor support cap could be added an o-ring to avoid the entrance of rain and dust.
- To avoid movements between pipes and elbows, especially in the upper and middle frame, generated by normal use, they could be tightened using specific glue, which can be easily removed in the case of disassembly.
- PVC caps can be placed at the end of few parts of the frame structure to avoid the entrance of rain and dust, also providing better look and finishing.

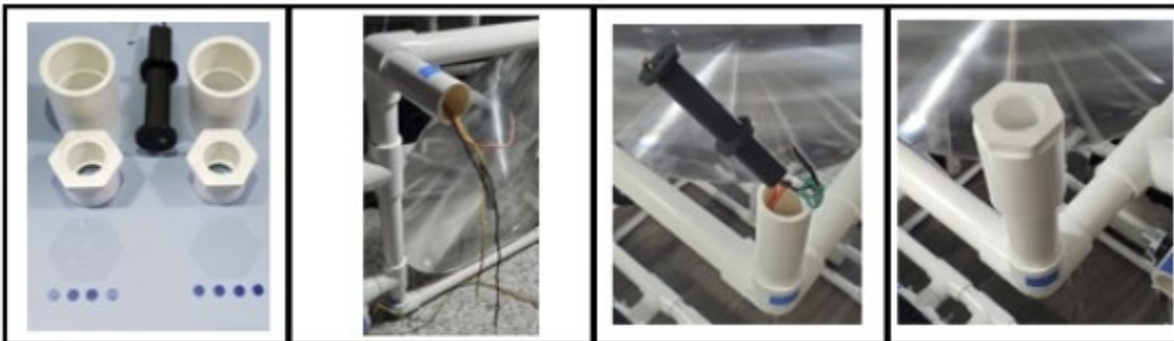
APPENDIX E
CHRONOLOGICAL CONSTRUCTION PHOTO GALLERY

The following pictures follow a chronological order from up to down, and from left to right, of the main assemblies.

Box Controller



Novel Sensor Holder



Dual Solar Tracker System



REFERENCES

- [1] Almara, Laura Mabel. Investigation on a Fresnel lens Assisted Heater for Seawater Desalination System, Proceedings of ASME-IMECE 2020, 25267 (2020).
- [2] Lee Johnson, Heather Castleden. AREA, Volume43, Issue3, September 2011, Pages 353-361. <https://doi.org/10.1111/j.1475-4762.2011.01001.x>.
- [3] S. Ashok, Kenny Chmielewski. Solar Energy. Encyclopedia Britannica, Inc. <https://www.britannica.com/science/solar-energy>
- [4] Investigation of the Fresnel lens based solar concentrator system through a unique statistical-algorithmic approach. Hassan Qandil. PhD Dissertation. University of North Texas. December 2019.
- [5] Design and Evaluation of the Fresnel-Lens Based Solar Concentrator System through a Statistical-Algorithmic Approach. Hassan Qandil and Weihuan Zhao. Proceedings of the ASME-IMECE 2018.
- [6] <https://refractiveindex.info>.
- [7] <https://www.filmetrics.com/refractive-index-database/Stainless-Steel>.
- [8] Laura Mabel Almara. Ray Optics and Heat Transfer Analysis of a Curved Fresnel Lens Heater for a Desalination System. Proceedings of COMSOL 2020, (2020).
- [9] U.S. National Weather Service. National Oceanic and Atmospheric Administration (NOAA). <https://www.weather.gov/oun/efscale>
- [10] A. Z. Hafez, A. M. Yousef, N .M. Harag. Solar tracking systems: Technologies and tracker drive types-A Review. 2018. Renewable and Sustainable Energy Reviews 91, 754-782.
- [11] Ali S. Allw, Ikhlas H. Shallal. Evaluation of Photovoltaic Solar Power of a Dual-Axis Solar Tracking System. Journal of Southest Jiaotong University. Vol. 55 No. 1. Feb. 2020. ISSN: 0258-2724 DOI: 10.35741/issn.0258-2724.55.1.52.
- [12] Mustafa H. Al-Jumaili, Hussein M. Haglan, Mohammed K. Mohammed, Qusay H. Eesee. An Automatic Multi-axis Solar Tracking System in Ramadi City: Design and Implementation. Indonesian Journal of Electrical Engineering and Computer Science. Vol. 19, No. 3, September 2020, pp. 1126~1234. ISSN: 2502-4752. DOI: 10.11591/ijeecs.v19.i3.pp1126-1234.
- [13] Izhar A. Sohu, Syed A. A. S. Bukhari, Asif A. Rahimoon, Arslan A. Sohu, Asadullah Shaikh. Implementation of Solar Tracking Design Using FPGA Tool. 2019 International Conference on Computing, Mathematics and Engineering Technologies – iCoMET 2019.

- [14] Saad T. Hamidi, Jamal A. Mohammed, Laith M. Reda. Design and Implementation of an Automatic Control for Two Axis Tracking System for Applications of Concentrated Solar Thermal Power. *Al-Khwarizmi Engineering Journal*, Vol. 14, No. 4, December, (2018). P.P. 54- 63. <https://doi.org/10.22153/kej.2018.01.010>.
- [15] R. S. Zulkafli, A.S. Bawazir, N. A. M. Amin, M. S. M. Hashim, M. S. A. Majid, N. F. M. Nasir. Dual Axis Solar Tracking System in Perlis, Malaysia. 2018. *Journal of Telecommunication, Electronic and Computer Engineering*. Vol. 10 No. 1-14. eISSN: 2289-8131.
- [16] Ceyda Aksoy, Cenk Yavuz. A Mechanical Design of an Altitude-Azimuth Two Axis Solar Tracking System for Sakarya, Turkey. *International Journal of Mechanical Engineering and Robotics Research* Vol. 7, No. 1, January 2018.
- [17] R. Vinodhkumar, Stalin John. IoT based dual-axis solar tracking system. 3rd International Conference on Advances in Mechanical Engineering (ICAME 2020). IOP Conf. Series: Materials Science and Engineering 912(2020) 032024. doi:10.1088/1757-899X/912/3/032024.
- [18] Hachimenum N. Amadi, Sebastián Gutiérrez. Design and Performance Evaluation of a Dual-Axis Solar Tracking System for Rural Applications. *EJECE, European Journal of Electrical and Computer Engineering*. Vol. 3, No. 1, January 2019. DOI: <http://dx.doi.org/10.24018/ejece.2019.3.1.52>.
- [19] Rexel U. Sabran, Arnel C. Fajardo. An Improved Sunflower-Inspired Solar Tracking Strategy for Maximizing Photovoltaic Panel Power Generation. *International Journal of Recent Technology and Engineering (IJRTE)*. ISSN: 2277-3878, Volume-8 Issue-2, July 2019. DOI: 10.35940/ijrte.B1013.078219.
- [20] Dr. Anas L. Mahmood. Date/Time Operated Two Axis Solar Radiation Tracking System for Baghdad City. *International Journal of Applied Engineering Research* ISSN 0973-4562 Volume 13, Number 7 (2018) pp. 5534-5537.
- [21] Masoumeh Abdollahpour, Mahmood R. Golzarian, Abbas Rohani, Hossein A. Zarchi. Development of a machine vision dual-axis solar tracking system. 2018. *Solar Energy* 169, 136-143.
- [22] Joel J. Ontiveros, Carlos D. Ávalos, Faustino Loza, Néstor D. Galán, Guillermo J. Rubio. Evaluation and Design of Power Controller of Two-Axis Solar Tracking by PID and FL for a Photovoltaic Module. *Hindawi. International Journal of Photoenergy*. Volume 2020, Article ID 8813732, 13 pages. <https://doi.org/10.1155/2020/8813732>.
- [23] S. V. Mitrofanov, D. K. Baykasenov, A. U. Nemaltsev. Operational experience of a Solar Power Plant with a Dual-Axis Solar Tracking System in the conditions of the Southern Urals. *E3S Web of Conferences* 124, 01022 (2019). <https://doi.org/10.1051/e3sconf/201912401022SES-2019>.

- [24] Keke Zhang, Chaoming Si, Zhencai Zhu, Chongbin Guo, Qi Shi. A Two-Dimensional Solar Tracking Stationary Guidance Method Based on Feature-Based Time Series. Hindawi. *Mathematical Problems in Engineering*. Volume 2018, Article ID 3420649, 12 pages. <https://doi.org/10.1155/2018/3420649>.
- [25] Colin Lawless, Erik Kärrfelt. Sun Following Solar Panel. Degree Project in Technology. Stockholm, Sweden 2018.
- [26] M. Umesh, Joshua Freeman, Krishnashree Achuthan, Balakrishnan Shankar. Remote Triggered Single-Axis Solar PV Tracking System with Varying Angle of Incidence. *International Journal of Renewable Energy Research*. M. Umesh et al., Vol.8, No.3, September, 2018.
- [27] M. Zinaddinov, S. Mil'shtein. Solar Tracking with Anti-Tracking Support for Ancillary Service. Conference Paper. June 2019. DOI: 10.1109/PVSC40753.2019.8980560.
- [28] Tolga Özer, Muhammed M. Kelek, Yüksel Oğuz, Sinan Kıvrak, Mustafa Şahin. Double Axis Solar Tracking System Design and Implementation. *International Journal of Scientific & Engineering Research* Volume 9, Issue 8, August 2018.
- [29] Henriks Putans, Imants Ziemelis, Ilze Pelece, Andrejs Snegovs. Solar Tracking Stand for Solar Panels and Collectors. *Engineering for Rural Development*. Jelgava, 23.-25.05.2018.
- [30] Junkun Ma, Min J. Suh. Design and Development of a Laboratory-Scale Dual-Axis Solar Tracker System. *International Journal of Engineering Research*. September 2020.
- [31] Regina C. Allil, Alfredo Manchego, Alexandre Allil, Igor Rodrigues, Arthur Werneck, Gisel C. Diaz, Fabio T. Dino, Yordanka Reyes, Marcelo Werneck. Solar tracker development based on a POF bundle and Fresnel lens applied to environment illumination and microalgae cultivation. *Elsevier. Solar Energy* 174 (2018) 648–659.
- [32] Sohaib R. Awad, Mamoon A. Al Jbaar, Mohammed A. M. Abdullah. Efficient and Low-Cost Arduino based Solar Tracking System. *IOP Conf. Series: Materials Science and Engineering* 745 (2020) 012016. DOI: 10.1088/1757-899X/745/1/012016.
- [33] M. Muladi, M. F. A. Jalil, A. Aripriharta, I. Fadlika, S. Hidayat, S. Sendari, A. N. A. Afandi, G. J. Horng, W. M. Utomo. A testbed of intelligent Sun tracking system and thermoelectric generator with Fresnel lens at solar cell system for maximizing generated energy. *Journal of Physics: Conference Series*. International Conference on Renewable Energy (ICORE) 2019. 1595 (2020) 012017. DOI: 10.1088/1742-6596/1595/1/012017.
- [34] BAJ Dere, SR Kalbande, AJ Dhondge. Performance evaluation of solar Fresnel lens cooker. *Journal of Pharmacognosy and Phytochemistry* 2019; 8(6): 2427-2431. E-ISSN: 2278-4136.
- [35] Hai Wang, Jin Huang, Mengjie Song, Yanxin Hu, Yunfeng Wang, Zijian Lu. Simulation and Experimental Study on the Optical Performance of a Fixed-Focus Fresnel Lens Solar

Concentrator Using Polar-Axis Tracking. MDPI. Energies. Energies 2018, 11, 887. DOI: 10.3390/en11040887.

[36] Pengwei Hu, Jian Yang, Lei Guo, Xiang Yu, Wenshuo Li. Solar-tracking methodology based on refraction-polarization in Snell's window for underwater navigation. Chinese Journal of Aeronautics 2021. <https://doi.org/10.1016/j.cja.2021.02.011>.

[37] Xiaoqiang Du, Yuechan Li, Pengcheng Wang, Zenghong Ma, Dangwei Li, Chuanyu Wu. Design and optimization of solar tracer with U-PRU-PUS parallel mechanism. Mechanism and Machine Theory 155 (2021) 104107.

[38] Ramadan ElGamal, Sameh Kishk, Salim Al-Rejaie, Gamal ElMasry. Incorporation of a solar tracking system for enhancing the performance of solar air heaters in drying apple slices. Renewable Energy 167 (2021) 676-684.

[39] Shunxiang Zhang, Peng Li, Qi Luo, Yuantao Chen. Experiment study of a hybrid concentrated photovoltaic/thermal(CPV/T) system. IOP Conf. Series: Earth and Environmental Science 657(2021) 012096. doi: 10.1088/1755-1315/657/1/012096.